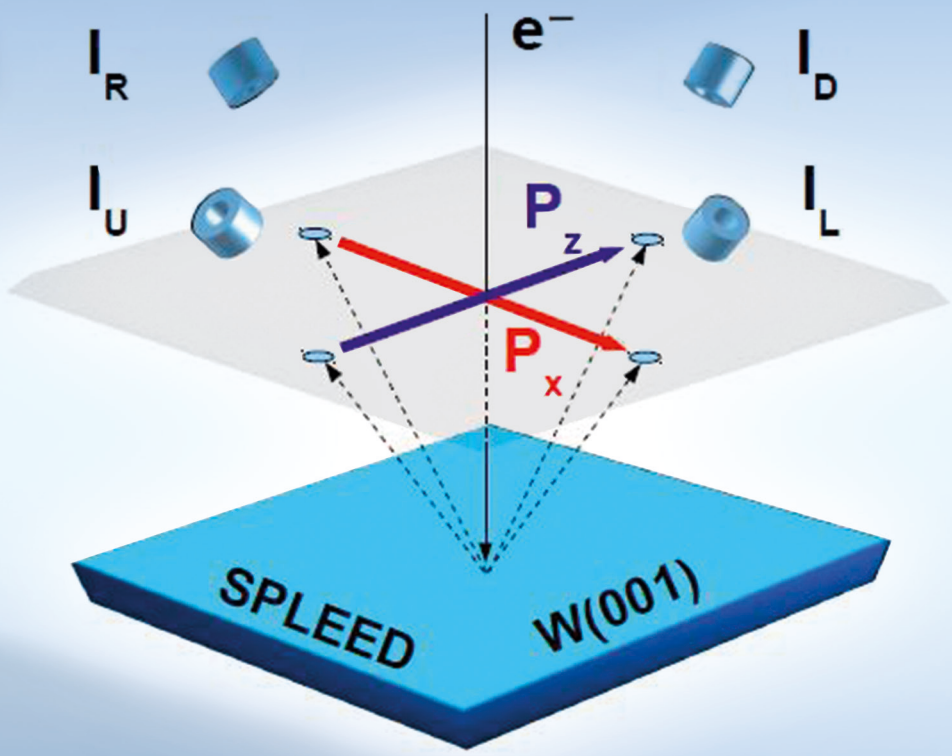

Exploring the electronic properties of novel spintronic materials by photoelectron spectroscopy

Alexej Herdt

Member of the Helmholtz Association

JÜLICH
FORSCHUNGSZENTRUM

Schriften des Forschungszentrums Jülich
Reihe Schlüsseltechnologien / Key Technologies Band / Volume 51

Forschungszentrum Jülich GmbH
Peter Grünberg Institut (PGI)
Elektronische Eigenschaften (PGI-6)

Exploring the electronic properties of novel spintronic materials by photoelectron spectroscopy

Alexej Herdt

Schriften des Forschungszentrums Jülich
Reihe Schlüsseltechnologien / Key Technologies Band / Volume 51

ISSN 1866-1807 ISBN 978-3-89336-831-0

Bibliographic information published by the Deutsche Nationalbibliothek.
The Deutsche Nationalbibliothek lists this publication in the Deutsche Nationalbibliografie; detailed bibliographic data are available in the Internet at http://dnb.d-nb.de.

Publisher and Distributor:	Forschungszentrum Jülich GmbH Zentralbibliothek 52425 Jülich Phone +49 (0) 24 61 61-53 68 · Fax +49 (0) 24 61 61-61 03 e-mail: zb-publikation@fz-juelich.de Internet: http://www.fz-juelich.de/zb
Cover Design:	Grafische Medien, Forschungszentrum Jülich GmbH
Printer:	Grafische Medien, Forschungszentrum Jülich GmbH
Copyright:	Forschungszentrum Jülich 2012

Schriften des Forschungszentrums Jülich
Reihe Schlüsseltechnologien / Key Technologies Band / Volume 51

D 464 (Diss., Duisburg, Univ., 2012)

ISSN 1866-1807
ISBN 978-3-89336-831-0

The complete volume is freely available on the Internet on the Jülicher Open Access Server (JUWEL) at http://www.fz-juelich.de/zb/juwel

Zusammenfassung

Die vorliegende Arbeit beschäftigt sich mit den elektronischen und strukturellen Oberflächeneigenschaften zweier bedeutender Materialklassen, die im Idealfall die Voraussetzung einer vollen Spinpolarisation an der Fermienergie aufweisen und somit Kandidaten für zukünftige Spintronikanwendungen darstellen: *Topologische Isolatoren* und halbmetallische *Heusler-Legierungen*.

Im Fall der topologischen Isolatoren wurde erstmals die elektronische Bandstruktur von dünnen Filmsystemen Bi_2Te_3 und Sb_2Te_3 mittels spin- und winkelaufgelöster Photoemissionsspektroskopie eingehend untersucht. Im Vordergrund stand dabei die experimentelle Bestimmung von robusten und spin-polarisierten Oberflächenzuständen. Die beobachteten Resultate wurden mit Hilfe von *ab initio* Bandstrukturberechnungen basierend auf der Dichtefunktionaltheorie im Rahmen der lokalen Dichtenäherung analysiert. In dieser Arbeit wurde auch der Einfluss verschiedener *in situ* Reinigungsverfahren, die zu einkristallinen und reinen Oberflächen von topologischen Isolatoren führen, untersucht. Nach der erfolgreichen *in situ* Präparation dünner Bi_2Te_3 und Sb_2Te_3 Filme wurde die Unempfindlichkeit der dispersiven Energiebänder gegenüber den durch die Reinigungsprozesse induzierten Oberflächenmodifikationen gezeigt. Für die experimentell ermittelten Spinpolarisationswerte der *in-plane* ($\sim 45\%$) und *out-of-plane* ($\sim 15\%$) Vektorkomponenten des Bi_2Te_3 Dirac-Kegels wurde eine sehr gute Übereinstimmung mit der Theorie gefunden. Die experimentellen Resultate wurden anhand tiefenaufgelöster Berechnungen bestätigt. Diese Studie erklärt erstmals die Reduktion der Spinpolarisation anhand einer Delokalisation der Elektronendichte und intrinsischer Spinumkehrprozesse innerhalb der ersten atomaren Schichten.

Für die Herstellung dünner Co-basierter halbmetallischer Heusler-Filme wurde eine neue Ultrahochvakuum Magnetron-Sputteranlage aufgebaut und kommissioniert. Als Materialsystem wurde die Verbindung Co_2CrAl ausgewählt. Dünne Heusler Filme wurden von einem stöchiometrischen Target auf einkristallinen MgO(001) Substraten unter verschiedenen Wachstumsbedingungen *in situ* deponiert. Durch die Analyse der Oberflächen- und Volumenbeschaffenheiten konnten erste Prozessparamter für ein epitaktisches und geordnetes Kristallwachstum reiner Filme gefunden werden. Mit Hilfe der winkelaufgelösten Photoemmissionsspektroskopie wurden dispersive Strukturen des Valenzbandes gemessen, die gut mit den berechneten Zustandsdichten übereinstimmen.

Abstract

The presented thesis deals with the electronic and structural surface properties of two important material classes: *Topological insulators* and half-metallic *Heusler alloys*. In the ideal case these are predicted to show a full spin polarization at the Fermi energy and therefore are potential candidates for future spintronic applications.

In the case of the topological insulators, the electronic band structure of thin Bi_2Te_3 and Sb_2Te_3 films was extensively studied by means of spin- and angle-resolved photoemission spectroscopy. The experimental determination of topologically protected robust and spin-polarized surface states was of particular interest. A detailed analysis of the observed results was performed within the density functional theory employing the local-density approximation.

In this work, also the influence of various *in situ* cleaning procedures for obtaining atomically clean and well-ordered topological insulator surfaces was investigated. The Bi_2Te_3 and Sb_2Te_3 thin film surfaces studied were successfully cleaned and subsequently characterized by photomission spectroscopy. It could be shown, that the measured dispersive energy bands were insensitive to the surface modifications induced by the cleaning processes. The measured *in-plane* ($\sim 45\%$) and *out-of-plane* ($\sim 15\%$) spin polarization values of the Bi_2Te_3 Dirac cone surface state exhibited a very good agreement with the theoretical calculations. The degree of the spin polarization was confirmed by means of depth-resolved slab simulations. For the first time it is shown, that the delocalization of electron density over the first quintuple layer and related spin reversal effects lead to reduced spin polarization values.

For the deposition of Co-based Heusler alloy thin films a new magnetron sputtering deposition system was assembled and commissioned. The material system chosen in this study was the ternary Co_2CrAl full-Heusler compound. Thin films were deposited *in situ* from a stoichiometric target on single crystalline MgO(001) substrates under various growth conditions. The analysis of surface and bulk structure revealed first process parameters for an epitaxial crystal growth of pure and ordered thin films. First angle-resolved photoemission measurements showed dispersive valence band features which were in good agreement to the calculated density of states.

Contents

1 Introduction

In modern condensed matter physics the investigation of the electronic properties of solids is a key step towards the realization of novel spintronic materials and devices. The central physical quantity in the field of spin electronics is the electron spin which is explored in spin-dependent electron transport phenomena for multifunctional applications. To date, the manipulation and generation of pure spin currents instead of the electron charge drives the research and the search for new materials.

Recently, a new class of materials attracted tremendous attention - the so-called *topological insulators*. These materials are of both experimental and theoretical interest due to their unique electronic properties: Unlike a conventional insulator, topological insulators possess an insulating bulk band gap, but - at the same time - offer gapless conducting surface or edge states. In particular, gapless surface states in the family of three-dimensional (3D) topological insulators (TIs) Bi_2Te_3, Bi_2Se_3, Sb_2Te_3, and their alloys are of special interest due to their potential in producing fully spin-polarized currents for spin-electronic applications [1]. Analytical theoretical models predict that these surface states are single-branched and fully spin-polarized. This fact allows for a dissipationless transport of pure spin currents at room temperature, which would be of major impact for future spintronics evolution.

The notation 'topological insulator' is related to the electronic properties of the involved energy bands. In case of a normal band insulator, surface states can exist between the valence and the conduction band. However, the insulating behaviour can be recovered by doping the material surface using non-magnetic elements or even impurities, which lead to an opening of a band gap. Such a perturbation of the electronic structure is not allowed when the surface states follow time-reversal symmetry, as it is the case for topological surface states. In particular, the topological protection is associated with a spin-degenerated crossing point of the surface states which is robust to induced surface chemical disorder [2], such as impurity doping,

which in turn prevents the gap opening. The band structure of a topological insulator may be compared to a rubber Möbius strip which sustains its topological properties after an induced deformation and does not adopt a conventional strip geometry.

In this thesis, the electronic properties of the 3D topological insulators Bi_2Te_3 and Sb_2Te_3 are studied in thin film geometry by using a combination of spin- and angle-resolved photoelectron spectroscopy (SP-ARPES), which has become the method of choice to experimentally explore the band structure of complex materials. The magnitude of the electron spin polarization in the surface states is an essential parameter in respect of spintronics applications. Recent SP-ARPES investigations were reported for Bi_2Se_3 [3], Bi_2Te_3 [4] and Sb_2Te_3 [5] single crystal samples. However, since the implementation into spin-based devices asks for thin film structures for which the promising properties observed on bulk single crystals have not been demonstrated yet, a thorough understanding of the spin polarization of the electronic states in thin films is necessary for designing future spintronics devices. It is therefore important to conduct a detailed experimental study on high-quality TI thin films in order to explore the momentum dependent spin polarization properties. A comparison of the experimental data to periodic slab density functional theory (DFT) calculations allows one to discuss the electronic properties with high reliability. Within such an approach, the average spin polarization of the TI surface states is predicted to be strongly reduced due to spin-orbit entanglement [6], and the vector of spin polarization is found to change its orientation between the subsequent atomic layers [7, 8]. With regard to this theoretical framework, the spin polarization degradation will be linked to the effective probing depth of the photoemission experiment. To our knowledge, this is the first work that studies the spin polarization limit of surface localized states in epitaxial 3D TI thin films. In addition, a detailed analysis of the spin texture within the extended binding energy regime of the Bi_2Te_3 and Sb_2Te_3 compounds is provided, which is essential for a complete understanding of the electronic band structure.

Another material class offering promising properties for future spintronic devices are the so-called *Heusler alloys*. They are divided into ternary intermetallic half- and full Heusler alloy compounds with stoichiometry compositions XYZ and X_2YZ, respectively. Here, X and Y denote transition metals and Z is a main group element.

Recent studies pointed out that half-Heusler alloys XPtBi (X = Lu,Dy,Gd) show similar electronic properties, for instance a spin-orbit coupling induced band inversion process, as TIs [9–11]. First ARPES measurements on these materials can be found in Ref. [12], however, the classification of this family of materials as topological insulators remains still discussed [12]. In the case of full-Heusler alloys, ternary cobalt-based Co_2YZ hybrids have attracted considerable interest because of their magnetic and electronic properties. In particular, they were commonly predicted to show a half-metallic behaviour at the Fermi level leading to full spin-polarized channels within the bulk electronic band structure [13]. Compared to other half-metals, specifically pervoskite manganites (e.g. $La_{1-x}Sr_xMnO_3$ structures), transition metal chalcogenides (e.g. CrSe, CrTe) or transition metal oxides (e.g. CrO_2), Heusler alloys exhibit high Curie temperatures (T_C) above or close to room temperature and have close lattice match (between 1-3%) to most semiconductors (e.g. GaAs, Si) or insulators (e.g. MgO or Al_2O_3) [14]. The natural spin imbalance in Heusler alloy films is thought to be useful for a spin-polarized current injection into semiconductors while acting as an electrode material.

However, the degree of spin polarization is affected by several factors: In particular, different surface terminations [15], site-disorder effects [16], off-stoichiometry configurations [17] and surface contaminations yield to reduced values of the spin polarization. The degree of the surface spin polarization can be determined by surface-sensitive spin-resolved photoemission spectroscopy. An *in situ* growth of clean thin film structures allows one to optimize the quality of the measured surfaces, since any surface quality degradation due to contamination is minimized. Therefore, it is mandatory to establish a technological basis for the thin film deposition as well as providing a thorough characterization of the prepared samples with respect to the used growth conditions. For this purpose, a new ultra-high vacuum (UHV) preparation chamber including a direct current magnetron sputter source was assembled, installed and commissioned. Ternary Co_2CrAl Heusler alloy thin films were grown *in situ* on single crystalline MgO(001) substrates and subsequently characterized by using *in situ* and *ex situ* approaches. Moreover, the electronic band structure of epitaxial Heusler alloy thin films was studied by means of a spin- and angle-resolved photoemission experiment.

The thesis is structured as follows:

- **Chapter 2** outlines the theoretical aspects of spin- and angle-resolved photoemission spectroscopy. Furthermore, a short description of the DFT approach, which is used for the interpretation of the experimental data is given.
- In **chapter 3**, the technical details of the experimental setups and sample characterization methods are summarized. Moreover, the equipment of the new ultra-high vacuum thin film preparation chamber, comprising of a direct current magnetron sputter source and a heatable sample stage are presented.
- **Chapter 4** provides an overview of fundamental structural and electronic properties of 3D TIs. Thereafter, experimental results on clean and well-ordered Bi_2Te_3/Si(111) and Sb_2Te_3/Si(111) thin films will be presented. First, a detailed description of successfully applied sample preparation methods is given. This is followed by a discussion of the spin- and angle-resolved photoemission results. In order to analyze the experimental data, we combine the photoemission experiments with *ab initio* slab calculations. Special attention is payed to the magnitude of the electron spin polarization in surface states.
- **Chapter 5** is dedicated to the growth and electronic structure of half-metallic Heusler alloys compounds. First, a short discussion of the structural and electronic properties is given. Thereafter, the sample preparation of *in situ* grown Co_2CrAl thin films on single crystalline MgO(001) substrates is presented which is followed by the chemical and structural characterization results. Finally, the experimental photoemission results of the valence-band structure are summarized.
- **Chapter 6** gives a summary and an outlook of this thesis.

2 Theoretical considerations

In this work, main emphasis is put on the experimental determination of the valence electronic structure of 3D TIs Bi_2Te_3, Sb_2Te_3 and Heusler alloy Co_2CrAl thin films by means of spin- and angle-resolved photoelectron spectroscopy. The interpretation of the data is performed in the framework of density functional theory (DFT). In this chapter, the main aspects of the PES theory and DFT theory will be outlined.

2.1 Fundamental aspects of spin- and angle-resolved photoemission spectroscopy

Photoemission spectroscopy (PES) is a versatile experimental method to probe the electronic properties of various material systems. The valence band electronic structure of thin film and single crystal surfaces can be investigated by a surface-sensitive low-energy photoemission experiment with photon energies $h\nu$ varying between 10 and 100 eV [18]. Typically used photon sources are gas discharge lamps or synchrotron radiation light sources.

In the reciprocal space, the electronic band structure $E_B(\boldsymbol{k})$ is characterized by the relation between the binding energy E_B and the wave number $\boldsymbol{k}$ of the electron. These quantities can be directly obtained from an angular-resolved photoemission spectroscopy (ARPES) experiment, with the general scheme shown in Fig. 2.1. The irradiation of a sample surface by monochromatic light of the energy $h\nu$ leads to the excitation of photoelectrons above

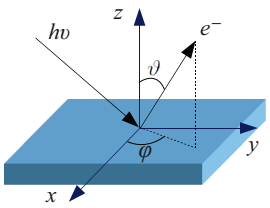

Figure 2.1: *Illustration of the PES geometry. Emitted photoelectrons leave the solid in in the direction defined by* (ϑ) *and* (φ) *emission angles.*

the Fermi energy E_F, which is related to the energy of the highest occupied state. An excitation of a photoelectron takes place, if an electron gains enough energy to overcome its binding energy E_B as well as the work function Φ of the material. The work function Φ is a threshold energy which depends sensitively on the material and can range from 2 eV in alkali metals to 5 eV in noble metals [19]. Satisfying the energy conservation principle, the kinetic energy of the escaped electrons can be written as

$$E_{kin} = h\nu - \Phi - |E_B|. \tag{2.1}$$

If the work function and the photon energy are known, the binding energy of the electron can be determined from a measurement of its kinetic energy. The electronic band structure is typically mapped by the study of the kinetic energy distribution of the emitted electrons in dependence of their emission angles. In case of spin-polarized electronic states, the combination of spin- and angle-resolved photoemission analysis of the electrons also accounts for the electron spin orientation $\sigma = (\uparrow, \downarrow)$, yielding the full set of electronic structure $E(\boldsymbol{k}, \sigma)$. A simple view of the photoemission process is outlined in the following.

2.1.1 The phenomenological three-step model

Photoemission spectra are typically interpreted in terms of the phenomenological three-step model, which dates back to the description by Berglund and Spicer [20]. This model treats the photoemission mechanism in terms of three independent steps in a single electron picture: (1) photon absorption followed by a *photoexcitation* of the photoelectron, (2) *transport* to the surface and finally (3) *transmission* and escape across the surface, as depicted in Fig. 2.2(a). Before the photoexcitation the electrons are described by the initial wave-vector $\boldsymbol{k}_i$. Electrons moving in the solid after the excitation are characterized by a final wave-vector $\boldsymbol{k}_f$, whereas the momentum of the emitted photoelectron in the vacuum is $\boldsymbol{K}$.

In step (1), a periodic potential $\mathrm{V}(\boldsymbol{r}) = \mathrm{V}(\boldsymbol{r}+\boldsymbol{R})$ is assumed, for which the initial and final states are described by Bloch waves $\psi_{n,\boldsymbol{k}} = u_{n,\boldsymbol{k}}(\boldsymbol{r}) \cdot e^{i\boldsymbol{k}\cdot\boldsymbol{r}}$ and satisfy the condition $\psi_{n,\boldsymbol{k}}(\boldsymbol{r}+\boldsymbol{R}) = e^{i\boldsymbol{k}\cdot\boldsymbol{R}}\psi_{n,\boldsymbol{k}}(\boldsymbol{r})$. Here, n is the band index within the electronic band structure, and i and f denote the initial and final states, respectively.

Before the excitation process, the initial eigenstate ψ_i^N represents a many-particle N-electron ground state, whereas after the photoexcitation the final state ψ_f^N is

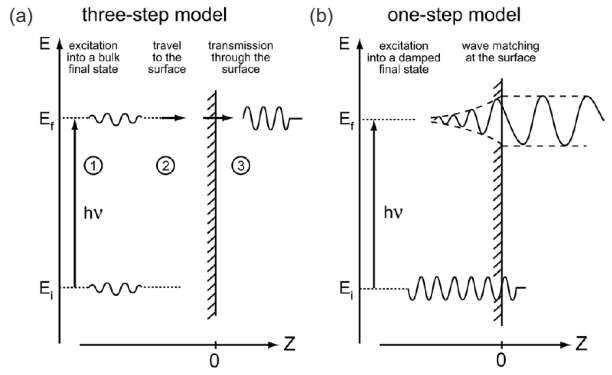

Figure 2.2: *(a) Three-step model of photoemission. The interaction with an electromagnetic wave leads to the excitation of a photoelectron. The transition from an initial to a final state is shown in the step (1). The travel through the solid along z is covered in step (2). The final transmission and escape to the vacuum is treated in step (3). (b) Definition of the wave-vector component inside the bulk material and outside the crystal. Taken from [18].*

the ionized $(N-1)$-electron state. As will be shown in paragraph 2.2, electron correlations and interaction effects within a many-body system can be discussed in terms of the DFT approach. After the photon absorption the electrons are excited from an occupied state ψ_i^N into an empty final state ψ_f^N above the vacuum level. For low photon energies (e.g. $h\nu < 30$ eV) in the ultraviolet regime - as used in this thesis - the momentum of the photon can be neglected assuming $\boldsymbol{k}_f^N = \boldsymbol{k}_i^N + \boldsymbol{k}_{ph} \approx \boldsymbol{k}_i^N$ and the energy conservation $E_f^N = E_i^N + h\nu$, which leads to vertical interband transitions within the reduced zone scheme. In the extended-zone scheme equivalent $\boldsymbol{k}$-space points within the electronic band structure are connected by a reciprocal vector $\boldsymbol{G}$ described as $\boldsymbol{k}_f^N = \boldsymbol{k}_i^N + \boldsymbol{G}$.

In general, the interaction between the photon and the N-electron ground state is introduced by using a non-relativistic Schrödinger-equation [18, 21]. The influence of the electromagnetic field on the undisturbed system $H_0 = \boldsymbol{p}/2m$ is entered by a substitution $\boldsymbol{p} \rightarrow \boldsymbol{p} - \frac{e}{c}\boldsymbol{A}$ of the momentum operator, with $\boldsymbol{A}$ representing the vector potential of the electromagnetic field. For relativistic effects of fermions it is important to provide a Hamiltonian in the relativistic form of the Schrödinger equation describing an electron in the presence of an electromagnetic field [22].

Moreover, spin-dependent terms should be considered for the interpretation of spin-polarized spectra. Thus, the Hamiltonian can be written as

$$H = \underbrace{\frac{1}{2m}\left(\boldsymbol{p} - \frac{e}{c}\boldsymbol{A}\right)^2 + e\phi}_{H_I} - \underbrace{\frac{e\hbar}{2mc}\boldsymbol{\sigma}\cdot\boldsymbol{\nabla}\times\boldsymbol{A}}_{H_{II}} + \underbrace{\frac{ie\hbar}{4m^2c^2}\boldsymbol{\sigma}\cdot(\boldsymbol{E}\cdot\boldsymbol{p})}_{H_{III}} - \underbrace{\frac{e\hbar}{4m^2c^2}\boldsymbol{\sigma}\cdot(\boldsymbol{E}\times\boldsymbol{p})}_{H_{IV}}. \tag{2.2}$$

The electron spin is included in terms of the Pauli matrices $\boldsymbol{\sigma} = (\sigma_x, \sigma_y, \sigma_z)$ given as

$$\sigma_x = \begin{pmatrix} 0 & 1 \\ 1 & 0 \end{pmatrix}, \quad \sigma_y = \begin{pmatrix} 0 & -i \\ i & 0 \end{pmatrix} \quad \text{and} \quad \sigma_z = \begin{pmatrix} 1 & 0 \\ 0 & -1 \end{pmatrix}. \tag{2.3}$$

The first term H_I is related to the non-relativistic spinless case with doubly degenerated (spin-up and spin-down) bands and represents the Hamiltonian of the solid disturbed by the incident electromagnetic radiation. The interaction between the magnetic dipole of a spin-1/2 particle with an external magnetic field $\boldsymbol{B}$ is described within the second term H_{II} using $\boldsymbol{B} = \boldsymbol{\nabla}\times\boldsymbol{A}$. The term H_{III} represents a relativistic correction to the energy, whereas the term H_{IV} accounts for the spin-orbit coupling. Within the fundamental electrodynamics it is allowed to choose the Coulomb gauge to fullfill $\boldsymbol{\nabla}\cdot\boldsymbol{A} = 0$. In combination with the commutator relation $[\boldsymbol{p}, \boldsymbol{A}] = -i\hbar\boldsymbol{\nabla}\cdot\boldsymbol{A}$ the non-relativistic term H_I can be expressed as

$$H_I = \frac{1}{2m}\boldsymbol{p}^2 + H_{int}, \tag{2.4}$$

wherein $H_{int} = \frac{e}{mc}\boldsymbol{A}_0\cdot\boldsymbol{p}$ is the perturbation Hamiltonian. Here, $\boldsymbol{A}_0$ is considered as a spatially constant quantity in the simplified system within the dipole approximation using $\boldsymbol{A}(\boldsymbol{r}, t) = \boldsymbol{A}_0(t)$ [21]. Moreover, for the external scalar potential the gauge $\Phi = 0$ was chosen. Thus, the excitation process can further be approximated by Fermi's Golden rule, which yields the transition probability for an optical excitation between the initial ψ_i^N and the final states ψ_f^N given as [23]

$$\omega_{f\to i} = \frac{2\pi}{\hbar}|\underbrace{\langle\psi_f^N|H_{int}|\psi_i^N\rangle}_{M_{f\to i}}|^2\delta(E_f^N - E_i^N - h\nu), \tag{2.5}$$

where the energy conservation is provided by the Delta function. In the framework of the first order perturbation theory and dipole approximation, the transition matrix element M_{if} is expressed as

$$M_{f\to i} \propto \boldsymbol{A}_0(E_f^N - E_i^N)\langle\psi_f^N|\boldsymbol{e}\cdot\boldsymbol{r}|\psi_i^N\rangle, \tag{2.6}$$

where $\boldsymbol{e}$ is the polarization vector of the electromagnetic radiation. Here, the quantity $\langle\psi_f|\boldsymbol{e}\cdot\boldsymbol{r}|\psi_i\rangle$ dictates qualitatively whether a transition takes place or not and quantitatively yields the transition strength of each particular photoemission process in terms of selected symmetries of the wave functions obeying the dipole selection rules [24]. A detailed interpretation of the photoemission data, however, can only be performed by means of a full-sclae *ab initio* calculation of the photoemission spectra.

In the second step (2), the photoexcited electron undergoes elastic and inelastic scattering processes due to the strong Coulomb interactions inside the solid. Caused by electron-electron, electron-phonon and defect scattering, the electron propagation is reduced and can be described by means of the inelastic electron mean free path λ (IMFP), which defines the surface sensitivity or rather the information depth of the experiment. Only non-scattered and elastically scattered electrons contribute to the photoemission signal which contains sharp intensity peaks. Inelastically scattered electrons, however, create the so-called inelastic background, which is more or less featureless. The IMPF affects the photoelectron intensity I_0 along a propagation path l as [24]

$$I(l) = I_0 e^{(-\frac{l}{\lambda})}. \tag{2.7}$$

As shown in Fig. 2.3, the general shape of the IMPF energy dependence curve is 'universal' for several kinds of materials. The minima of the curve corresponds to an IMFP of approximately 5 Å for kinetic energies around 100 eV [26]. In particular, for energies in the range between 10 and 100 eV the electrons can be approximately described by a two-

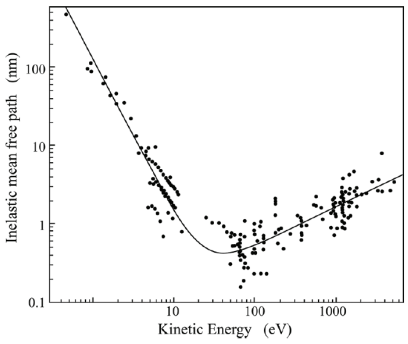

Figure 2.3: *Universal curve of the electron mean free path λ as a function of the kinetic energy for different elements (black dots). Taken from [25].*

dimensional free-electron gas model where bonding properties can be neglected, and the inverse mean free path λ^{-1} is expressed as [18]

$$\lambda^{-1} \simeq \sqrt{3}\frac{a_0 R}{E_{kin}} r_s^{3/2} ln\left[\left(\frac{4}{9\pi}\right)^{\frac{2}{3}} \frac{E_{kin}}{R} r_s^2\right]. \tag{2.8}$$

Here, $R = 13.6$ eV is the Rydberg constant and $a_0 = 0.529$ Å is the Bohr radius. Due to this high surface sensitivity, low-energy PES only probes the topmost surface atomic layers and is therefore perfectly suited for studies of surface related phenomena. Hence, the band mapping experiments have to be performed under UHV conditions as well as on highly-ordered and clean surfaces.

The third step (3) considers the transmission of the electron through the surface barrier of a semi-infinite crystal. In this case, the truncation of a finite crystal causes a broken symmetry along the z-axis. Fig. 2.4 shows a schematic representation of the involved wave-vector components in the solid and the vacuum.

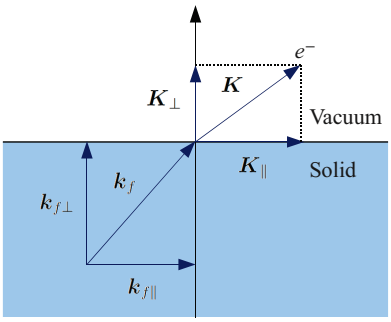

Figure 2.4: *Sketch of the electron wave-vector components in the vacuum and solid regions. During the transmission of the electron through the surface the component of the final wave-vector parallel to the surface* $\boldsymbol{k}_{f\parallel} = \boldsymbol{K}_\parallel$ *is conserved.*

The change of the potential leads to a modification of the perpendicular wave-vector component $\boldsymbol{k}_\perp$ which is not conserved during the transmission through the surface potential barrier, whereas the *in-plane* momentum wave-vector component $\boldsymbol{k}_\parallel$ and its reciprocal vector $\boldsymbol{G}_\parallel$ remain undisturbed. The parallel component of the wave-vector can be written as

$$\boldsymbol{k}_\parallel = \boldsymbol{K}_\parallel = \frac{1}{\hbar}\sqrt{2mE_{kin}} \cdot sin(\vartheta). \tag{2.9}$$

Besides various non-trivial band-mapping schemes reported in Refs. [23,27] the perpendicular wave-vector moment can be approximated within the nearly free-electron-picture as

$$\boldsymbol{k}_{\perp} = \frac{1}{\hbar}\sqrt{2m(E_{kin}cos^2(\vartheta) + V_0)}, \tag{2.10}$$

where V_0 is the inner potential at the surface. Since E_{kin} and ϑ are known parameters, V_0 has to be determined from the comparison of the experimental and theoretical band structures.

The resulting photocurrent measured during the ARPES measurement contains all possible transitions between the initial and final states and can be finally written by using eq. 2.5 as

$$I(\boldsymbol{k}, h\nu) = \sum_{f,i} \omega_{f\to i}. \tag{2.11}$$

A more accurate description of the photocurrent, however, can be obtained by means of the one-step model which treats the whole photoemission process as a single quantum-mechanically coherent process [28], see Fig. 2.2(b). In particular, the final states can be calculated using time-reversed states of low energy electron diffraction (LEED) functions Φ_{LEED} which include many-body effects. Due to its applicability to advanced fully relativistic photoemission calculations, this model is widely used in modern electronic band structure simulation tools. More details can be found in Refs. [21,29].

2.1.2 Spin-polarized photoemission

Spin-resolved photoemission spectroscopy allows the experimental detection of the electron spin in $\boldsymbol{k}$-space. In addition to the kinetic energy and the momentum of the electrons available from ARPES, the determination of the *spin expectation* value provides a full characterization of the electronic states. A detailed theoretical description of polarized electrons can be found in Ref. [30]. Mathematically, quantum states are given in the Hilbert space. In the Schrödinger formalism the spin state $|\chi\rangle$ of an electron is described by a linear combination given as

$$|\chi\rangle = a_+ |\alpha\rangle + a_- |\beta\rangle , \tag{2.12}$$

with the complex numbers a_+, a_- and the eigenstates

$$|\alpha\rangle = \left|\chi\left(+\tfrac{1}{2}\right)\right\rangle = \begin{pmatrix}1\\0\end{pmatrix} = |\uparrow\rangle\,, \quad |\beta\rangle = \left|\chi\left(-\tfrac{1}{2}\right)\right\rangle = \begin{pmatrix}0\\1\end{pmatrix} = |\downarrow\rangle \tag{2.13}$$

representing orthogonal two-component spinors of spin-up and spin-down electrons along a given quantization axis. Assuming an electron beam with normalized pure spin states described by eq. 2.12, the expectation value of the Pauli matrices (see eq. 2.3)

$$\boldsymbol{P} = \langle\boldsymbol{\sigma}\rangle = \langle\chi|\,\boldsymbol{\sigma}\,|\chi\rangle = (a_+^*, a_-^*)\boldsymbol{\sigma}\begin{pmatrix}a_+\\a_-\end{pmatrix} \tag{2.14}$$

describes an average value of the spin direction within an electron ensemble, which is known as the spin polarization vector. Therefore, in this case a measured spin polarization reflects the expectation value of the quantum observable $\boldsymbol{\sigma}$. According to the particular vector components of the Pauli matrices, the degree of polarization or rather the magnitude of the polarization vector can be written as

$$P = \sqrt{P_x^2 + P_y^2 + P_z^2}, \tag{2.15}$$

which contains the *in-plane* P_x, P_y and *out-of-plane* P_z polarization components with respect to a quantization axis in three-dimensional space. In this particular case P is 1 and is related to a totally polarized electron beam. However, in real systems an electron beam is partially polarized and leads to a spin polarization which is less than unity.

In the solid, the presence of spin-dependent interactions leads to spin-polarized ground states of the electronic system which can be detected by spin-resolved photoemission spectroscopy. Phenomenologically, exchange-induced polarization effects are observed in the presence of itinerant ferro- and antiferromagnetism, whereas spin-polarized states from non-magnetic materials are described by spin-orbit coupling (SOC) effects, which lead to a splitting of atomic levels. Moreover, spin-orbit interaction enables the generation of spin-polarized electrons by an optical spin orientation process. On the basis of symmetry arguments, optical spin excitation is possible for circularly, linearly and unpolarized light. The concept of optical spin orientation can be generalized to magnetic materials, where it is called magnetic

dichroism [31]. More details can be found in Ref. [32]. There exists also a spin-orbit dependent polarization effect at surfaces as a special case, known as Rashba effect.

Within the framework of this thesis, the main goal is to obtain momentum dependent spin information originating from highly spin-polarized materials, such as topological insulators and half-metallic Heusler alloys. In order to understand the electronic structure of topological insulators presented in chapter 4, it is important to review the basic properties of spin-polarized surface states originating from non-magnetic materials and to provide the theoretical basis for their experimental investigation by means of a spin-resolved PES experiment. The orientation of the spin polarization vector $\boldsymbol{P}$ is determined by symmetry considerations defining the relevant quantization axis [33]. The direction of quantization is either determined by the crystal structure or by the entire experiment as a freely selectable parameter [24, 34]. As will be shown later, due to the spin-momentum locking, Rashba systems and topological insulators have a well-defined spin quantization axis [34].

In non-magnetic materials, such as TIs, spin-polarized electrons arise from strong spin-orbit interactions. Typical examples are high Z materials, such as gold (Au), bismuth (Bi) or antimony (Sb) surfaces. Moreover, the influence of SOC on a non-magnetic clean Cu(001) surface by spin- and angle resolved PES was reported in Ref. [35]. It was shown, that the spin dependence in the transition matrix $M_{f\to i}$, caused by the irradiation with circularly polarized light was mainly produced due to the effect of SOC. In particular, the coupling of the spatial and the spin parts in the electron wave functions leads to different excitation probabilities for spin-up and spin-down states, which results in a spin-polarized photoemission intensities even in low Z materials.

In many cases the electronic configuration of a surface is not equivalent to a simple truncation of the bulk material, since different surface reconstructions, such as a change of atomic positions compared to the bulk positions, lead to a modified crystal structure of the surface layers. Moreover, a broken translational symmetry caused by the sudden truncation along the surface normal forms a confined two-dimensional electron gas (2DEG) which may result in a formation of surface states.

The general theory of surface states dates back to the pioneering theoretical work of Shockley [36], which describes the occurrence of surface states only for inverted band gaps at the Brillouin zone boundaries. A more extended picture based on analytical calculations by Forstmann and Pendry [37–39] proposed the existence of

surface states residing in SO band gaps for high Z materials. They showed that within a SO opened band gap, which is situated between two high symmetry points, at least one surface state must be present.

Considering an electron with a momentum $\boldsymbol{k}$ and spin ($\uparrow$ or $\downarrow$), the combination of the time-reversal (TR) symmetry

$$E_{\uparrow}(\boldsymbol{k}) = E_{\downarrow}(-\boldsymbol{k}) \tag{2.16}$$

and the inversion symmetry

$$E_{\uparrow}(\boldsymbol{k}) = E_{\uparrow}(-\boldsymbol{k}) \quad \text{and} \quad E_{\downarrow}(\boldsymbol{k}) = E_{\downarrow}(-\boldsymbol{k}) \tag{2.17}$$

leads to spin-degenerated eigenstates for the non-magnetic (i.e. non time-reversal broken) bulk electronic structure, known as Kramers states with energies

$$E_{\uparrow}(\boldsymbol{k}) = E_{\downarrow}(\boldsymbol{k}). \tag{2.18}$$

Here, a single-particle picture has been considered with an electron moving in a constant potential $V_0 = 0$. Moreover, no external magnetic fields are present. A schematic drawing of conventional non-magnetic surface state and the corresponding Fermi surface without SOC is shown in Fig. 2.5(a). At the surface, the missing spatial inversion symmetry lifts the spin-degeneracy even in the absence of an external magnetic field $\boldsymbol{B}$. This can be deduced from a Taylor expansion of a surface confining potential $V(\boldsymbol{r}) = V_0 + e\boldsymbol{E} \cdot \boldsymbol{r}$ [40], whereas in the lowest order the potential is described by means of an electric field $\boldsymbol{E}$. Thus, the truncation of the bulk material involves a potential gradient perpendicular to the surface, which is related to an electric field $\boldsymbol{E}(\boldsymbol{r}) = \nabla V(\boldsymbol{r})$. As a consequence of the relativistic Lorentz transformation of the electric field, the electron experiences a magnetic field $\boldsymbol{B} = \frac{1}{c}(\boldsymbol{v} \times \boldsymbol{E}) = \frac{\hbar}{m^* c}(\boldsymbol{k} \times \boldsymbol{E})$ in its local frame, wherein m^* represents the effective mass and c is the speed of light.

SOC is a relativistic effect, which can be derived from fundamental quantum mechanics. Assuming an electron travelling with a velocity $\boldsymbol{v}$ and momentum $\boldsymbol{p}$ in a centrosymmetric potential V(r), the SOC term can be written as [41]

$$\boldsymbol{\sigma}(\boldsymbol{E}(\boldsymbol{r}) \times \boldsymbol{p}) = \boldsymbol{\sigma}(\boldsymbol{\nabla} V(\boldsymbol{r}) \times \boldsymbol{p}) = \frac{1}{r}\frac{dV(r)}{dr}\boldsymbol{\sigma} \cdot (\boldsymbol{r} \times \boldsymbol{p})) = \frac{1}{r}\frac{dV(r)}{dr}(\boldsymbol{\sigma} \cdot \boldsymbol{L}) = \xi \boldsymbol{\sigma} \cdot \boldsymbol{L}, \tag{2.19}$$

where $\boldsymbol{L}$ is the orbital momentum operator and ξ is a SOC constant. The electron spin is described by the Pauli matrices $\boldsymbol{\sigma} = (\sigma_x, \sigma_y, \sigma_z)$. For the special case of a surface with a specific geometry and a modified potential, the interaction of the spin $\boldsymbol{\sigma}$ and the magnetic field $\boldsymbol{B}$ is attributed to the Rashba or Bychkov-Rashba Hamiltonian

$$H_R \propto \boldsymbol{\sigma}(\boldsymbol{p} \times \boldsymbol{E}) \quad \text{or} \quad H_R = \alpha_R(|\boldsymbol{E}|)\boldsymbol{\sigma}(\boldsymbol{k} \times \boldsymbol{e}_z), \tag{2.20}$$

where α_R is a material-specific coupling factor, known as Rashba-parameter. α_R is characterized by the gradient of the potential $V(\boldsymbol{r})$ in z direction as $\alpha_R \propto \partial V/\partial z$, which is related to the strength of the Rashba effect [42]. As can be seen, H_R is nothing else than the relativistic SOC term introduced in eq. 2.19. Whereas without SOC the energy bands are spin degenerate, a combination of atomic SOC and the asymmetric[1] surface potential induces a Rashba spin splitting of the electronic surface states located near the surface. Using eq. 2.3, for the electrons moving within a (x, y)-plane of a 2DEG with respect to a quantization axis along the z direction, the non-magnetic system can be described by the Hamiltonian [43]

$$H = H_0 + H_R = \frac{\hbar^2}{2m^*}\boldsymbol{\nabla}^2 - \alpha_R\left(i\sigma_y\frac{\partial}{\partial x} - i\sigma_x\frac{\partial}{\partial y}\right), \tag{2.21}$$

which can be solved in an analytical way. The eigenenergies of H_R, with broken inversion symmetry $E_\uparrow(\boldsymbol{k}_\parallel) \neq E_\downarrow(\boldsymbol{k}_\parallel)$, are related to the upper (+) and lower (-) Rashba branches

$$E_\pm(\boldsymbol{k}_\parallel) = \frac{\hbar^2}{2m^*}|\boldsymbol{k}_\parallel|^2 \pm \alpha_R|\boldsymbol{k}_\parallel|. \tag{2.22}$$

In this simple model, the spin expectation vector can be written as

$$\boldsymbol{S}_\pm(\boldsymbol{k}) = \frac{\hbar}{2}\begin{pmatrix} \mp sin\varphi \\ \pm cos\varphi \\ 0 \end{pmatrix}, \tag{2.23}$$

which is always perpendicular to $\boldsymbol{k}$ with an absent *out-of-plane* z component. More precisely, this implies non-degenerate surface states and related Fermi surfaces arranged in pairs with deviating wave-vectors carrying opposite spin orientations, see Fig. 2.5(b), wherein the arrows indicate the direction of the electron spin.

[1] The asymmetry of the potential lies in the direction perpendicular to the *(x,y)*-plane.

Rashba-type SO splitting has been investigated on several materials, such as (111)-oriented Au [44,45], as well as on high Z material surfaces of Bi [46–48], Sb [49] and related surface alloys [50, 51] by means of dedicated photoemission studies. In TIs being investigated in this thesis, however, SOC induces in addition, primarily a band inversion process which opens a band energy gap near the Fermi level. The surface states are therefore trapped between the conduction and the valence band as will be shown in more detail in chapter 4. In addition, the states are spin-polarized due to the aforementioned Rashba-effect. The surface states appear as single band dispersions, which carry a single electron spin state at each surface wavevector $\boldsymbol{k}$, whereas states with opposite wavevector, $\boldsymbol{k}$, have opposite spin 'orientation' [52]. At the high symmetry points of the Brillouin zone, however, the surface states remain spin-degenerate satisfying the Kramers degeneracy, see Fig. 2.5(c); these points are the so-called Dirac points. More details about TIs and the effect of SO interaction on that materials will be presented in chapter 4.

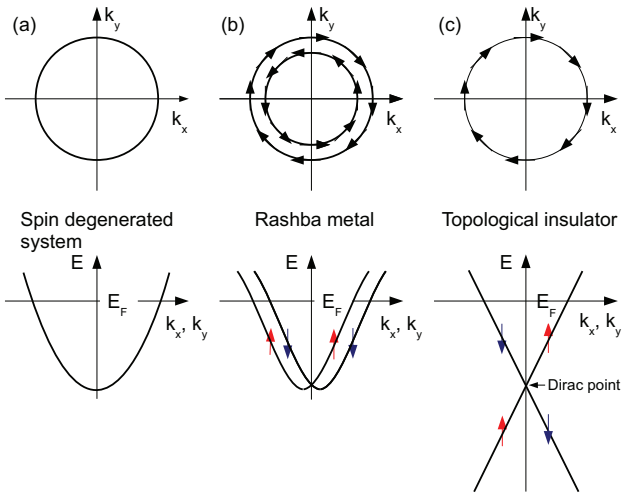

Figure 2.5: *Schematic Fermi surface (top) and energy band dispersion (bottom) of a non-magnetic material (a) without SO influence, (b) with SOC included Rasba spin splitting and (c) SOC induced single branched topological surface states.*

In order to obtain accurate spin informations from spin-polarized surface states, it is mandatory to determine the exact emission position within the $\boldsymbol{k}$-space. For

this reason, a state-of-the-art PES experiment is usually equipped with a combination of an angular and a spin-sensitive detection system; in this SP-ARPES mode a comprehensive determination of the electronic structure is possible by means of a prior spin-integrated Fermi surface mapping within the surface Brillouin zone and a subsequent measurement of the spin polarization vector $\boldsymbol{P}$. The experimental combination of spin- and angle-resolved PES modes directly yields a thorough determination of the electronic band structure characterized by the kinetic energy E_{kin}, the wave-vector moment $\boldsymbol{k}$ and the electron spin $\boldsymbol{\sigma}$. After positioning of the sample to the desired emission angle, a spin detector allows the measurement of the partial polarized beam intensities $I^{\uparrow,\downarrow}$ for spin-up and spin-down electrons, respectively. These can be obtained separately by using the expressions

$$I^{\uparrow} = \frac{1}{2} I(E)(1 + P(E)) \quad \text{and} \quad I^{\uparrow} = \frac{1}{2} I(E)(1 - P(E)), \tag{2.24}$$

with the spin-integrated total intensity $I(E)$ of emitted photoelectrons and the total polarization $P(E)$ value given by the asymmetry expression

$$P(E) = \frac{I^{\uparrow}(E) - I^{\downarrow}(E)}{I^{\uparrow}(E) + I^{\downarrow}(E)}. \tag{2.25}$$

2.2 Density functional theory: An overview

In this work the electronic band structure calculations are used for the interpretation of the experimental data. In the case of bulk related electronic properties of topological insulators and Heusler alloys, I have applied the WIEN2k [53] package in the scheme of the density functional theory. Surface related calculations have been investigated by our collaborators from the theory group PGI-1 (Dr. Bihlmayer, Prof. Dr. Blügel) using the FLEUR code (for details see Ref. [54]) at the Research Centre Jülich. The simulations are based on the *local density approximation (LDA)* and *generalized gradient approximation (GGA)* approaches with the basic ideas outlined in the following.

In condensed matter physics, a many-body system consists of a large number of interacting particles, such as electrons in a periodic crystal system, which can be explained by means of elementary quantum mechanics. By assuming the Born-Oppenheimer approximation, the movement of electrons in the field of the nuclei

is governed by the time-independent Schrödinger equation describing a N-electron system

$$\underbrace{(T_e + V_{Ne} + V_{ee})}_{H} \psi_i(\boldsymbol{r}_1, \ldots, \boldsymbol{r}_N | \boldsymbol{R}_1, \ldots, \boldsymbol{R}_M) = E_i \psi_i(\boldsymbol{r}_1, \ldots, \boldsymbol{r}_N | \boldsymbol{R}_1, \ldots, \boldsymbol{R}_M), \tag{2.26}$$

where T_e is the kinetic energy of the electrons, V_{Ne} describes the interaction between the nuclei and the electrons and V_{ee} is the electron-electron interaction term. $(\boldsymbol{r}_1, \ldots, \boldsymbol{r}_N | \boldsymbol{R}_1, \ldots, \boldsymbol{R}_M)$ are the space coordinates of the electrons and the nuclei. If H contains only single-particle terms, the problem is tractable. The electron-electron interaction, however, complicates the solution of such a system, thus leading to a problem which cannot be solved exactly in general. One approach for solving this problem is the Hartree-Fock method, where the wave function of the ground state is approximated by a Slater determinant of N orbitals which are used to minimize the ground state energy by means of a variational principle. A detailed description of this approach can be found in Refs. [55, 56]. Since this approach does not provide exact values of ground state energies, modern computational methods often use the Hartree-Fock plane wave method as starting point for the simulations of the electronic band structure.

Instead of using Slater determinants, Hohenberg and Kohn suggested to express the ground state energy E of a many-particle system as functional of the electron density $n(\boldsymbol{r})$ [57], which gives the density distribution of the particles. In particular, two central theorems have been formulated for N electrons moving in an external potential $v(\boldsymbol{r})$ which is caused by a nuclei in a non-degenerate ground state [58]:

- The many-body wave function ψ and potential $v(\boldsymbol{r})$ are uniquely determined by the particle density distribution $n(\boldsymbol{r})$ as a basic variable.
- For a guessed density $n(\boldsymbol{r}) > 0$ satisfying the particle conservation $\int n(\boldsymbol{r}) d\boldsymbol{r} = N$, the energy functional is written by means of an energy variation principle

  $$E[n_0(\boldsymbol{r})] \leq E[n(\boldsymbol{r})] = T_e[n(\boldsymbol{r})] + E_{Ne}[n(\boldsymbol{r})] + E_{ee}[n(\boldsymbol{r})], \tag{2.27}$$

  where n_0 is the ground state density and T_e, E_{Ne} and E_{ee} are the corresponding energies, see eq. 2.26.

The Hohenberg-Kohn theorems are used as a basis for modern DFT codes. In the Hohenberg-Kohn-Sham theory [59], the many-body problem can be transferred into an effective single-particle system, wherein the particle density distribution is expressed in terms of auxiliary wave functions $\phi_i(\boldsymbol{r})$ as

$$n(\boldsymbol{r}) = \sum_{i=1}^{N} |\phi_i(\boldsymbol{r})|^2. \tag{2.28}$$

This leads to the so-called *Kohn-Sham* equations which have the form of a standard Schrödinger equation, and have been proposed in the year 1965 [59]

$$H_{eff}^{KS}\phi_i(\boldsymbol{r}) = \epsilon_i\phi_i(\boldsymbol{r}), \tag{2.29}$$

with an effective Hamiltonian

$$H_{eff}^{KS} = \frac{-\hbar^2}{2m}\nabla^2 + V_{eff}(\boldsymbol{r}) = \frac{-\hbar^2}{2m}\nabla^2 + V_H(\boldsymbol{r}) + V_{xc}(\boldsymbol{r}) + V_{ext}(\boldsymbol{r}). \tag{2.30}$$

Here, V_H is a Hartree Hamiltonian or classical Coulomb repulsion term, V_{ext} is an external potential and $V_{xc} = \frac{\delta E_{xc}}{\delta n(\boldsymbol{r})}$ is a non-classical term, known as exchange-correlation potential. The latter basically captures all electron-electron interactions beyond the Hartree-approximation. In particular, the exchange property is referred to the Pauli exclusion principle, whereas the correlation property is related to the interaction between the electrons not described in the Hartree-Fock theory. Among other parameters it is the exchange-correlation energy E_{xc}, which represents the most important part within the DFT which can be solved by several approximate schemes.

The local (spin) density approximation

In a non-uniform or rather inhomogeneous electron gas, the exchange-correlation potential V_{xc} at a point $\boldsymbol{r}$ not only depends on the density at the position $\boldsymbol{r}$, but also on its variation close to the position $\boldsymbol{r}$, which can be expressed by gradient terms. Therefore, the expansion in the gradients to arbitrary order of the density can be written [60] as

$$V_{xc}[n(\boldsymbol{r})] = V_{xc}[n(\boldsymbol{r}), \nabla n(\boldsymbol{r}), \nabla(\nabla n(\boldsymbol{r})), \ldots]. \tag{2.31}$$

Due to the involved gradients, an approximation to V_{xc} is difficult to find. As an approximation, a homogeneous electron gas is assumed, where the exchange-correlation energy depends only on the value of the density at the position $\boldsymbol{r}$. This approach is known as the *local density approximation (LDA)*.

In short, after the separation from the total energy, E_{xc} can be approximated by the following exchange-correlation functional, where the density is a slowly varying quantity

$$E_{xc}^{LDA}[n(\boldsymbol{r})] \equiv \int n(\boldsymbol{r})\epsilon_{xc}(n(\boldsymbol{r}))d\boldsymbol{r}. \tag{2.32}$$

Here, ϵ_{xc} is the exchange-correlation energy per particle in a homogeneous electron gas with the density n. The splitting of the energy ϵ_{xc} into the exchange and correlation contribution leads to separated energies $\epsilon_{xc}(n(\boldsymbol{r})) = \epsilon_x(n(\boldsymbol{r})) + \epsilon_c(n(\boldsymbol{r}))$. The exchange energy can be calculated from the Hartree-Fock theory for a homogeneous electron gas as the Dirac-Bloch exchange energy $\epsilon_x(n(\boldsymbol{r})) \propto n^{1/3}(\boldsymbol{r})$. In contrast, the correlation energy can only be approximated by a number of different approximations, such as Monte Carlo simulations [61], e.g. by means of the widely used numerical parametrization method proposed by Perdew and Zunger [62]. For spin-polarized systems, such as magnetic systems, two spin-densities $n^{\uparrow}(\boldsymbol{r})$ and $n^{\downarrow}(\boldsymbol{r})$ are taken into account for which the related exchange-correlation energies can be evaluated separately within the *local spin density approximation (LSDA)*. However, for strongly correlated systems, such as transition metal oxides and rare-earth metal compounds, where the d and f electrons are localized, the L(S)DA leads to unrealistic one-electron energies [63]. The L(S)DA neglects the orbital dependence of the Coulomb interaction. In order to overcome this problem, it is possible to introduce a Hubbard term U which accounts for the orbital dependence of the Coulomb $d-d$ and exchange interactions, which are not considered in the LDA [64] leading to the L(S)DA+U method.

The generalized gradient approximation

The *generalized gradient approximation (GGA)* is an alternative method for the calculation of the exchange-correlation energy functional and has been reported as an improvement of the L(S)DA, as it gives better total energies for molecular and strongly inhomogeneous systems. In particular, this method accounts for inhomo-

geneities of the investigated system and describes the ground state functional as a function of the density $n(\boldsymbol{r})$ and its gradient $\nabla n(\boldsymbol{r})$ [65]

$$E_{xc}^{GGA}[n(\boldsymbol{r})] \equiv \int f(n(\boldsymbol{r}), \nabla n(\boldsymbol{r}))d\boldsymbol{r}. \tag{2.33}$$

3 Experimental setup

The photoelectron spectroscopy experiments presented in this thesis were performed at two different vacuum ultraviolet (VUV) end-stations. This chapter summarizes the technical details of the instruments used. The spin- and angle-resolved photoemission measurements were carried out at the third generation synchrotron facility DELTA[1] using the VUV setup of beamline 5. In paragraph 3.1 the setup of the beamline will be discussed. In the same paragraph the newly developed magnetron sputtering system for UHV thin film deposition will be presented. Moreover, a laboratory based PES system was used, which provides excellent conditions to measure details of the band structure at high energy and wave vector resolution. In paragraph 3.2 the description of this system will be given.

3.1 DELTA beamline 5

The general outline of the synchrotron radiation beamline 5 is shown schematically in Fig. 3.1. The beamline is adapted to the planar electromagnetic undulator U250 which produces linearly-polarized light and is located in the north-east part of the storage ring. Among other optical devices, such as focusing and refocusing mirrors, a water-cooled plane-grating mirror monochromator (PGM) provides variable photon energies for the experiment and is designed for VUV and soft X-ray regime. The UHV monochromator tank hosts a combination of three tunable optical parts consisting of two plane gratings and a plane mirror. An incoming white beam impinges on a constant line spacing plane grating which acts as a dispersion element. High photon fluxes in the low photon energy range between 10 eV and 200 eV are covered by the 300 lines/mm grating. A second grating with 1200 lines/mm is used for higher photon energies between 200 eV and 1000 eV. The basic operation principle of a PGM can be found in Ref. [66]. The resulting photon energy of the monochrom-

[1] Dortmunder Elektronen Speicherring Anlage, Dortmund, Germany

atized beam is defined by the geometrical arrangement of the grating and the mirror which can be adjusted by remotely controlled stepper motor devices. Afterwards, the photon beam passes two mirror devices and finally reaches the photoemission experiment. In order to provide results comparable to the laboratory based system, the experiment was primarily optimized within the VUV regime around $h\nu = 24$ eV, i.e. tuned to high photon fluxes and an effective suppression of higher order radiation contributions. The second (and higher) order light, which is produced by the undulator, and allowed by the grating, produces unwanted background in the photoemission spectrum. The PGM allows the suppression of the second (and higher) order on the expense of intensity by setting the fixed-focus constant (cff), which is related to the arrangement of the mirror and grating angle.

In Fig. 3.2 a schematic overview of the experimental end-station is shown. The related photograph is provided in Fig. 3.3. The UHV system consists of three parts separated by manually operated valves. Here, two different preparation chambers labelled PREP I and PREP II were used for the preparation and characterization of the investigated materials. The photoemission experiments took place in the chamber labelled MAIN.

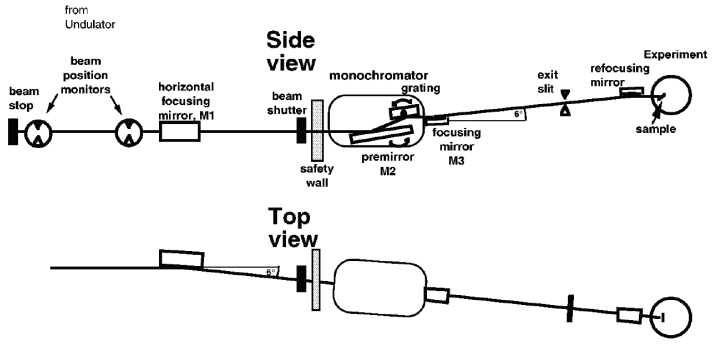

Figure 3.1: *Side- and top view drawings of the beamline 5 setup. Taken from [67]. The safety wall shields the radiation from the storage ring. The PES experiment is shown on the right.*

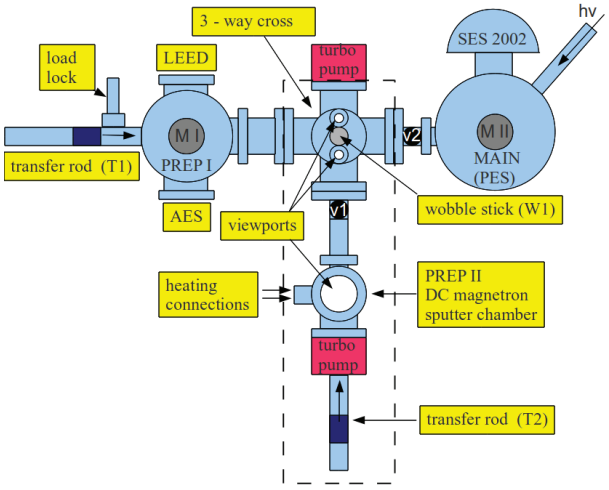

Figure 3.2: *General outline of the experimental end-station located at the beamline 5. The installed preparation chambers PREP I, PREP II and the photoemission vacuum setups are shown.*

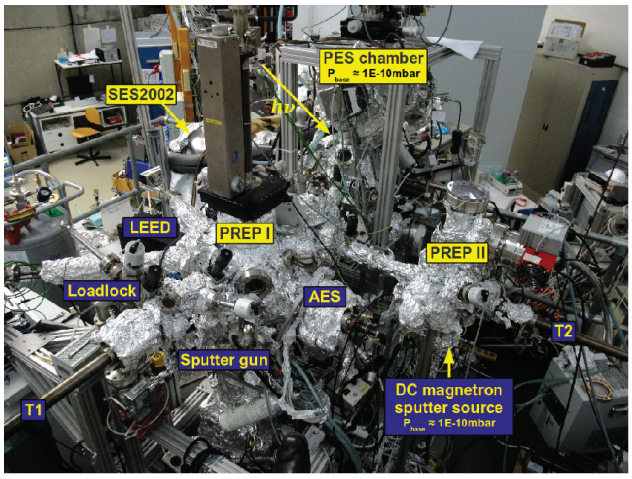

Figure 3.3: *Photograph of the experimental end-station consisting of two preparation chambers and a PES chamber.*

3.1.1 Sample preparation systems and characterization methods

The introduction of the samples from air into vacuum conditions is performed using a standard UHV load-lock setup. The entire setup uses an UHV Omicron-type sample transfer system. After being pumped to approximately $1 \cdot 10^{-7}$ mbar, the sample is transferred from the load-lock into a long transfer rod (T1). This device allows one to store seven samples inside a reservoir and is used for sample transfer between the three chambers.

PREP I chamber

The PREP I chamber is equipped with standard low-energy electron diffraction (LEED) and Auger-electron spectroscopy (AES) systems for surface analysis. It contains a 5-axis VG[2] manipulator including a current heated Tungsten filament for sample degassing and annealing purposes up to 600 °C. The temperature measurement is provided by using thermocouple sensors. Moreover, the sample surfaces can be cleaned by an Argon (Ar)-ion sputtering gun. This device allows the removal of adsorbed contaminants, such as Oxygen (O) or Carbon (C). Typical cleaning parameters of investigated samples will be given in the corresponding chapters 4 and 5 dealing with the preparation of topological insulating and half-metallic materials, respectively. In following the basic aspects of AES and LEED methods will be summarized.

Low-energy electron diffraction

LEED is a widely used technique to determine the structure of crystalline surfaces. Due to the short penetration depth of the involved electron beams LEED is a surface-sensitive method. The probing depth of electrons is limited by their short attenuation length defined by the inelastic mean free path, see chapter 2. A typical experimental setup is shown in Fig. 3.4. Being emitted by a cathode filament, the primary focused electron beam (0.1 mm to 0.5 mm) is accelerated with typical energies of 30 eV to 200 eV towards the sample surface, which is placed in front of a LEED screen. The impinging electrons interact with the two-dimensional (2D) periodic lattice surface, which represents a diffraction grating. The constructive

[2]VG Scienta, Sweden

interference of elastically backscattered electron waves and the 2D periodic lattice surface is given by the Laue condition

$$(\boldsymbol{k}^{||} - \boldsymbol{k}_0^{||}) = \boldsymbol{G} = h\boldsymbol{a}^* + k\boldsymbol{b}^* \quad (h,k = 0,1,2...), \tag{3.1}$$

with the primitive translational reciprocal vectors $\boldsymbol{a}^*, \boldsymbol{b}^*$, a set of integers h, k and the reciprocal lattice vector $\boldsymbol{G}$. $\boldsymbol{k}_0^{||}$ and $\boldsymbol{k}^{||}$ denote the parallel wave vectors components of the impinging and the scattered electrons, respectively. According to this, backscattered electrons imaged onto a fluorescence screen form a distinct array of diffraction spots reflecting the crystallographic orientation of the sample. In normal incidence geometry, the scattering process is visualized by using the 2D Ewald sphere representation, shown in Fig. 3.4. The allowed diffraction spots are then related to defined intersections between the 2D reciprocal lattice, which is shown as a set of rods, and the constructed Ewald sphere with a radius of $|\boldsymbol{k}_0^{||}|$.

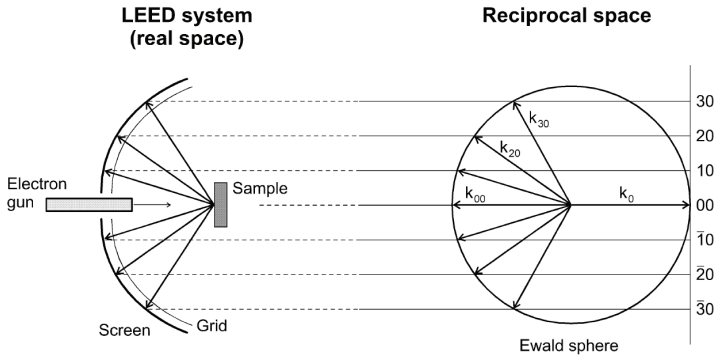

Figure 3.4: *Left side: Basic outline of a LEED device consisting of an electron gun and a detection screen in front of a sample in real space. Right side: Schematic representation of the Ewald sphere construction for LEED in the reciprocal space. The sketch was adapted from [68].*

Auger electron spectroscopy

The Auger electron spectroscopy (AES) method is based on a radiationless electron emission process, which yields the chemical composition with an information depth of few Å below the surface. The underlying physical process relies on the ionization

of a core level by using either electron or photon beams. Photon induced Auger electrons are commonly observed in XPS/ESCA studies. In following only the Auger process induced by incident electrons, as available in the most standard UHV characterization systems, will be discussed. A conventional AES system consists of an electron gun and a cylindrical mirror analyzer mounted in an UHV chamber. In contrast to LEED, higher energy incident electrons of $3 - 5$ keV are used. AES measurements will be presented in the chapters 4 and 5.

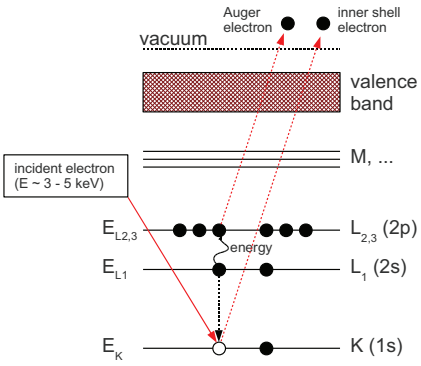

Figure 3.5: *Schematic illustration of the Auger electron emission process. The related spectroscopic notation of the involved transitions are given.*

The ionization of a core state may result in an electronic rearrangement which leaves the atom in a doubly ionized state [69]. For the example given in Fig. 3.5, the created hole within the 1s core level is first filled by a 2s electron transferring the remaining transition energy to an outer shell electron, which is emitted, for example from the 2p level with a characteristic kinetic energy related to its parent atom. More precisely, one can think about the absorption of a virtual photon by the outer electron leading to the Auger emission process. In spectroscopic notation, the transition types are labelled as KLL, LMM and MNN reflecting the transition sequences starting with the core level hole state K, the electron relaxation and the final emission of an Auger electron. In this particular example the kinetic energy of Auger electrons related to a KLL transition is therefore given by

$$E_{kin} = E_K - E_{L_1} - E_{L_{2,3}}. \tag{3.2}$$

PREP II chamber: DC magnetron sputtering method and apparatus

Within the framework of this thesis an additional UHV system has been installed. This contains a direct current (DC) magnetron sputter source device. The new setup opens the possibility of an *in situ* thin film deposition of various materials, such as Heusler alloys, on selected substrates. In the case of the TIs a radio-frequency (RF) power supply should be used [70].

The general outline of the instrument is displayed in Fig. 3.2(a), where the main parts of the new setup are framed by the dashed line. The system is connected via a gate valve (v1) to the first preparation chamber (PREP I) and the photoemission chamber (MAIN), and is pumped by a turbomolecular pump[3]. The central part is the UHV vacuum tank (PREP II), which is equipped with an UHV based planar magnetron sputter source of 2 inches in diameter manufactured by TFC[4]. Moreover, there exists a rotatable long-travel transfer rod (T2) which is able to move the sample *in situ* between the PREP II chamber and the 3-way cross. On top of the latter two viewports and a wobble stick device (W1) were installed. The Omicron-type sample stage is mounted on the T2 part, and includes a vacuum compatible rectangular Boron Nitride (pBN)[5] heating element (max. current 16 A, power ca. 1440 W), see Figs. 3.6(a) and (b). The base pressure of the new system is around $p \sim 1 \cdot 10^{-10}$ mbar. For the deposition of Co_2CrAl thin films a two inch stoichiometric sputter target with a purity of 99.999 %[6] was used. The target material was bonded to a Cu plate via an Indium (In) layer. The bonding increases the thermal conductivity of the entire target stack. Since the melting temperature of In is around 150 °C, it is recommended not to use higher temperatures during the bake-out process. Prior to the first thin film deposition, a distance of 73 mm between the source and the sample holder has been optimized by means of a growth rate control using a water-cooled quartz thickness monitor adapted to the PREP II chamber. The measured growth rate varied between 0.5 - 0.7 Å/s. An exact value can be obtained from a reflectivity measurement yielding the thin film thickness.

[3] HiPace™300, Pfeiffer Vacuum GmbH, Germany
[4] Type ION'X-2UHV, Thin Film Consulting GmbH, Grafenberg, Germany
[5] Boralectric, Germany
[6] MaTecK GmbH, Germany

In following, a brief description of the magnetron sputtering method are presented. The experimental results of the thin film deposition will be shown in chapter 5.

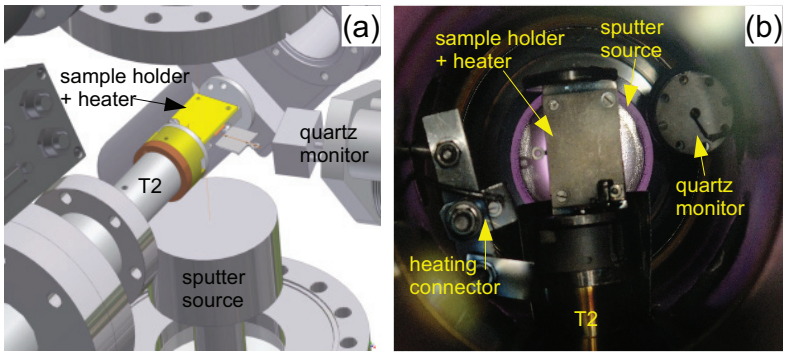

Figure 3.6: *Technical drawing (a) and photograph (b) of the magnetron sputter device area. The sample is mounted on a standard Omicron-type sample holder system, which is adapted to a ceramic heating plate. The entire sample holder assembly is fixed via an insulated mounted Cu-cylinder on the transfer rod T2 and positioned above the 2 inch magnetron sputter source. The heating connection as well as the quartz monitor are shown.*

DC magnetron sputtering

Magnetron sputtering is a well-established physical vapour deposition (PVD) technique widely used in industrial as well as in scientific applications. Sputter deposition is a process, where atoms are first ejected from a stoichiometric target material and finally coat a substrate material. A typical magnetron sputter process is shown in Fig. 3.7. The main parts of magnetron sputter system are the sputter source, which acts as cathode and a substrate material which represents the anode. The creation of a plasma, caused by a DC high-voltage induced ionization of inert gas atoms, e.g. pure Ar-ions, initializes the sputtering process. Here, the ionized gas atoms are accelerated towards the sputter target consisting of the elements which will form the thin film. The bombardment of the target material leads to a ballistic ejection of the desired elements which subsequently coat the substrate. In particular, sputtered atoms leave the target surface with relatively high energies and velocities and initially intermix into the atomic lattice of the substrate surface [71]. The sputter efficiency is highly increased by using a toroidal magnetic field on the target surface,

which confines the plasma by trapping secondary electrons on defined trajectories and thus enables a sustainable glow discharge. This leads to more collisions between the electrons and the gas atoms. Hence, the amount of ions increases which results in higher sputter and growth rates. For this reason, a typical planar magnetron device contains a built-in array of permanent magnets producing a magnetic field of several mT.

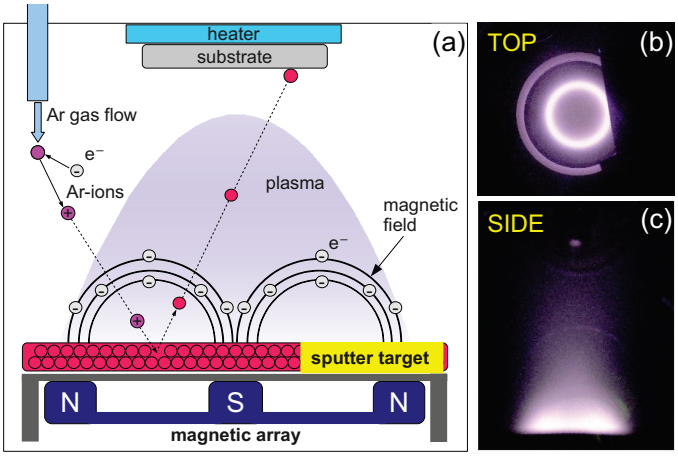

Figure 3.7: *(a) General outline of the magnetron sputter deposition process. Here, the ignition of a plasma induces the main mechanism, where Ar-ions start the bombardment of a stoichiometric target material. The sputter efficiency is enhanced by an electron trapping torodial magnetic field produced by permanent magnets located below the sputter target. The substrate material is placed above the sputter source and is covered by the atoms ejected from the target. (b) Top and (c) side view photograph of the created plasma during a typical in situ sputter deposition captured within the PREP II chamber.*

Due to the conservation of energy, a neutralization of residual gas ions by free electrons results in a release of photons appearing in a characteristic glowing of the plasma observable during the sputter process, see Fig. 3.7(b). As can be seen, there exists a circular area, from which the target material is preferentially ablated. This non-uniformity of erosion is a direct consequence of the electron travelling path [71]. In detail, the electrons confined by magnetic fields are accelerated to a drift velocity that is orthogonal to both the direction of the electric field and the magnetic field in the vicinity of the target surface. Hence, emitted secondary electrons lead to additional ionization processes of the Ar atoms resulting in higher sputter rates

especially close to the circular path on the target surface. As a consequence, most of the target material remains 'unused' while efficient sputtering takes place along the described path.

Besides of the ability to deposit the materials at high constant rates (up to few nm/s), this method has proved to be advantageous for the deposition of stoichiometric compounds defined by the stoichiometry of the sputter target. In thermal evaporation techniques the deviating film composition is influenced by the element specific vapour pressure of the evaporants. This is not the case in magnetron sputtering, where only atoms located near the surface are sputtered from the target. A faster ejection of one element would leave the surface enriched with the others, effectively counteracting the difference in sputter rates [72]. On the other hand, due to the fixed chemical stoichiometry the usage of a single sputter deposition source restricts the possibility of a variation in the chemical composition of the desired material. However, a preferential sputtering is possible if the atomic masses of a multicomponent target differ considerably from each other, which leads to an off-stoichiometry of the thin films. In the particular case of the Co_2CrAl compound used in this work, this effect can be neglected due to the relatively small mass differences of the constituent elements and the usage of Ar-ions during the process.

3.1.2 The photoemission system

The state-of-the-art photoemission system is housed in an UHV chamber (MAIN), see Fig. 3.2. It includes a VG Scienta SES-2002 hemispherical spectrometer customized with a combination of an optimized high transmission spin-polarized low-energy electron diffraction (SPLEED) based detector[7] [73, 74] as well as a two-dimensional delay-line detector (DLD) system[8]. The general outline of the installed equipment is shown in Fig. 3.8.

Compared to a standard multichannel-plate (MCP) scintillator-CCD design, the DLD operates without any viewport or CCD camera. This makes it convenient to fit into the area crowded with the MCP and the electron transfer optics for the spin-detector [75]. In this configuration the simultaneous detection of a 1D spin-resolved energy-distribution curve (EDC) and 2D angular map of dispersive band structures as well as Fermi surfaces is possible.

[7] Manufactured by FOCUS GmbH, Germany.
[8] Surface Concept GmbH, Germany

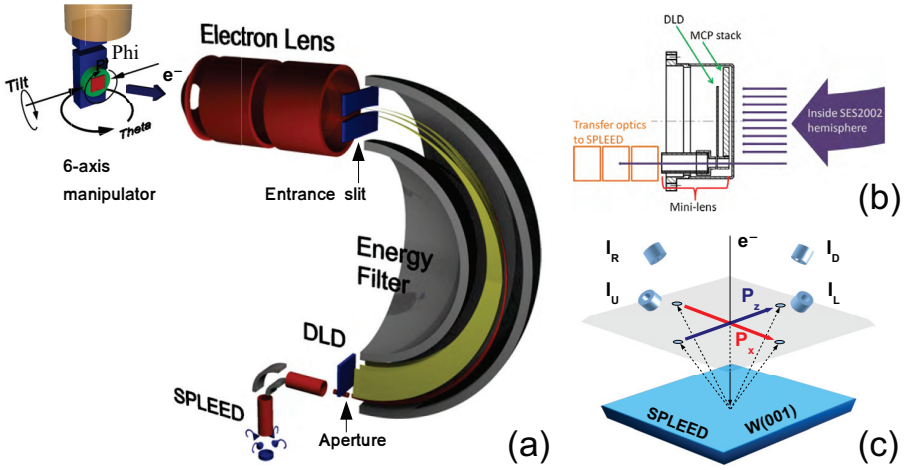

Figure 3.8: *Schematic representation of the photoemission apparatus installed at beamline 5. (a) The sample is mounted on a six-axis manipulator. Excited photoelectrons are focussed onto the entrance slit of the hemispherical SES-2002 analyzer system. The angular distribution of electrons according to their kinetic energy is measured with the 2D DLD. Another part of the electrons is transferred onto a W(001) scatter target by using a* 90° *deflector. The partial intensities containing the spin information are measured by four channeltrons surrounding the crystal. (b) A more detailed representation of the 2D angular detector. It is characterized by the MCP stack and the DLD assembly. Taken from [75]. (c) A more detailed representation of the SPLEED detector. The channeltrons allow to detect the in- and out-of-plane spin vector components (P_x and P_z) in a simultaneous way. The partial scattered beam intensities are denoted as I_L, I_R, I_U and I_D.*

In order to enable Fermi surface or constant energy surface mapping measurements, a six axis manipulator (MII)[9] was implemented into the PES chamber, and replaced an older version manipulator with less degrees of freedom. It is compatible with Omicron-type sample holder system and allows cryogenic cooling. Besides the x, y and z translational directions, there exist additional three rotational degrees of freedom in polar (ϑ), azimuthal (φ) and tilt (α) rotation directions, see inset Fig. 3.8(a). With the exception of the x and y directions, the movements are remote controlled. In reference to the horizontally positioned entrance slit of the analyzer, which sets the angular acceptance area of the photoelectrons, the sample tilt opens the possibility of a $\boldsymbol{k}$-space Fermi surface mapping.

[9]The design was developed in IFW Dresden, Germany. Currently the manipulator is commercialized by VG Scienta.

For the spin polarization analysis on 3D TIs a prerequisite Fermi surface mapping is mandatory in order to define the desired emission areas within the reciprocal space, which carry the informations about the spin-helicity of the surface localized states. Thus, prior to the measurements using the spin-sensitive SPLEED detector, the Fermi surfaces of Bi_2Te_3 and Sb_2Te_3 have been obtained by measuring the set of ARPES maps for a range of tilt angles. The general outline of the sample and experiment geometry used for SP-ARPES measurements at beamline 5 is shown in Fig. 3.9. The incidence angle of the incoming linearly-polarized photon beam is 50° with respect to the sample normal. A typical Fermi surface mapping result from a clean Bi_2Te_3 thin film surface is plotted on top. For this purpose, the sample was rotated around the x-axis by changing the tilt angle in 0.25° steps while several $E_B(\boldsymbol{k})$ angular maps were taken at different emission angles. The duration of such $\boldsymbol{k}$-space mapping was about one hour. A final merging of the angular maps for a selected binding energy E_B leads to a constant energy surface, and for the particular case of $E_B = 0$ eV to the Fermi surface. The corresponding surface Brillouin zone (SBZ) is plotted on top of the schematic sample surface. The *in-plane* P_x and *out-of-plane* P_z spin vector components being monitored by the SPLEED detector are shown. During the data acquisition the cryostat was cooled by liquid nitrogen.

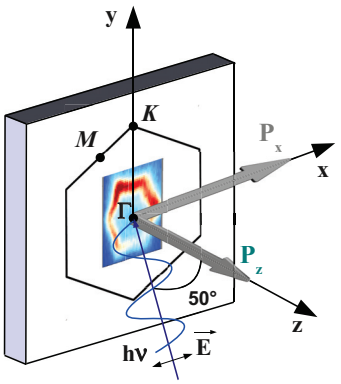

Figure 3.9: *Sketch of the sample geometry with respect to the linearly-polarized photon beam, characterized by the electric field vector* $\boldsymbol{E}$ *and a photon energy* $h\nu$*. The spin vector components* P_x *and* P_z *being detected by the SPLEED detector are indicated by grey arrows. The hexagonal SBZ is plotted on top of an experimental* Bi_2Te_3 *Fermi surface. The dimensions are not to scale.*

Hemisperical electron analyzer

After the photoemission process the emitted photoelectrons enter a lens aperture. The angular emission range of the electrons is defined by an electrostatic lens system,

which can operate either in imaging or angular dispersive mode, depending on the lens voltage settings. In angular dispersive mode, used in this work, the electron lens produces the angular distribution along the entrance slit of the hemispherical energy filter. The typical angular resolution of the analyzer is between 0.3° and 0.4°. Furthermore, the lenses match the initial kinetic energy of the electrons to the pass energy E_{pass} of the electron analyzer [76]. Subsequently, a concentric 180° capacitor arrangement with a mean radius of $R = 200$ mm, consisting of an inner and an outer hemisphere, allows the filtering of electrons as a function of their kinetic energy E_{kin}. The electrons entering the hemispheres with the kinetic energy equal to the pass energy E_{pass} will be transmitted along the center trajectory, electrons with higher kinetic energies will be deflected towards the outer sphere, whereas those with lower kinetic energies approach the outer hemisphere. An even potential distribution is provided by a graphite coating of all surfaces seen by the photoelectrons. The final image depends on the selected entrance slit curvature which can be set either straight or curved shaped. Electrons passing through a straight entrance slit, will be detected as a curved line at the detector due to the spherical symmetry of the analyzer. Although a curved entrance slit will provide straight lines, the image is related to electrons coming from a curved line on the sample. For the case of the angular mode it is related to a curved line in the surface Brillouin zone. In order to avoid any influences caused by external magnetic fields, the electron lens and the analyzer are surrounded by outer μ-metal[10] shields.

The energy resolution ΔE of the analyzer depends on the width of the analyzer entrance slit W_{slit}, the pass energy E_{pass}, the mean radius R and the angle of incidence α and can be approximated by

$$\Delta E = E_{pass}\left(\frac{W_{slit}}{2R} + \frac{\alpha^2}{2}\right) \approx E_{pass}\frac{W_{slit}}{R}. \tag{3.3}$$

Here, the α term can be controlled by an additional aperture in front of the slit which is positioned away from the focal point and therefore controls the incidence angle. The spectrometer is typically designed in such a way that $\frac{\alpha^2}{2} \approx \frac{W_{slit}}{2R}$. However, the real energy resolution of the experiment is limited due to the Fermi-Dirac statistics of the electrons, which will be explained by means of high-resolution measurements in paragraph 3.2.

[10]Typical μ-metals are Ni-Fe alloys showing a high magnetic permeability.

In the framework of this thesis, the ARPES studies were carried out at a laboratory based system described in paragraph 3.2. The measurements were typically performed at a pass energy $E_{pass} = 5$ eV and a slit width of $W_{slit} = 0.4$ mm leading to energy resolutions $\Delta E < 10$ meV, while the SPLEED experiments were done at $E_{pass} = 20$ eV with a resolution of $\Delta E \sim 150$ meV. Additional ARPES band mapping at beamline 5 was performed at $\Delta E = 50$ meV. Typical analyzer entrance slit and aperture settings used at beamline 5 are given in table 3.1.

Mode	Slit width [mm]	Slit length [mm]	Aperture width [mm]	Aperture length [mm]	Shape
ARPES	0.5	25	1.9	30	Curved
SP-PES	1.5	30	3.2	30	Straight

Table 3.1: *Entrance slit geometries used either in angle-resolved or spin-polarized PES modes.*

Delay line detector

The 2D detector system comprises an MCP stack and a *meander* DLD placed behind, see Fig. 3.8(b). The incoming electrons are amplified by at least 10^7 by the MCP stack of 27.5 mm (energy direction) x 30 mm (angular) active dimensions. The detection principle of the produced electron ensemble involves the measurement of induced electrical pulses in the DLD anode printed on a PCB plate consisting of two meander structured delaylines operating in a capacitive mode. A fast amplifier device as well as complex pulse processing units allow the conversion to 2D $E(\boldsymbol{k})$ images covering an angular range of approximately 15°. For more details see Ref. [77]. Furthermore, it is possible to perform stroboscopic experiments in a 2D time resolved mode. The latter mode was not used in the experiments shown in this thesis.

SPLEED detector

In order to perform spin-polarized measurements an additional electron transfer optics has been integrated within the SES-2002 detector area [75]. The experimental setup of the SPLEED detector system is sketched in Figs. 3.8(a) and (c). Here, one part of the photoelectron beam which exits the analyzer enters a mini-lens which is

placed 24 mm off-center (towards the outer hemisphere). The overall spin detection area is defined by the choice of the entrance slit aperture width (see table 3.1) and the fixed mini-lens entrance. The angular integration over the circular aperture of the optics entrance (⌀5 mm circular opening) is related to approx. 3.2° electron emission angle. Being transferred by the first Einzel lens, the electrons pass through a 90° deflector which employs a spherical electrostatic field, that is simulated by cylindrical electrodes [78]. This arrangement enables the measurement of the spin polarization vector components P_x and P_z in the *in-plane* and *out-of-plane* directions. Finally, the beam is focused by a second Einzel lens and transferred to the W(001) detector crystal. Further details and characterization of the SPLEED polarimeter setup can be found in Ref. [75].

The spin analysis is based on a spin-dependent electron scattering caused by spin-orbit interaction. In particular, the incoming spin-polarized beam is focussed on a W(001) scattering target, where it is finally scattered with a kinetic energy $E_{kin} = 104.5$ eV. Since the scattering process of an electron beam from a high Z target is spin-dependent due to SOC, the scattering potential causes a left-right asymmetry of the backscattered beams [79]. In absence of apparatus-related asymmetries, the basis expression for the spin polarization value is given as

$$P = \frac{1}{S}\frac{N_A - N_B}{N_A + N_B}, \tag{3.4}$$

where the function S is a detector specific parameter, known as Sherman function [22, 80]. This quantity reflects the instrument ability to distinguish different spin states, which is determined by the scattering conditions. In other words, the spin asymmetry function S represents the spin-resolving efficiency of the polarimeter. N_A and N_B are related to the partial intensities of the diffracted beams. More precisely, the intensities of the corresponding different spin vector orientations can be detected in opposite aligned channeltron elements, positioned in the (2,0), (0,2), ($\overline{2}$,0) and $(0, \overline{2})$ diffraction directions, which lead to two normalized intensity asymmetry values related to the *in-plane* and *out-of-plane* spin components, respectively:

$$A_x = \frac{I^{\uparrow}_{20}(E) - I^{\downarrow}_{2\overline{0}}(E)}{I^{\uparrow}_{20}(E) + I^{\downarrow}_{2\overline{0}}(E)} \quad \text{and} \quad A_z = \frac{I^{\uparrow}_{02}(E) - I^{\downarrow}_{0\overline{2}}(E)}{I^{\uparrow}_{02}(E) + I^{\downarrow}_{0\overline{2}}(E)}, \tag{3.5}$$

where $\uparrow, \downarrow$ denote the spin-up and spin-down electrons. Moreover, the channeltron intensities are often indicated by a left-right $I_{L,R} (= I_{20,2\overline{0}})$ and up-down $I_{U,D} (= I_{02,0\overline{2}})$

channel scattering nomenclature related to the geometrical arrangement within the SPLEED system, see Fig. 3.8(c). The spin polarization values can be obtained from

$$P_{x,z} = \frac{1}{S} \cdot A_{x,z}. \tag{3.6}$$

The error of the measured polarization is small when the figure of merit, which is defined as $P^2R = S^2\frac{I}{I_0}$, takes high values. Here, R is the reflectivity, whereas I_0 and I represent the intensity of the incident and scattered electron beam, respectively. In the case of the Focus SPLEED detector, there exists a maximum value of the figure of merit at the scattering energy of 104.5 eV, which is used for the diffraction by the W(001) single crystal for all spin-polarized measurements.

In the case of ferromagnetic materials the spin moments are aligned along a specific quantization axis which is defined by the magnetization direction of the sample. Therefore, spin-resolved photoemission from ferromagnets are usually obtained from a remanently magnetized sample. In order to remove apparatus asymmetries, the final spin-polarization is computed from two different measurements with sample being magnetized either in 'plus' ($I^+_{L,R}$) or 'minus' ($I^-_{L,R}$) direction. Hence, this procedure eliminates instrumental asymmetries originating from a misaligned beam of the electrons. The expression for the *in-plane* spin polarization vector component is then given by

$$P_x = \frac{1}{S} \cdot \frac{\sqrt{I^+_L \cdot I^-_R} - \sqrt{I^-_L \cdot I^+_R}}{\sqrt{I^+_L \cdot I^-_R} + \sqrt{I^-_L \cdot I^+_R}}. \tag{3.7}$$

It should be noted, that the above equation uses geometrical mean values of the count rates which account for different detector sensitivities. An arithmetical mean value is used in situations where one of the channels I_L or I_R is suspected to have a constant offset in count rate [81]. For the *out-of-plane* component the left-right $I_{L,R}$ intensities are replaced by the up-down $I_{U,D}$ intensities. Knowing the polarization value, the constituent intensities can be written in terms of $I_L = 0.5 \cdot I_{sum} \cdot (1 + P)$ and $I_R = 0.5 \cdot I_{sum} \cdot (1 - P)$, with $I_{sum} = I^+_L + I^-_R + I^-_L + I^+_R$. For non-magnetic materials, e.g. TIs, we will use a general version of eq. 3.5 given as

$$\Rightarrow P = \frac{1}{S} \cdot \frac{I^{\uparrow} - I^{\downarrow}}{I^{\uparrow} + I^{\downarrow}}, \tag{3.8}$$

with $I^{\uparrow,\downarrow}$ indicating either a left- or a right-handed movement of the spin vector along the constant energy surfaces.

Prior to the spin-polarized measurements the W(001) crystal of the SPLEED detector has been prepared in order to obtain well-defined diffraction patterns at the electron detectors as well as to attain a high spin asymmetry. A sufficient cleaning was obtained by flashing the crystal up to a temperature of $T = 2300$ K where the amount of tungsten oxides has been removed. The crystal was heated with a power of about 250 W for about 20 sec. [78]. This procedure was repeated again after about 5 hours in order to prevent the degradation of the crystal during the measurements. The experimental results will be presented in chapter 4.

3.2 Laboratory based PES system

The laboratory based PES system is located at the Peter-Grünberg-Institute PGI-6, Research Centre Jülich. The general outline of the laboratory system is shown in Fig. 3.10(a).

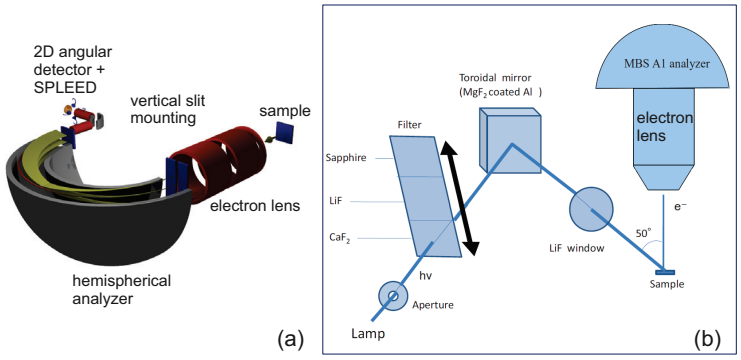

Figure 3.10: *(a) Sketch of the laboratory based photoemission system with a vertical analyzer slit mounting. (b) Schematic view of the optical system consisting of different ionic crystal filters, and electron-cyclotron resonance plasma discharge source as well as a He-lamp. Taken from [82].*

The UHV setup is equipped with the standard AES and LEED characterization methods. The base pressure of the system is better than $5 \cdot 10^{-11}$ mbar. Two gas discharge sources act as photon sources. In detail, different photon energies are provided by a laboratory Helium (He I: $h\nu = 21.2$ eV, He II: $h\nu = 40.8$ eV) lamp[11] and a resonance plasma discharge source, which can be operated with various

[11]SPECS, Surface Nano Analysis GmbH, Germany

gases such as Krypton ($h\nu$ = 10.03 eV), Argon ($h\nu$ = 11.6 eV) and Xenon (Xe $h\nu$ = 8.44 eV). The discharge lamps are combined with three crystal filters, here sapphire, CaF_2, and LiF, which monochromatize the incoming beam by filtering out all photons with energies above the fundamental gaps of the filters. More details can be found in Ref. [82]. Due to its permanent availability, this instrument can be alternatively used during synchrotron shutdown periods. Unlike in the beamline 5 setup, the hemispherical analyzer of type MB Scientific A-1[12] is rotated by 90° as shown in Fig. 3.10(a). The resulting vertical slit entrance opens the possibility of Fermi surface measurements, which can be performed by means of a sample rotation using the polar degree of freedom of the cryostat cooled manipulator. The experimental results will be presented in chapter 4.

Besides the continuous beam availability, this system allows the measurement of high resolution ARPES data. Following eq. 3.3, the theoretical analyzer resolution using a pass energy of E_{pass} = 2 eV and a slit width W_{slit} = 0.2 mm is approximately 2 meV. In a real experiment, however, the thermal broadening due to the Fermi-Dirac distribution of electrons

$$f(E) = \frac{1}{e^{\frac{E-E_F}{k_B T}} + 1}, \tag{3.9}$$

where $k_B = 1/11600\ eVK^{-1}$ is the Boltzmann constant, has to be considered. Typically, such as in the present case, the entire experiment is limited by the resolution due to the sample temperature, and less due to the analyzer resolution. Due to the high sharpness of the Xe, Kr, Ar, and He lines, the photon energy width contribution to the resolution is below 1 meV and will be neglected. According to this, it is possible to determine the energy resolution by a fitting procedure of the Fermi edge. For this purpose, a cold metallic solid, such as Au, Ag or Cu can be used as test materials. Fig. 3.11 shows the experimental Fermi edge of a He-cooled Cu(111) single crystal surface obtained at $h\nu$ = 10.03 eV at the analyzer resolution of approximately 2 meV. The red line indicates the non-linear fitting curve of the Fermi function. The dx value of 1.52 meV is related to the k_BT term of the Fermi Dirac statistics, which leads to a sample temperature of $T^{fit} = (17.6 \pm 0.4)$ K. Finally, the

[12]MB Scientific AB, Sweden

energy resolution can be expressed from a simple model as the total full-width at half maximum (FWHM) of the Fermi function

$$\Delta E \simeq 4 \cdot k_B T^{fit} = (6.08 \pm 0.15)\ meV. \tag{3.10}$$

Alternatively, it is possible to convolute the Fermi-Dirac function with a Gaussian and also to consider broadening contributions, such as the photon energy width, see Ref. [18].

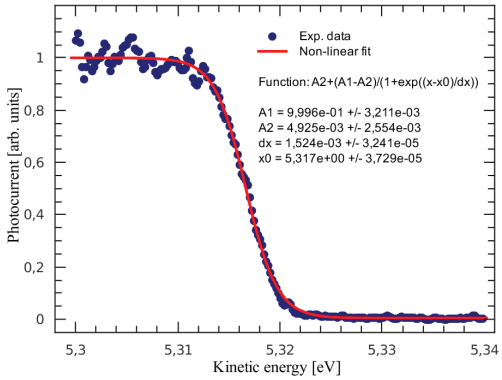

Figure 3.11: *Fermi edge of a clean helium cooled Cu(111) sample measured at* $h\nu = 10.03$ *eV using the sharp Kr emission line. The red line represents the Boltzmann distribution fitted to the data points. The corresponding fitting parameters are given. The total FWHM of 6.08 meV validates the high resolution of the laboratory photoemission system at low sample temperatures around 15 K.*

A typical high resolution measurement is shown in Fig. 3.12(a). The angular map shows a normal emission measurement of a bulk Bi_2Se_3 crystal. This data clearly shows the well known V-shaped surface state and the crossing point at the Brilloiun zone center $|\boldsymbol{k}_\parallel| = 0$ Å^{-1}, known as Dirac point [83]. Fig. 3.12(b) depicts further ARPES scans on the Cu(111) surface state carried out at different photon energies using the Xe, Ar and Ar excitation energies and sample temperatures around 90 K.

More recently, a SPLEED detector was installed behind a 90° deflector similar to the synchrotron based photoemission system, which opens up new possibilities of high-resolution spin-resolved photoemission studies on single crystal and thin film material systems. In the near future the laboratory system will be upgraded

by a newly developed FERRUM[13] spin detector, which is based on the exchange scattering of electrons on a magnetized and oxygen-passivated iron film with details described in Ref. [84]. One of the advantages is its large figure of merit being at least one magnitude compared to the existing SPLEED detector ($S^2 I/I_0 \sim 2 \cdot 10^{-4}$).

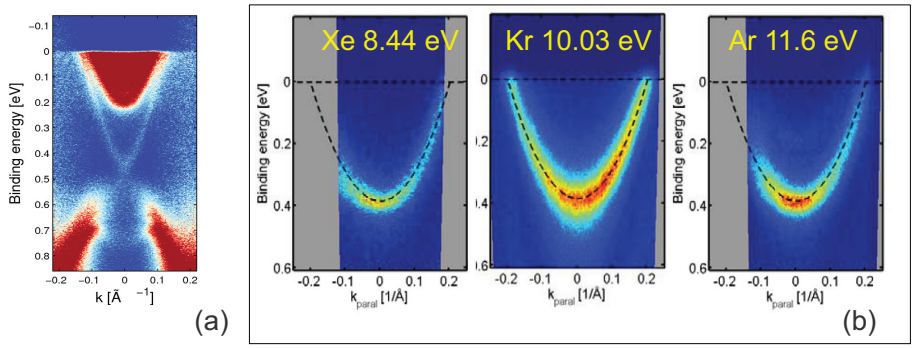

Figure 3.12: *High-resolution ARPES maps taken using the laboratory based PES system. (a) Normal emission $E_B(k)$ map of a bulk 3D TI Bi_2Se_3 sample taken at $h\nu = 21.2$ eV using the He I excitation line with sample kept at 15 K. (b) ARPES of a surface state measured on a sputter-annealed clean surface of Cu(111) at 90 K by using different discharge photon sources. Taken from [82].*

[13]Focus GmbH, Germany

4 Topological insulators

4.1 Introduction

In condensed matter physics phase transitions occurring in crystalline solids, magnets, or superconductors are traditionally characterized by a sudden change of the involved translational, rotational and gauge symmetries [85]. The invariance of a system under a certain symmetric transformation is described by means of an invariant Hamiltonian. For many years the phenomenological Landau theory of phase transition, which was developed in 1937 [86], has been successfully used to classify the different states of matter formed by a broken symmetry.

However, the situation has changed considerably with the experimental discovery of the Integer Quantum Hall effect (IQHE) by Klitzing *et al.* in 1980 [87], which has attracted a great interest in many scientific research fields of condensed matter physics, high energy physics, atomic physics and astrophysics [88]. Herein, the application of an external magnetic field to a confined two-dimensional electron gas (2DEG) leads to the occupation of quantized Landau energy levels and induces an integer quantized Hall resistance which can be measured from semiconductors, whereas very low temperatures ($\sim$ 1.5 K) and high magnetic fields of several Tesla are needed. As a result, the transverse magneto-conductance takes extremely precisely quantized values. It could be shown, that the resulting QH states could only exist at the edges of the sample where impurity scattering is suppressed [85,89]. The insensitivity of the states to local perturbations such as defects, disorder or thermal fluctuations was affiliated to the absence of a spontaneously broken symmetry. Therefore, the QH states were referred to a new state of matter, so-called topological phases [90]. For periodic lattices being discussed in topological band theory, Thouless, Kohmoto, Nightingale and den Nijs *et al.* [90] classified the integer QHE by means of a topological order, known as Chern number C_n, which determines the precise quantization of the QH conductivity. In particular, the geometric interpre-

tation of the Hall conductance is given by the connection of the geometrical and topological properties.

Motivated by the theoretical descriptions [91, 92] of an intrinsic spin Hall effect and its experimental confirmations on n-doped and p-doped semiconductors [93,94], 2005 Kane and Mele [95] proposed the existence of distinct Quantum Spin Hall (QSH) phases in a two-band model of graphene. Within this model the time-reversal invariant QSH state system is attributed to a topological invariant index $\mathbb{Z}_2$ which is basically an analogue to the aforementioned Chern number C_n, and allows the discrimination between an ordinary band insulator and a QSH state. In 2D the QSH state is a close cousin of the integer QH state. Unlike in the QHE, the mechanism of the QSHE relies on strong SOC effects yielding time-reversal invariant phases which replaces high magnetic fields for their existence.

2D QSH states in graphene, as proposed by the Kane and Mele [95] model, however, did not show up in reality since it turned out that in graphene the SO gap is of the order of 10^{-3} meV, yielding QSH states only at unrealistically low temperatures [96, 97]. These works initiated a tremendous search for new non-trivial topological states of matter within the global scientific community. In the course of the search for a real QSH system, Bernevig *et al.* [98] predicted the existence of a 2D topological insulating state in a mercury telluride-cadmium telluride (HgTe-CdTe) semiconductor quantum well system. The experimental confirmation of this theory was provided by König *et al.* [99]. Briefly, it was shown that the QSH state appears in a certain region of a HgTe-CdTe quantum well. Due to a strong SOC, the QSH states can exist without the need of an external magnetic field forming states with opposite spin vector orientations counterpropagating along the sample edges.

Shortly after the theoretical and experimental investigation of the 2D topological insulating HgTe quantum well phase, the first 3D TI was theoretically predicted [100] and experimentally observed by means of ARPES measurements on the $Bi_{1-x}Sb_x$ phase [101, 102]. The models describing the 2D and 3D TIs are very similar. In both, the underlying physical properties of the electronic structure is influenced by the presence of a strong SOC giving rise to unique edge and surface states, respectively. A layered 3D version of the QSH insulator Hg(Te)Cd represents a *weak* 3D TI with an even number of surfaces states, however, which are not robust against induced disorder [103]. Instead of the edge states, in 3D one deals with highly spin-polarized surface states which have potential properties for future spintronic

applications. The SO induced surface states residing in a bulk energy band gap are considered as higher-dimensional analogues of the edge states that characterize a QSH insulator [101, 104]. The generalization of the QSH state to 3D TIs has been theoretically described by Fu *et al.* [105] and experimentally confirmed by means of ARPES measurements on several 3D topological insulating materials [83, 101, 106–108]. More recently, various types of ternary half-Heusler alloys, such as XPtBi (X = Lu,Dy,Gd), were predicted to show a SOC induced band inversion process near the Fermi level [9, 10].

In following, the properties of 3D TIs will be introduced with the emphasis on the SOC effects explained in paragraph 2.1.2. The results will be evaluated with the aid of the dedicated theoretical *ab initio* bulk and surface calculations performed within this framework, see paragraph 4.2. The experimental results comprising the preparation of Bi_2Te_3 and Sb_2Te_3 thin films, the investigation of spin- and angle-resolved photoemission spectra and the direct comparison to dedicated thin film DFT calculations will be shown in paragraph 4.3. The chapter closes with final conclusions.

4.2 3D TIs: Bi_2Te_3 and Sb_2Te_3 compounds

In contrast to $Bi_{1-x}Sb_x$ the second-generation of 3D topological insulating materials composed of Bi_2Se_3, Bi_2Te_3 and Sb_2Te_3 shows a rather simplified electronic structure characterized by single-branched Dirac cones as proposed by Zhang *et al.* [1]. Due to their high thermoelectric figure of merit and relatively high Seebeck coeffecients, these materials have been initially studied as thermoelectric materials, and have been widely used in industrial applications such as thermoelectric refrigeration for a long time [109, 110].

4.2.1 Crystal structure

In general the atomic arrangement in tetradymite-type M_2X_3 can be visualized in terms of a layered structure, which is characteristic for the 3D TIs [111]. Bi_2Te_3, Bi_2Se_3 and Sb_2Te_3 compounds crystallize in a trigonal crystal structure with the space group $D^5_{3d}(R\bar{3}m)$ [111]. Due to the equivalent structure, in the following the crystal structure of the Bi_2Te_3 compound will be described as an example. The bulk crystal structure of Bi_2Te_3 is shown in Fig. 4.1(a). It has a layered structure built up

by stacked atomic plane sequences of five atoms arranged along the trigonal z-axis of the hexagonal lattice. The strong covalent stacking of two equivalent Bi atoms ($Bi^{[1]}$ and $Bi^{[1']}$), two equivalent Te atoms ($Te^{[1]}$ and $Te^{[1']}$) and an additional third Te atom ($Te^{[2]}$) forms a quintuple layer (QL) sequence of Te-Bi-Te-Bi-Te. Except for the $Te^{[1]}$ atom, whose three nearest-neighbours are located on a different QL layer leaf, the other atoms have six atoms as first neighbours sitting on the layer below and above along the z-axis arranged in an octahedral coordination [110]. The QLs are weakly bound by van-der-Waals forces with a slightly covalent nature [112]. It could be shown, that the relatively large van-der-Waals gaps of the layered structure simplifies the cleaving of single Bi_2Se_3, Bi_2Te_3 and Sb_2Te_3 crystals, in a same way as the mechanical graphene exfoliation, leading to a defined surface termination, see [109,113]. The hexagonal crystal structure shown in Fig.4.1(a) can be constructed by using the three primitive lattice vectors $\boldsymbol{t}_1, \boldsymbol{t}_2$ and $\boldsymbol{t}_3$ spanning the primitive trigonal cell

$$\boldsymbol{t}_1 = (-a_{hex}/2, \sqrt{3}a_{hex}/6, c_{hex}/3) \tag{4.1}$$

$$\boldsymbol{t}_2 = (a_{hex}/2, -\sqrt{3}a_{hex}/6, c_{hex}/3) \tag{4.2}$$

$$\boldsymbol{t}_3 = (0, \sqrt{3}a_{hex}/3, c_{hex}/3), \tag{4.3}$$

where in the hexagonal representation the experimental lattice constants of the Bi_2Te_3 phase are $a_{hex} = 4.384$ Å and $c_{hex} = 30.487$ Å [111], whereas Sb_2Te_3 has the hexagonal cell lattice constants of $a_{hex} = 4.264$ Å and $c_{hex} = 30.458$ Å [114]. The rhombohedral lattice parameters can be found in Ref. [111]. For the purpose of calculating the surface electronic structure, the hexagonal unit cell is used due to the reduced symmetry in the presence of the surface.

4.2.2 Electronic structure

In the 3D TIs Bi_2Se_3, Bi_2Te_3 and Sb_2Te_3 the strong SOC of the constituent elements leads to an inversion of the conduction band and valence band. As a result, there are gapless surface states formed, which reside in the fundamental band energy gap. These dispersing surface states inside the band gap are referred to the relativistic nature of the Dirac Fermions. In contrast to conventional spin-split surfaces, such as Au(111) surface states, the SOC causes highly spin-polarized surface state branches appearing in single cone shaped structures. Due to symmetry considerations, the

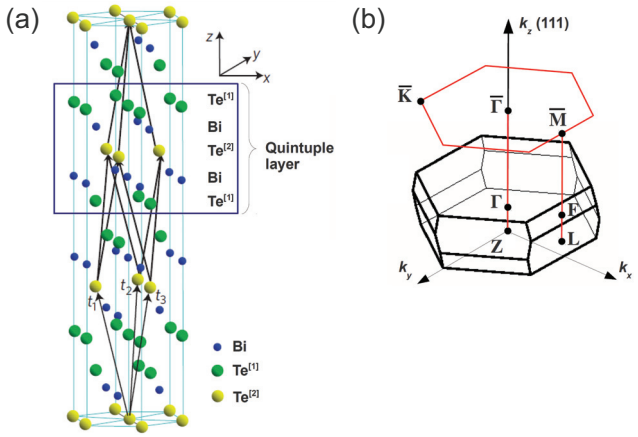

Figure 4.1: *(a) Crystal structure of Bi_2Te_3 with both the primitive rhombohedral, and the hexagonal unit cells indicated. One QL composing a sequence of five atomic layers is indicated by the blue frame. Adapted from [1] (b) Schematic representation of the first bulk BZ with four time-reversal invariant points Γ, Z, F and L. Red hexagon indicates the corresponding 2D SBZ with the $\overline{\Gamma}, \overline{K}$ and $\overline{M}$ points of the (111) surface.*

branches have to cross at an inversion symmetric point, e.g. $\overline{\Gamma}$. In particular, these conducting states are robust against perturbations that preserve the time-reversal symmetry (e.g. surface chemical disorder [2]). Very recently, Henk *et al.* [115] presented the influence of Mn doping on the topological character of Bi_2Te_3 by first-principles calculations. It turned out, that the doping leads to a ferromagnetic order. For an *in-plane* magnetization the Dirac point is shifted perpendicular to the magnetization direction. Contrary, the Dirac surface state is gapped for a magnetization normal to the surface, which breaks the time-reversal symmetry. For electrons the time-reversal symmetry is attributed to an antiunitary operator $\hat{K}$, which reverses $\boldsymbol{p}$ and $\boldsymbol{\sigma}$ of the SO term given in eq. 2.19 as

$$\hat{K}\boldsymbol{p}\hat{K}^{-1} = -\boldsymbol{p} \quad \text{and} \quad \hat{K}\boldsymbol{\sigma}\hat{K}^{-1} = -\boldsymbol{\sigma}. \tag{4.4}$$

Satisfying the property $\hat{K}^2 = -1$, it follows that at time-reversal invariant momenta (TRIM) the eigenstates are twofold spin degenerated. This can be proofed by assuming that a non-degenerated state $|\chi\rangle$ is an eigenstate of $\hat{K}$ with some constant c, which would lead to $\hat{K}|\chi\rangle = c|\chi\rangle$ and thus to $\hat{K}^2|\chi\rangle = |c|^2|\chi\rangle$ [89]. However, due

to $|c|^2 \neq -1$ this is not possible confirming the Kramers theorem. Therefore, the Hamiltonian has to commute with the time-reversal operator as

$$\hat{K}^{-1} H(\boldsymbol{k}) \hat{K} = H(-\boldsymbol{k}). \tag{4.5}$$

This result means, that a smooth perturbation of H, e.g. surface chemical disorder, does not lift the Kramers degeneracy at the TRIM which are basically related to the crossing points of the spin-polarized surface states. Magnetic impurities, such as deposited iron (Fe) layers, can cause an electronic band gap opening of the surface state related to a broken time-reversal symmetry [116].

Due to the close similarity of the electronic properties of graphene based 2D electron systems and the 3D TIs, first the basic differences between those systems will be outlined. Although spin-polarized currents are weak in graphene, which is mainly caused by the 'light' carbon atoms, it is a potential candidate for spintronic applications. It could be shown, that graphene is able to conserve the spin effectively due to the absence of backscattering processes, providing a spin transmission over large distances [117]. The crystal structure is related to an one-atom-thick planar sheets of carbon atoms arranged in a honeycomb lattice. The electronic structure of graphene is described by means of the relativistic Dirac equation. Dirac electrons can be controlled by an application of external electric and magnetic fields or by altering sample geometry and/or its topology [118]. Near the Fermi level the band structure displays the Dirac cone structure consisting of linear energy band dispersions. In particular, there exist six gapless Dirac cones being formed by the conduction (CB) and valence band (VB), respectively. The connection points of the VB and CB boundaries are denoted as Dirac points K and K'. The DOS shape is referred to a semi-metal or rather a gapless semiconducting structure.

Fig. 4.2(a) depicts a schematic drawing of a 3D TI surface state. Unlike in graphene, however, 3D TIs show an odd number of single Dirac cone band dispersions, in most cases at the $\overline{\Gamma}$ point. Similar to the effective Hamiltonian related to 2D QW structures found in Refs. [98, 99], the electronic structure of 3D TIs can be described by an effective tight-binding Hamiltonian model given in Ref. [1]. The origin of the theoretical models used by the TI community can be related to an extended Dirac model presented by Shen *et al.* [119]. Here, the existence of topologically protected boundary states and surface states, being observed in the 2D and 3D TIs, was introduced by means of a modified Dirac equation.

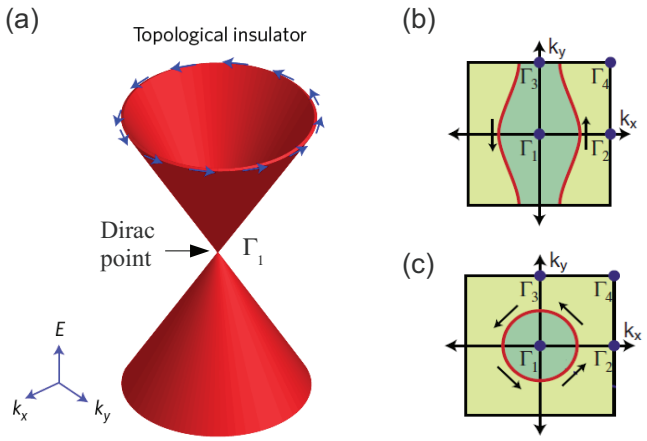

Figure 4.2: *Schematic drawing of a single Dirac cone surface state of a 3D TI. The direction of the spin polarization vector is indicated by the blue arrows. Adapted from [120]. Schematic representation of the Fermi surfaces for (b) a weak TI and (c) a strong 3D TI, respectively.* $\Gamma_{1,2,3,4}$ *denote four time-reversal invariant points within the SBZ. Adapted from [89].*

3D TIs are classified by four $\mathbb{Z}_2$-invariants $\nu_0; (\nu_1\nu_2\nu_3)$ which are used to distinguish between 16 phases, with the two general classes of *weak* and *strong* TIs as proposed by Moore *et al.* in Ref. [121]. The invariants are mathematical quantities based on the 3D generalization of the 2D QSH states reported by Fu *et al.* [105] and are referred to integration areas within the surface Brillouin zone (SBZ), see Figs. 4.2(b) and (c). In this pictures, the Dirac point is projected on the surface Brillouin zone. Depending on the number of surface states present, the invariants are used to define the topological property of the topological space. The geometrical orientation of the resulting closed 2D planes is referred to the three indices $(\nu_1\nu_2\nu_3)$, which are an analogues to the known Miller indices and can form a reciprocal lattice vector given as $\boldsymbol{G} = \nu_1\boldsymbol{b}_1 + \nu_2\boldsymbol{b}_2 + \nu_3\boldsymbol{b}_3$ [100]. If the Fermi surface encloses an even number of projected Dirac points within the SBZ, then the invariant $\nu_0 = 0$ characterizes a *weak* topological insulator (e.g. 2D QSH / TI state) class. A *strong* topological insulator (e.g. 3D TI) is present, when there exists an odd number of Dirac points related to the invariant $\nu_0 = 1$ which is referred to a topologically distinct quantum phase [105, 121, 122], see Fig. 4.2(c).

The essential features of the time-reversal protected surface states are generally described by an effective Hamiltonian expressed by the proportionality

$$H_{ss} \propto v_F(\boldsymbol{k} \times \boldsymbol{\sigma})_z, \tag{4.6}$$

with the Fermi velocity v_F. The spin and momentum are locked within the (x, y)-plane giving rise to Dirac Fermions characterized by an intrinsic spin helicity and a lifted spin degeneracy. The locking is mainly caused by an interplay of the strong SOC and a broken translational symmetry of a truncated surface. The orientation of the electron spin within the Fermi surface is indicated by the blue arrows, demonstrating a defined direction resulting in an opposite spin configuration for opposite momenta, as shown in Fig. 4.2(a). At the TRIM $\Gamma_{a=1-4}$, however, the electronic states remain spin degenerated and cross with opposite spin configurations defined by $\boldsymbol{k}_\uparrow$ and $-\boldsymbol{k}_\downarrow$.

Besides an unusual spin texture within the (x, y)-plane, Bi_2Te_3 shows a notably *out-of-plane* spin polarization which is mainly attributed to an intrinsic deformation of an isotropic Fermi surface as predicted by Fu *et al.* [123]. This feature might be advantageous for spintronic spin injection devices, where an additional *out-of-plane* spin component may reduce the geometric limitation of a fixed *in-plane* spin injection. In particular, there exists an additional cubic $H_w = \frac{\lambda}{2}(k_+^3 + k_-^3)\sigma_z$ term being added to the effective Hamiltonian, which leads to a distortion of the Fermi surface from an isotropic circular to a hexagonal shape described by the dispersion relation [123]

$$\epsilon_\pm(\boldsymbol{k}) = \epsilon_o(\boldsymbol{k}) \pm \sqrt{v^2(\boldsymbol{k})\boldsymbol{k}^2 + \lambda^2\boldsymbol{k}^6 cos^2(3\theta)}, \tag{4.7}$$

where the strength of warping increases for binding energies apart from the Dirac point. In accordance to the coupling to σ_z, the Fermi surface of Bi_2Te_3 shows the strongest distortion among presently examined TIs with a significant *out-of-plane* spin vector component. Indeed, recent extensive spin-polarized ARPES measurements experimentally proofed the unique spin-helical texture of Dirac Fermions from bulk Bi_2Se_3 [3, 124] and Bi_2Te_3 [4, 125] samples, and confirmed the existence of both *in-* and *out-of-plane* spin vector components in Bi_2Te_3 .

Bulk properties

Next, the electronic structure of TIs calculated by means of first-principle DFT methods is presented. The underling process of the SOC induced band inversion can already be obtained from bulk band dispersions.

An exemplary theoretical description of the inversion process was given for the Bi_2Se_3 phase by Zhang *et al.* [1], where the underlying mechanism is summarized in three different stages related to physical properties of the Bi (electronic configuration $6s^26p^3$) and Se ($4s^24p^4$) atomic orbitals, as shown in Fig. 4.3 [1, 85]. In following, only the p orbital states which dominate the top of the valence band and the bottom of the conduction band, will be considered. In the first stage (I), the chemical bonding between Bi and Se atoms leads to five hybridized p orbital states indicated by $|P1^{\pm}_{x,y,z}\rangle$, $|P2^{\pm}_{x,y,z}\rangle$ and $|P0^{-}_{x,y,z}\rangle$, whereby the parity of the orbitals is denoted by the superscripts related to three states (one odd, one even) from each Se p orbital and to two states (one odd, one even) from each Bi p orbital.

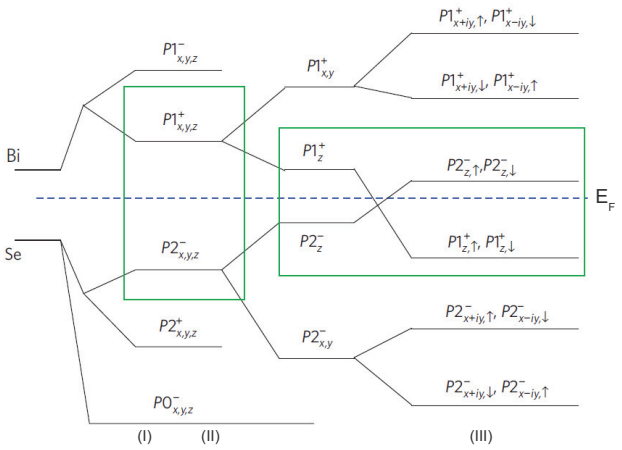

Figure 4.3: *Schematic illustration of the band inversion process near the* Γ *point shown for the* Bi_2Se_3 *material as an example. Steps (I) to (III) depict the change of the atomic orbitals* $p_{x,y,z}$ *caused by chemical bonding, crystal field splitting and finally by strong SOC effects leading to dominating contributions from the* P_z *orbitals near the Fermi level. Taken from [1].*

From the assumptions of this model it follows, that the Bi states are established above the Fermi level, whereas the Se states are pushed down below the Fermi

level. Based on the crystal field theory, the degenerated p states split into x, y and z components as indicated in stage (II). It should be noticed that only p_z levels ($|P1_z^+\rangle$ and $|P2_z^-\rangle$) will contribute significantly to a band inversion near the Fermi level. The SOC effect is described by means of the Hamiltonian $H_{SO} = \lambda \mathbf{L} \cdot \mathbf{S}$ and implies the conservation of the total angular momentum. Herein, H_{SO} combines the spin and angular momenta. This leads to a level repulsion between the $|P1_z^+, \uparrow\rangle$ and $|P1_{x+iy}^+, \downarrow\rangle$ and between similar combinations [85]. Due to the similar electronic configuration this model is also valid for other 3D TIs.

In order to show this mechanism for the Bi_2Te_3 and Sb_2Te_3 compounds, I have applied the linear augmented plane wave (LAPW) method using the WIEN2k [53] package in the scheme of the DFT. The exchange-correlation potential was taken into account by means of the generalized gradient approximation (GGA) of Perdew, Burke, and Ernzerhof [126]. The SOC was considered in a second variational step using scalar-relativistic eigenfunctions as basis.

In Figs. 4.4 and 4.5 the bulk band structures of Bi_2Te_3 and Sb_2Te_3 are plotted along the high-symmetry TRIM Γ, Z, F and L points for the valence band and the near Fermi level region, respectively. Without SOC there exist clear degeneracies of the involved dispersions at certain $\boldsymbol{k}$-values around the TRIM, whereas the band structures are similar to that of a direct bandgap semiconductor. SOC, however, induces a band gap opening reflected by an energy shift for the conduction and valence band. As a result, there appear nondegenerate discrete states. As can be seen for both materials, due to strong SO interaction and crystal symmetry the band character order is inverted near the Γ point. In particular, the former unoccupied bulk conduction state acquires the nature of the occupied valence band and vice versa. The presented results are in a good agreement with previous reported Bi_2Te_3 [1, 127, 128] and Sb_2Te_3 [129] bulk structure calculations.

Surface electronic structure of Bi_2Te_3

The surface electronic properties of the Bi_2Te_3 material were investigated by our collaborators from the theory group PGI-1 (Dr. Bihlmayer, Prof. Dr. Blügel) at the Research Centre Jülich. The topologically protected surface states (TSS) were obtained from a self-consistent full-potential linear augmented plane wave (FLAPW) calculation as implemented in the FLEUR code (for details see [54]). The surfaces were simulated by means of a 6 QL thick slab geometry embedded in vacuum using

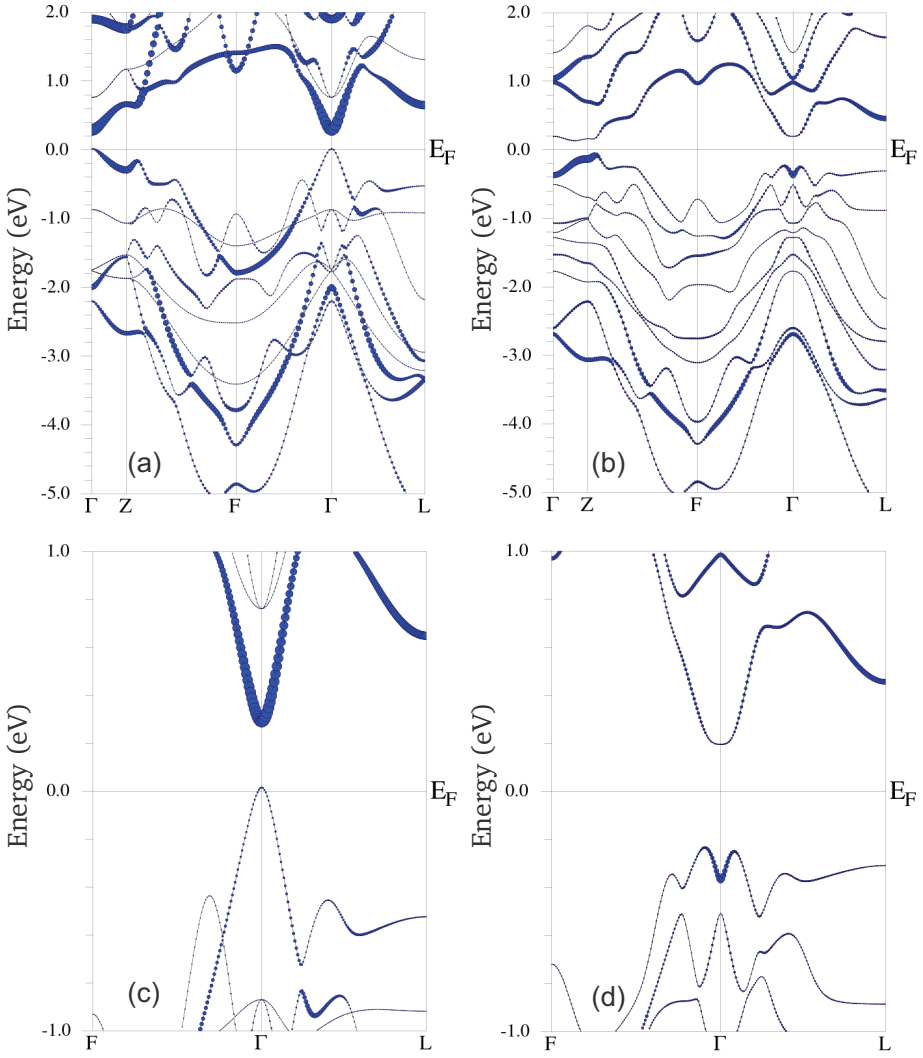

Figure 4.4: *Calculated electronic bulk band structure of Bi_2Te_3 for $|\boldsymbol{k}_\perp| = 0$ $Å^{-1}$. (a,c) Without SOC and (b,d) with SOC included. (a) and (b) show a wide energy window, whereas in (c) and (d) the near Fermi region is plotted along the $F - \Gamma - L$ direction. The size of the blue points reflects the P_z character of the eigenvalues projected onto the atomic basis of the equivalent Bi atoms. The inversion of band character takes place near the Γ point.*

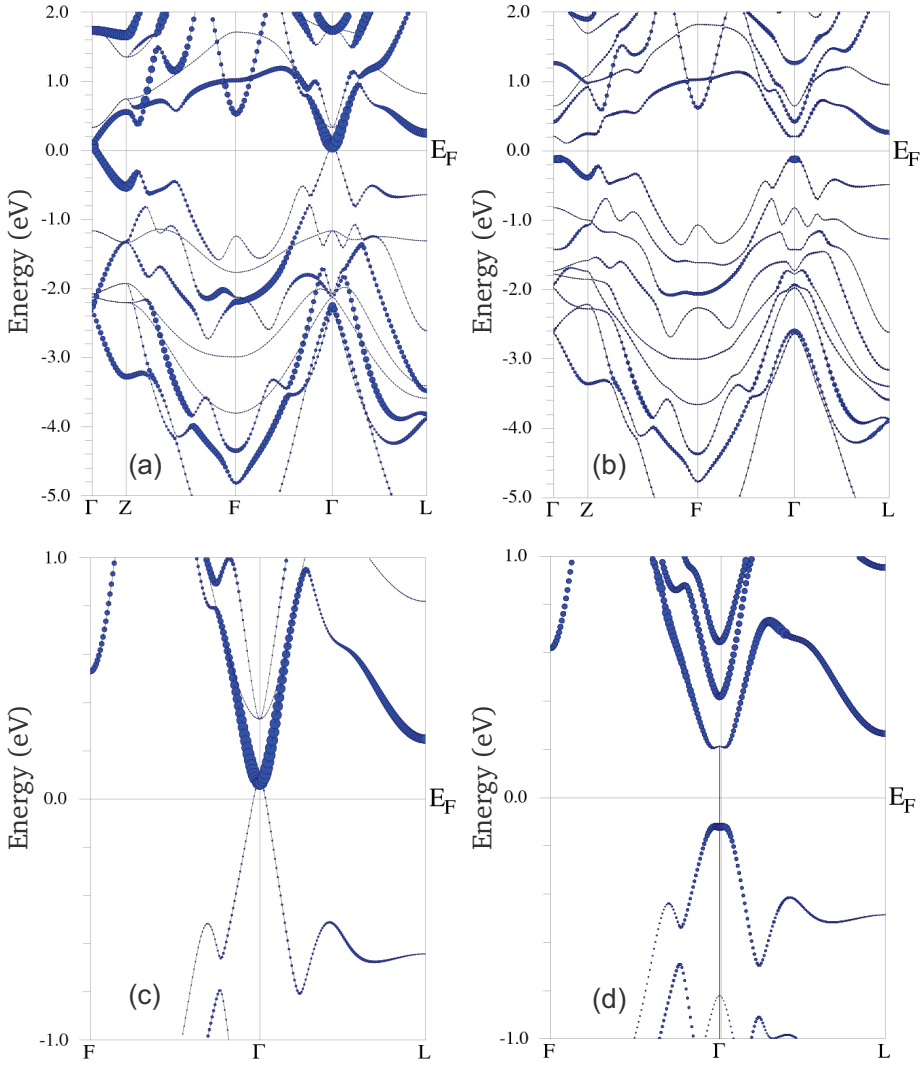

Figure 4.5: *Calculated electronic bulk band structure of* Sb_2Te_3 *for* $|\boldsymbol{k}_\perp| = 0$ $Å^{-1}$. *(a,c) Without SOC and (b,d) with SOC included. (a) and (b) show a wide energy window, whereas in (c) and (d) the near Fermi region is plotted along the* $F-\Gamma-L$ *direction. The size of the blue points reflects the* P_z *character of the eigenvalue projected onto the atomic basis of the equivalent Sb atoms. The inversion of band character takes place near the* Γ *point.*

optimized bulk lattice parameters. The *ab initio* calculations were carried out within the DFT employing the local-density approximation (LDA). SOC was included self-consistently as described in Ref. [130].

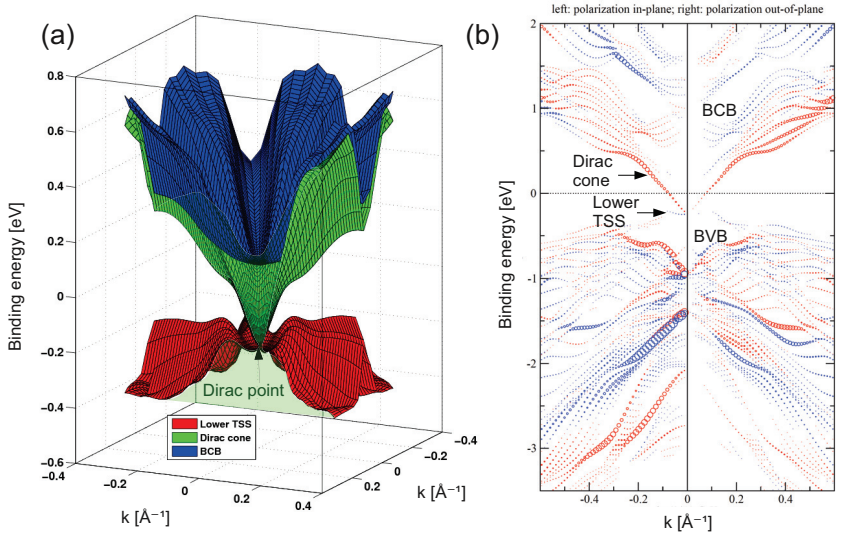

Figure 4.6: *DFT calculation of the surface electronic band structure of a 6 QL Bi_2Te_3 slab. (a) 3D plot of the spin-integrated band structure near the Fermi level along the $\overline{\Gamma K}$ and $\overline{\Gamma M}$ directions. The insight of the nesting BCB within the 3D Dirac cone state is clearly visible by cutting of an angular sector as indicated by the shadowed area. (b) Spin-polarized electronic band structure related to a cut through (a) along one of the planes (for $\overline{\Gamma M}$ direction). Spin-polarized electronic band structure. Blue and red solid circles indicate the spin direction, whereas the size of the symbols is related to the magnitude of the spin polarization of the BCB, Dirac cone and BVB states. For simplicity in-plane (left) and out-of-plane (right) spin vector components share the same plot. Calculated by our collaborators from the neighbouring institute PGI-1, Dr. Bihlmayer and Prof. Dr. Blügel.*

Fig. 4.6(a) shows the Dirac cone state calculated by the FLEUR code in the 6 QL slab geometry with the bottom of the condution band. This is characterized by a bulk conduction band (BCB, blue), the Dirac cone surface state (green) and the related lower part of the Dirac cone (red) denoted 'lower TSS'. The 3D plot was obtained from single band dispersion calculations between the $\overline{\Gamma M}$ and $\overline{\Gamma K}$ directions (here, in every 5 deg steps) which were finally combined with the symmetric parts of the SBZ. Furthermore, a spin-polarized band structure was calculated, which is

shown in Fig. 4.6(b) for the $\overline{\Gamma M}$ direction. On the left side of the plot the size of the marker reflects the magnitude of the *in-plane* spin polarization, whereas on the right side the *out-of-plane* spin polarization magnitudes are shown. As can be seen, the band structure is characterized by a set of spin-polarized surface localized energy bands extending up to 3.5 eV binding energy, which indicate the unique spin properties of that material. Herein, the red and blue open circles are related to the different orientations of the spin vector, whereas the size of the symbols represents the magnitude of the spin polarization. The only feature arising between the bulk conduction band and the bulk valence band (BVB) is the time-reversal protected Dirac cone surface state, which is formed intrinsically due to the opened SO band gap as described in the theory of surface states by Pendry and Gurmann [39]. In Fig. 4.6(b) the corresponding 3D illustration of the calculated BVB, Dirac cone and BCB states near the Fermi level is depicted. Especially these highly spin-polarized states find particular attention within the framework of this thesis, which are studied by dedicated spin- and angle-resolved PES measurements.

However, in order to interpret real spin-resolved photoemission results, an extended model will be needed which considers the experimental conditions such as the electron mean free path dependence leading to depth-resolved spin information of the states localized within the first surface atomic layers. The experimental results are presented in paragraph 4.3.

4.3 Experimental results and discussion

4.3.1 Sample preparation

Since photoemission spectroscopy is a surface-sensitive method, it requires clean and well-ordered surfaces. In this framework, clean surfaces of 3D TI thin film and single crystalline samples have been successfully prepared by using a variety of surface preparation techniques.

The Bi_2Te_3 and Sb_2Te_3 thin films were grown on chemically cleaned *n*-doped Si(111) 100 mm diameter wafers using a solid-source molecular-beam epitaxy (MBE) system consisting of Knudsen effusion cells under UHV conditions. A detailed description of the epitaxial thin film growth procedure, the characterization and film quality optimizations can be found in Ref. [131]. After the growth, the prepared

Bi_2Te_3 and Sb_2Te_3 films were exposed to air and cut into pieces of approximately 10×10 mm^2. Finally, the samples were mounted onto plates compatible with the Omicron sample holder system and prepared *in situ* by different types of surface cleaning methods. We succeeded to clean Sb_2Te_3 thin film surfaces via a single annealing step as well as by cleaving using a silver epoxy. The latter method is also planned for Bi_2Te_3 and Bi_2Se_3 thin films. Our investigations showed, that in the case of Bi_2Te_3 thin films several annealing and sputtering cycles were necessary in order to clean the sample surface. Moreover, it was possible to cleave single crystals of Bi_2Se_3 in UHV with a scotch tape.

For the Bi_2Te_3 thin films, with a thickness of $\sim$ 16 nm, repeated sputter and annealing cycles were required to achieve a clean and well-ordered surfaces. During the sputtering with Ar-ions at 500 eV, the sample was held at room temperature and positioned at an angle of 45° with respect to the sputter device. The working pressure was kept at about $p \sim 6.5 \cdot 10^{-6}$ mbar. After each sputter cycle the sample was flashed to roughly 220 °C for 5 min. The temperature of the sample during annealing was controlled by a calibrated infrared pyrometer through a standard UHV viewport. The amount of C and O contaminants was checked by means of AES measurements at primary electron energy $E_{AES} = 3$ keV. As shown in Fig. 4.7(a), the Carbon and Oxide peaks were reduced after two sputter and annealing cycles. The determined kinetic energies of the Bi_2Te_3 Auger peaks are summarized in Table 4.1. An additional decrease of the Bi_2Te_3 thin film thickness led to the Silicon (Si) peak of the substrate showing up in AES, which appeared after eight cleaning cycles, see Fig. 4.7(b). The presence of the Si peak in the AES spectra allowed the determination of a sputtering rate of $\sim$2.5 nm/min [132].

Atomic number Z	Element	Transition	Kinetic energy [eV]
6	C	KLL	270
8	O	KLL	510
14	Si	LMM	93
52	Te	MNN	484, 489
83	Bi	MNN	102, 250, 269

Table 4.1: *Bi_2Te_3 AES peak information. The measured kinetic energies for different elements with an atomic number Z and the related spectral lines are given.*

Fig. 4.7(c) shows the resulting hexagonal LEED pattern of a cleaned and well-ordered Bi_2Te_3 thin film surface taken at a primary electron energy $E_{LEED} = 80$ eV.

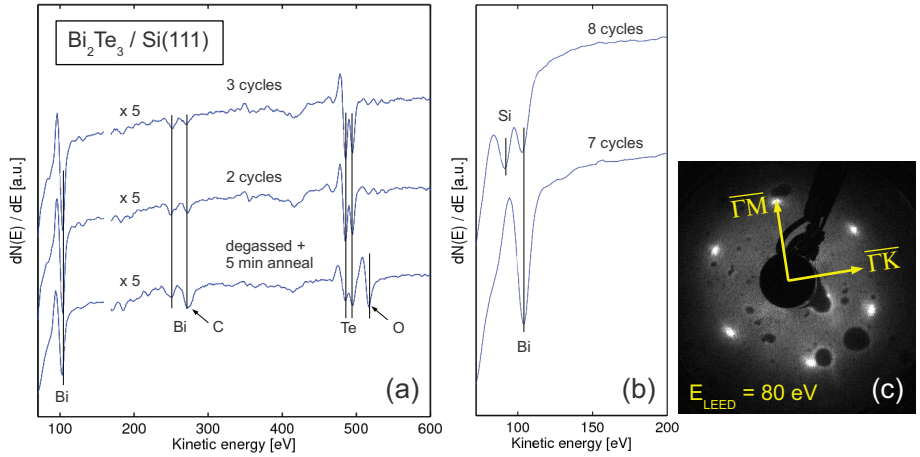

Figure 4.7: *(a) Auger electron spectra of a Bi_2Te_3/Si(111) thin film shown for the different cleaning cycles. (b) The evolution of the substrate Si peak after additional cleaning cycles. (c) The observed LEED pattern was measured at a primary electron energy $E_{LEED} = 80$ eV. Clear diffraction spots are visible related to the hexagonal structure of the Bi_2Te_3 unit cell.*

The observed spots confirm a fully epitaxial thin film growth and demonstrate, that the prepared surfaces are adequate for further angular-resolved band structure measurements. In addition, the image provides the necessary informations of the crystal orientation (see yellow arrows), which is required for the alignment of the sample surface for ARPES measurements. Surfaces of the layered crystals are typically passive, and the apparent quality of the LEED pattern remained unchanged even after several days, which confirms the long term stability of the prepared surfaces. The LEED spot size was relatively broad, which can be referred to a cleaning-induced surface roughness as confirmed by atomic force microscopy (AFM) measurements. The AFM results for a Bi_2Te_3 sample, which has been sputtered and annealed three times, are shown in Fig. 4.8. Here, a remarkable increase of the surface roughness originating from the cleaning cycles with a root mean square value of ~ 1 nm was identified [131]. Before the cleaning the surface roughness value was about ~ 0.5 nm [133]. Nevertheless, the surface states being investigated by means of ARPES measurements remained robust even after more additional sputter and annealing procedures as will be shown later.

In the case of the Sb_2Te_3 material no sputtering of the sample surface was applied. The sample was annealed for 5 min around 250 °C resulting in a clean and well-ordered surface. The Auger data and resulting LEED pattern are shown in Fig. 4.9. The determined kinetic energies of the Sb_2Te_3 Auger peaks are summarized in Table 4.2. Since Bi_2Te_3 and Sb_2Te_3 share the same crystal structure, the LEED patterns have the same structure. The orientation of the crystal is indicated by the yellow arrows. Since no sputtering was involved, the film surface roughness was assumed to remain unchanged. Fig. 4.9(c) shows a typical scanning tunneling microscope (STM) image taken after the cleaning procedure around ~ 4.2 K which demonstrates a clear hexagonal periodic pattern with an atomic resolution.

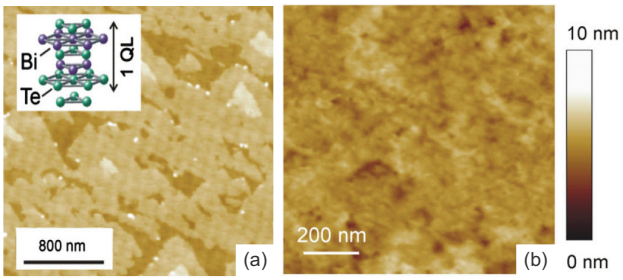

Figure 4.8: *AFM images of a Bi_2Te_3 thin film taken before (a) and (b) after an extended UHV surface preparation procedure. The height of the QL steps is about 1 nm. Adapted from [131]. The inset in (a) shows the crystal structure of Bi_2Te_3 with a thickness of 1 QL.*

Atomic number Z	Element	Transition	Kinetic energy [eV]
6	C	KLL	271
8	O	KLL	511
51	Sb	MNN	455, 463
52	Te	MNN	484, 489

Table 4.2: *Sb_2Te_3 AES peak information. The measured kinetic energies for different elements with an atomic number Z and the related spectral lines are given.*

Moreover, clean and well-ordered Sb_2Te_3 sample surfaces were obtained by cleavage under UHV conditions. To cleave clean surfaces, a small post was glued to the Sb_2Te_3 sample surfaces *ex situ* by using a conducting silver epoxy cement. The resulting droplets covered a sample area of approximately 2×3 mm^2. Fig. 4.10 shows

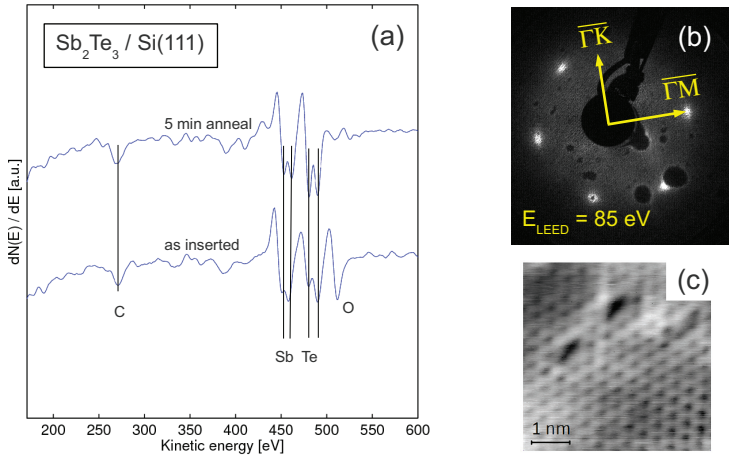

Figure 4.9: *(a) Auger electron spectra of a Sb_2Te_3/Si(111) thin film shown for the sample before and after annealing at 250 °C for 5 min. (b) The observed LEED pattern was measured at primary electron energy $E_{LEED} = 85$ eV. Clear bright diffraction spots are visible related to the hexagonal structure of the Sb_2Te_3 unit cell. (c) STM image measured on cleaned Sb_2Te_3 sample kept at 4.2 K.*

the photographs of typical Sb_2Te_3 sample mountings before the cleavage procedure. In vacuum, the post together with the glue were knocked off using a standard wobble stick. This removal caused the exfoliation of the first few QLs resulting in clean and well-ordered spot of sample surface. However, a cleavage of the Bi_2Te_3 surface was not possible. This may be associated with the stronger covalent interlayer bonding of the Bi_2Te_3 material.

4.3.2 ARPES on Bi_2Te_3 and Sb_2Te_3 thin films

Bi_2Te_3 and Sb_2Te_3 surfaces prepared by the aforementioned sample recipes were first investigated in the PGI-6 (Research Centre Jülich) by means of high-resolution ARPES measurements. The technical details of the laboratory based system are described in chapter 3. These measurements provided a thorough characterization of the band dispersions and the related surface states. Next, the data acquired with the laboratory system is presented.

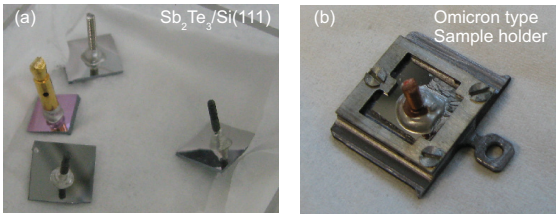

Figure 4.10: *Photographs of (a) glued posts to various Sb_2Te_3 sample surfaces and (b) a typical mounting of the sample on the Omicron type sample holder in which the sample is fixed by a Molybdenum frame body.*

High-resolution ARPES on Bi_2Te_3/Si(111) epilayers

Fig. 4.11 shows the ARPES intensity maps of the photoelectrons taken in normal emission geometry along the $\overline{\Gamma K}$ direction as a function of the momentum $\boldsymbol{k}$ and the binding energy E_B. The 2D $E_B(\boldsymbol{k})$ map covering a wide binding energy region is depicted in panel (a), whereas states appearing near the Fermi level are plotted separately in panel (b). The color scale saturation was separately adjusted for the different binding energy windows.

The clean Bi_2Te_3 thin film surface shows clear and well-defined surface states. Between 1.0 and 3.5 eV binding energy E_B the spectral weight distribution of the electronic structure is mainly dominated by a set of strongly dispersive energy bands near the $\overline{\Gamma}$ point indicated by letters β - ϵ. In the vicinity of the Fermi level the 'V-like' surface state α is related to the topologically protected Dirac cone, which is shown in more detail in Fig. 4.11(b). All present branches of dispersive bands are symmetric with respect to $|\boldsymbol{k}_{\|}| = 0$ Å^{-1}. The existence and sharpness of the observed dispersions confirms the quality of the MBE-grown thin films and compares well to the data from cleaved single crystals reported in Refs. [106, 134] or films studied *in situ* [135].

Within the narrow binding energy window the α surface state is accompanied by a bulk conduction band (BCB) and a bulk valence band (BVB) contributions. Following Ref. [136], the BCB near E_F is mainly caused by electron-type bulk carriers induced by Te-vacancies. In order to obtain the Fermi velocity, it is possible to use the linear shape of the energy dispersion near the $\overline{\Gamma}$ point assuming $E(k) \approx E_F \pm \hbar v_F k$, where v_F is the Fermi velocity of the charge carriers. Thus, v_F was obtained by fitting the linear dispersion yielding 2.82 eV Å ($v_F = 4.28 \times 10^5$ m/s), a value which is

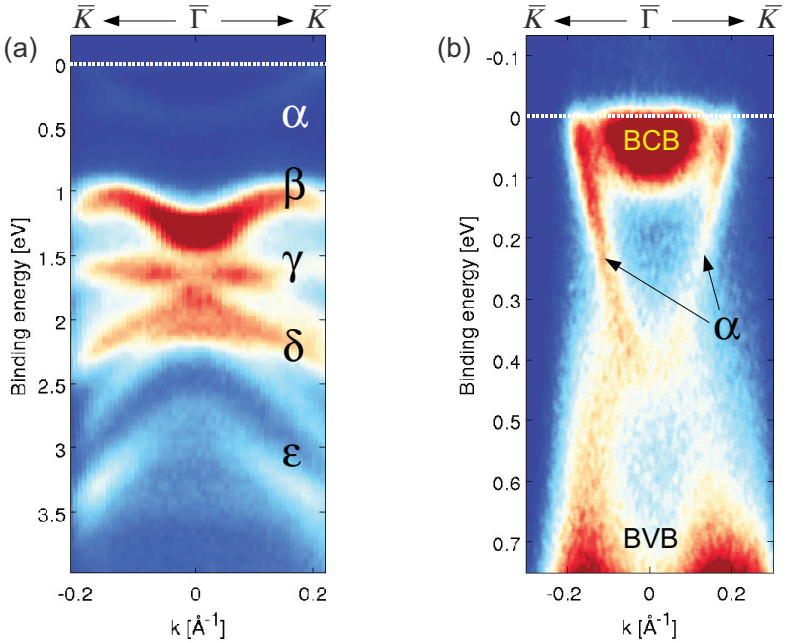

Figure 4.11: *Selected ARPES maps of surface electronic band dispersions of a Bi_2Te_3 thin film near the $\bar{\Gamma}$-point measured along the $\bar{\Gamma}\bar{K}$ direction using He I radiation ($h\nu = 21.218$ eV). (a) Measured wide range 2D angular map over the full valence band region. α - δ indicate the observed band dispersion areas. (b) The 'V'-shaped surface state α near the Fermi level forms a Dirac cone which is accompanied by a BCB and a BVB. The white dashed line indicates the Fermi level position.*

close to the one reported by Chen *et al.* [106] (2.67 eV Å, $v_F = 4.05 \times 10^5$ m/s) along the $\bar{\Gamma}\bar{K}$ direction. It should be emphasized here, that the observed Dirac cone structure does not show a distinct Dirac point at the $\bar{\Gamma}$ point. Compared to the cleaved single crystals [106], however, the present cones are wider, which is comparable to the states measured on air-exposed surfaces [137], where a strong modification of the surface state α was explained by a sample exposure to air or N_2 which gives rise to an alteration of the surface state.

In order to provide an entire picture of the (k_x, k_y)-space, the Fermi surface of Bi_2Te_3 has been measured by scanning the polar angle of the sample in the direction orthogonal to the spectrometer slit. For this purpose, various cuts in the momentum space were measured at different polar emission angles and merged together

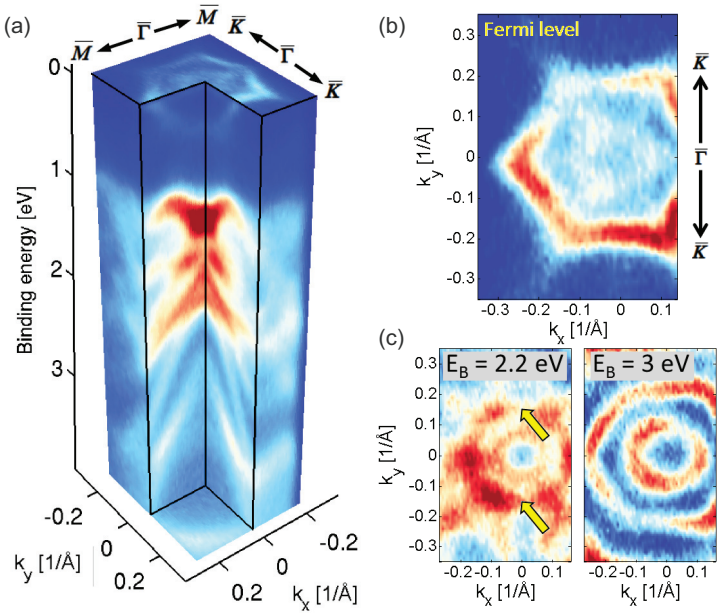

Figure 4.12: *(a) Experimental 3D illustration of the band structure of the Bi_2Te_3 thin film over the full valence band region. (b) Constant energy surfaces for the Fermi level (top), $E_B = 2.2$ eV and $E_B = 3.0$ eV. Each map was separately normalized for optimized contrast. Arrows in the $E_B = 2.2$ eV map indicate the two example symmetric positions on the ring, related to the δ surface band, for which the direction of the polarization vector is reversed due to its helical nature.*

yielding a 3D band structure which is shown in Fig. 4.12(a). The spectral weight distribution along both $\overline{\Gamma K}$ and $\overline{\Gamma M}$ directions is given. The $\boldsymbol{k}$-space mapping allows an accurate sample alignment to the different wave vector locations. At the Fermi level $E_F = 0$ eV the Bi_2Te_3 Dirac cone surface state forms a highly warped hexagram Fermi surface. Fig. 4.12(b) shows a more detailed picture of the measured (k_x, k_y)-map. In contrast to the proposed warping model [123], the observed hexagon deformation is related to non-linear parts of the Dirac cone along the $\overline{\Gamma M}$ direction near the Fermi level which lead to the warped rims within the Fermi surface. Near the Dirac point position the warping effects can be described by the aforementioned theoretical model. The BCB contribution located inside the Dirac cone surface state α displays a trigonal symmetry. A clear trigonal symmetry is also present at higher binding energies, see the constant energy map taken at $E_B = 3$ eV,

as shown in Fig. 4.12(c). The presence of the threefold symmetry indicates a thin film growth satisfying a single domain structure. Thus, we can exclude the presence of 60° rotated crystalline domains which were reported in Ref. [138]. The constant energy surface at $E_B = 2.2$ eV is related to the surface state δ. Later it will be demonstrated, that the α, δ and ϵ states carry highly spin-polarized electrons.

In order to confirm the proposed insensitivity of the thin film sample surface to disorder and interaction effects, the impact of a reduced film thickness was investigated next. For this purpose, the sample surface was treated by additional sputtering and annealing cycles. The film thickness was decreased from 16 QL down to an ultra thin film of approximately 1 QL using a sputtering rate of $\sim$ 2.5 nm/min. After sputtering, the sample was subsequently annealed at 250 °C for 5 min. Fig. 4.13 depicts the thickness dependent evolution of the Dirac cone surface state by means of angular maps measured along the $\overline{\Gamma K}$ direction. In this particular case shown in Fig. 4.13 the sample was held at $\sim$ 140 K during the sputtering, however identical results were obtained when sputtering at room temperature. The accuracy of the given thickness values is $\pm$0.5 QL ($\sim$ 0.5 nm) to account for small instabilities of the sputter gun ion flux and the non-uniform thickness profile shown in Fig. 4.8.

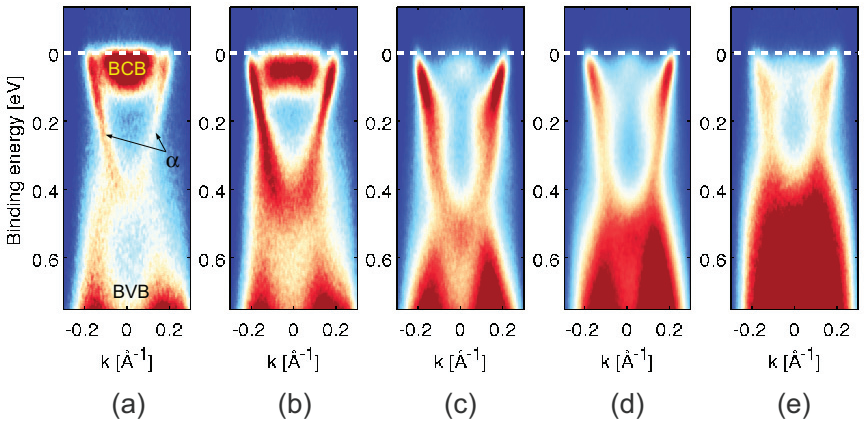

Figure 4.13: *(a)-(e) Selected ARPES maps measured along the $\overline{\Gamma K}$ using He I radiation ($h\nu = 21.218$ eV) at 140 K in the course of cleaning the same Bi_2Te_3 film several times. (a) 16 QL ($\approx$ 16 nm) (b) 11 QL (c) 6 QL (d) 3.5 QL (e) 1 QL. The white dashed line indicates the Fermi level position.*

As can be seen, the induced surface thickness perturbation leads to remarkable effects on the electronic band structure. For example, the spectral weight of the conduction band clearly decreases with the reduction of the film thickness. In the case of an ultra-thin film (1 QL) the BCB contribution is negligible, see panel (e). An opposite behaviour was observed for the spectral weight of the BVB, which clearly increased with a decreasing thin film thickness in comparison to the Dirac cone surface state α. The $E_B(\boldsymbol{k})$ maps obtained from thicker films, i.e. 16-11 QL, are comparable to the ones of Li *et al.* [135] measured on 2-5 QL films. However, in their work the spectral weight of the conduction band minimum decreased with an increasing film thickness and may be related to the time dependence of the film's growth. The data presented in this thesis shows an opposite trend reflecting a stoichiometry change of the surface caused by the sputter process [132]. The relative position of the surface state α with respect to the Fermi level (white dashed line), remains constant down to ultrathin films with a thickness of ~ 1 QL, see Fig. 4.13(e). The presence of the clear Dirac cone state after sputter induced surface disorder and roughness reflects the topological nature of the Bi_2Te_3 thin film structure and thus confirms the theoretical prediction of a robust Dirac cone surface state.

High-resolution ARPES on Sb_2Te_3/Si(111) epilayers

Fig. 4.14 shows high-resolution ARPES measurements of an annealed Sb_2Te_3 thin film taken in normal emission geometry. The wide binding energy angular map in panel (a) depicts clear dispersive energy band regions indicated by α-ϵ. The band structure is very similar to that obtained from the Bi_2Te_3 thin films, however, the observed α surface state near the Fermi level is related to the lower Dirac cone. Panel (b) shows the sharp Dirac cone surface state around the $\overline{\Gamma}$-point in more detail. Due to the intrinsic p-doped nature of bulk Sb_2Te_3, the Dirac point position is located above the Fermi level and thus is unobservable directly by a standard ARPES experiment [139]. The high-intensity spectral weight (red) originates from the BCB contribution. The related measured Fermi surface is displayed in Fig. 4.14(c).

4.3.3 SP-ARPES on Bi_2Te_3 and Sb_2Te_3 thin films

At the beamline 5, the spin-polarized PES experiments were performed on clean Bi_2Te_3 and Sb_2Te_3 thin films. The details of the sample preparation procedure are

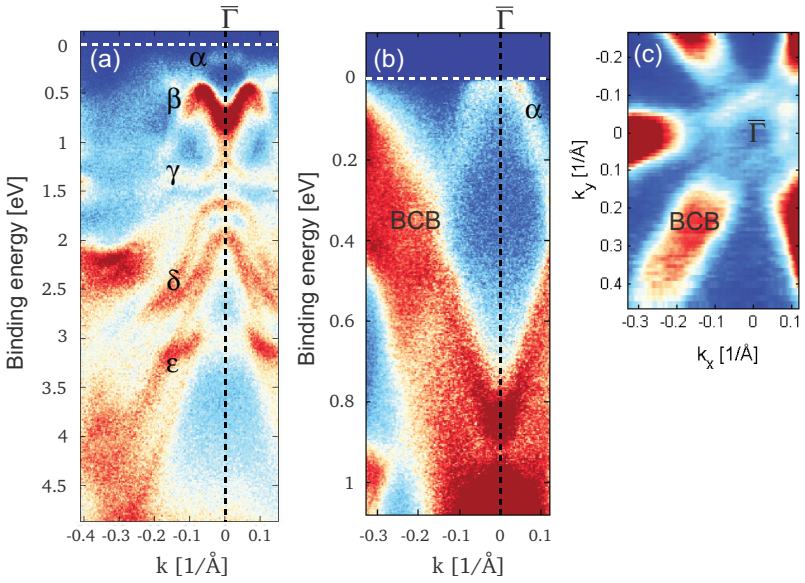

Figure 4.14: *Selected experimental ARPES maps from Sb_2Te_3 thin film measured at ~ 15 K. (a) Wide energy window spectrum taken with He I radiation ($h\nu = 21.22$ eV). (b) Narrow binding energy map near the Fermi level taken with Xe ($h\nu = 8.44$ eV) excitation. The white dashed lines represent the Fermi level position. (c) (k_x, k_y)-plot near the $\overline{\Gamma}$ point showing the Fermi surface of the Sb_2Te_3 thin film. The high-intensity spectral weight originates from the BCB contribution.*

described in paragraph 4.3.1. The following SP-ARPES results were all carried out using a photon energy of $h\nu = 24$ eV which is relatively close to the photon energy $h\nu = 21.2$ eV of the He I radiation used for the laboratory measurements. For all presented SP-ARPES measurements a pass energy of $E_{pass} = 20$ eV was used, whereas the sample was kept around 200 K.

SP-ARPES on Bi_2Te_3

The spin-polarized measurements were carried out at two different $\boldsymbol{k}$-space positions located within the hexagonal Fermi surface as shown in Fig. 4.15(a). In order to capture the helical nature of the Dirac Fermions, the Bi_2Te_3 sample was tilted to the two opposite warped parts of the Fermi surface boundaries indicated by letters A and B. The corresponding angular maps were taken along the $\overline{\Gamma M}$ direction and are

depicted in panel (b). At normal emission (NE), the 'V'-shaped Dirac cone surface state is accompanied by additional spectral weights originating from the BCB and BVB contributions, which is in a very good agreement with the presented laboratory data. For the positions A and B the tilt angle of the sample was manually optimized to the 'W'-shaped band dispersions. At these positions the spin-polarized signals were integrated over the SPLEED detection area of 0.03×0.1 $Å^{-2}$ with the centres located at $k_{\|} = \pm 0.18$ $Å^{-1}$ for position A or B, respectively.

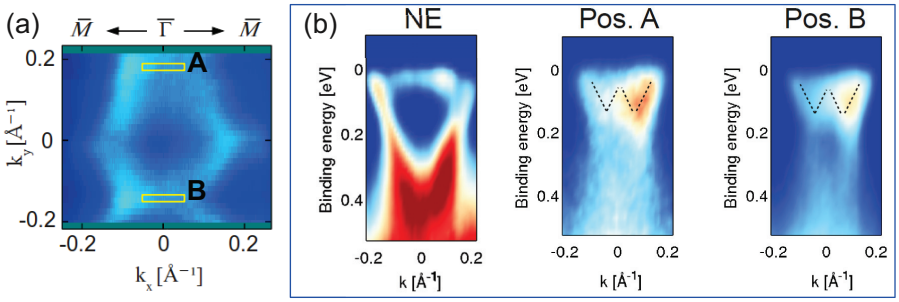

Figure 4.15: *(a) Experimental Fermi surface of the Bi_2Te_3/Si(111) thin film indicating the $\boldsymbol{k}$-space areas A and B, which are integrated in the spin-polarized experiment. (b) Angular maps taken along the $\overline{\Gamma M}$ direction for three different sample tilt angles related to the normal emission (NE) and the outer Dirac cone $\boldsymbol{k}$-space positions at approximately $|\boldsymbol{k}_{\|}| =$ 0.18 $Å^{-1}$. The measurements were taken at a photon energy $h\nu = 24$ eV.*

There are several effects which may influence the spin polarization value extracted from the experimental data. One of them is related to the instrumental asymmetry of the spin polarimeter, see chapter 3. In typical spin-polarized photoemission experiments on ferromagnetic thin films this issue is addressed by re-magnetizing the film in the opposite directions to effectively cancel instrument related asymmetries. Since in a non-ferromagnetic material such as Bi_2Te_3 magnetization is not possible, the spectra have been measured on the two precisely opposite sides of the warped Fermi surface Dirac cone rim. The calibration is confirmed by comparing the spectra measured on positions A and B.

Figs. 4.16 and 4.17 show the spin-resolved results from the Bi_2Te_3 thin film for the narrow and for the extended binding energy regions, respectively. In each figure, panels (a) and (b) display the *in-plane* P_x and *out-of-plane* P_z spin vector components for the position A, respectively. For the position B, the particular components

P_x and P_z are plotted in panels (c) and (d), respectively. For each position the data acquisition time was in the order of 5 hours for the near Fermi level window, whereas a sufficient statistic was obtained within one hour for the wider binding energy region. The signals for the beams scattered from the SPLEED W(001) crystal in opposite mirror directions are indicated by $I^{\uparrow}$ and $I^{\downarrow}$ which represent the intensities for the different spin vector orientations. In all spin-resolved plots, blue and red symbols are referred to different spin orientations, either spin-up or spin-down electrons per definition. The related solid curves represent slightly smoothed data of the measured channeltron intensities. In analogy to the analysis shown in Ref. [124], the unpolarized constant background above the Fermi level E_F has been removed by using a fitting procedure. For the two opposite momenta the spin polarization values were calculated according to $P_{x,z} = \frac{1}{S}(I^{\uparrow}_{x,z} - I^{\downarrow}_{x,z})/(I^{\uparrow}_{x,z} + I^{\downarrow}_{x,z})$. A Sherman function $S = 0.25$ has been chosen for the calculation of the particular spin polarization values, which are plotted by means of black symbols and a smoothed black solid curves below the corresponding spin-resolved EDCs. The error bars were obtained from standard deviation analysis and give the accuracy of the measured spin polarization values which depends on the countrate statistics.

Near the Fermi level E_F, the sharp intensity peaks around $E_B = 0.08$ eV are related to the upper branch of the Dirac cone surface state α. For this state, a clear sign reversal of the *in-plane* P_x component has been obtained comparing the data at positions A and B. The positive P_x values at position A become negative on the opposite side of the cone at position B. For the *out-of-plane* signal the situation is similar, however, the P_z vector component changes its sign from negative to positive values. This direct comparison of both measurements confirms the theoretically proposed helical nature of the spin polarization vector $\boldsymbol{P}$. For the *in-plane* spectra polarization values of up to $P_x \sim 45\%$ were obtained, in contrast to the much smaller *out-of-plane* polarization of about $P_z \sim 15\%$. The presence of an *out-of-plane* component is in a agreement with the theoretical prediction by Fu *et al.* [123], and is mainly caused by coupling effects within the Hamiltonian at the highly warped parts of the Bi_2Te_3 Fermi surface. The mean standard deviation of the given spin-polarizations is in the order of $\pm 5\%$. The polarization behaviour of the surface state α is also confirmed within the wider binding energy plots depicted in Fig. 4.17. Here, the spin polarization of the states observed for higher binding energies appearing below the Dirac cone are given. The measured intensity peaks are

indicated by the letters α-ϵ in reference to the angular map shown in Fig. 4.11(a). The strongest signal was observed for the δ-state. Less intensity was observed for the deeper lying states located at higher binding energies as well as for the surface state α appearing at $E_B < 1$ eV binding energy. The most pronounced state δ is located around $E_B = 2.3$ eV and shows the highest *in-plane* spin polarization of up to $P_x \sim 55\%$ among other observed valence band states. Again the polarization magnitudes change their sign between the positions A and B. Spin reversals were also measured for the β, γ and ϵ states localized within the surface QL. These results indicate, that the observed spin-polarized states obey the helical property of the electron spin. In addition, there are also indications of a sizeable *out-of-plane* polarization in other states, especially for the γ-state, which has the opposite polarity to the Dirac cone. However, in the current data this is close to the noise limit. The sufficient statistics is confirmed by the vertical error bars with a mean standard deviation value of $\pm 2\%$. Moreover, the spin-integrated spectra obtained from the laboratory based measurements at position A is shown. Excluding light polarization effects and the small photon energy difference, which result in different peak intensities, the integration of the laboratory based data over the SPLEED slit geometry around $|\boldsymbol{k}_\parallel| = 0.18$ Å^{-1} agrees well with the peak positions and peak widths of the synchrotron experiment. Table 4.3 gives an overview of the experimental observed spin polarization values of the entire electronic valence band structure.

Bi_2Te_3/Si(111)		Pos. A		Pos. B	
Dispersion	E_B [eV]	$P_x \pm \sigma_{P_x}$	$P_z \pm \sigma_{P_z}$	$P_x \pm \sigma_{P_x}$	$P_z \pm \sigma_{P_z}$
α	0.08	0.42 ± 0.05	-0.12 ± 0.05	-0.45 ± 0.05	0.08 ± 0.05
β	0.90	0.31 ± 0.03	-0.09 ± 0.03	-0.22 ± 0.04	0.03 ± 0.04
γ	1.70	-0.13 ± 0.02	0.03 ± 0.02	0.15 ± 0.03	-0.14 ± 0.03
δ	2.30	-0.54 ± 0.01	0.02 ± 0.02	0.58 ± 0.02	-0.07 ± 0.02
ϵ	3.35	0.44 ± 0.02	-0.01 ± 0.02	-0.25 ± 0.03	-0.08 ± 0.03

Table 4.3: *Experimental spin polarization values for the Bi_2Te_3 energy band dispersions $\alpha, \beta, \gamma, \delta$ and ϵ investigated at the $\boldsymbol{k}$-positions A and B for chosen binding energy positions. The standard deviations σ_{P_x} and σ_{P_z} of the in-plane and out-of-plane spin polarization components are given.*

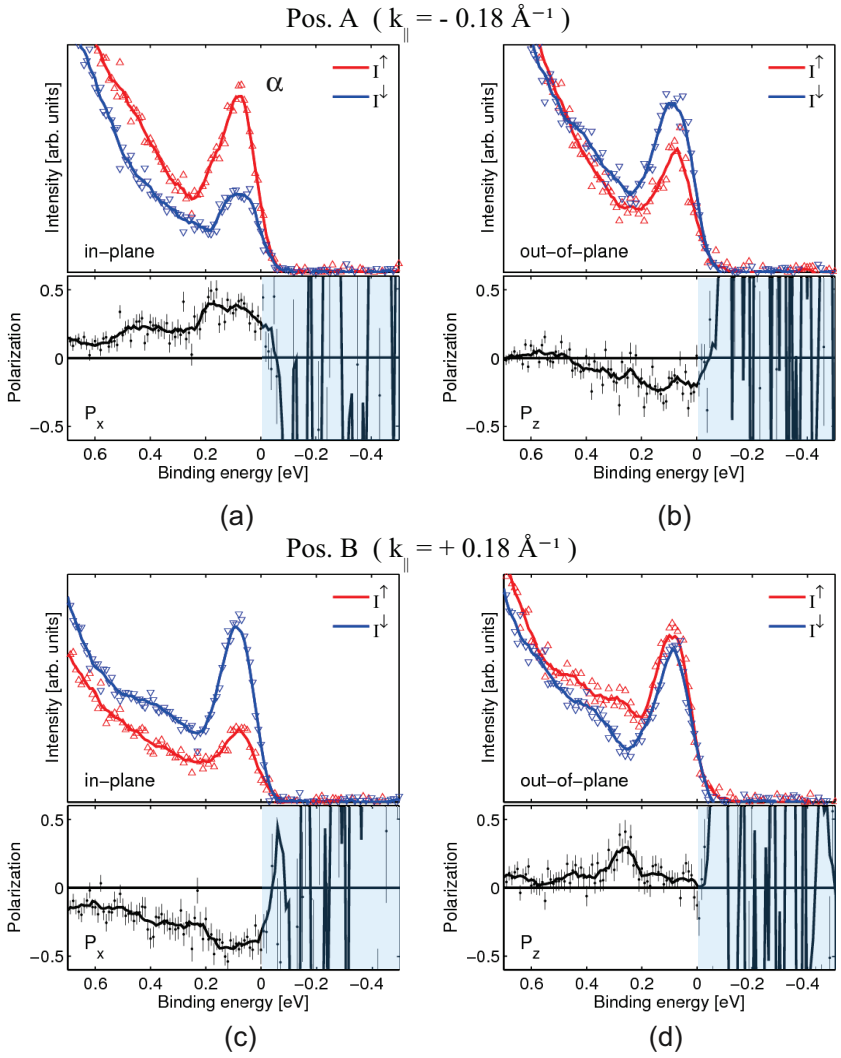

Figure 4.16: *Spin-polarized spectra of the Bi_2Te_3 Dirac cone state α taken along the $\overline{\Gamma K}$ direction at $h\nu = 24$ eV at selected positions $|\boldsymbol{k}_{\parallel}| = 0.18$ Å. Red and blue solid lines are related to smoothed $I^{\uparrow}$ and $I^{\downarrow}$ intensities for (a,c) the in-plane and (b,d) the out-of-plane spin vector components at different $\boldsymbol{k}$-space positions A and B, respectively. The related spin polarizations P_x and P_z are shown below the corresponding intensity plots, whereas standard deviations are given by vertical error bars. The black curves are guides to the eye.*

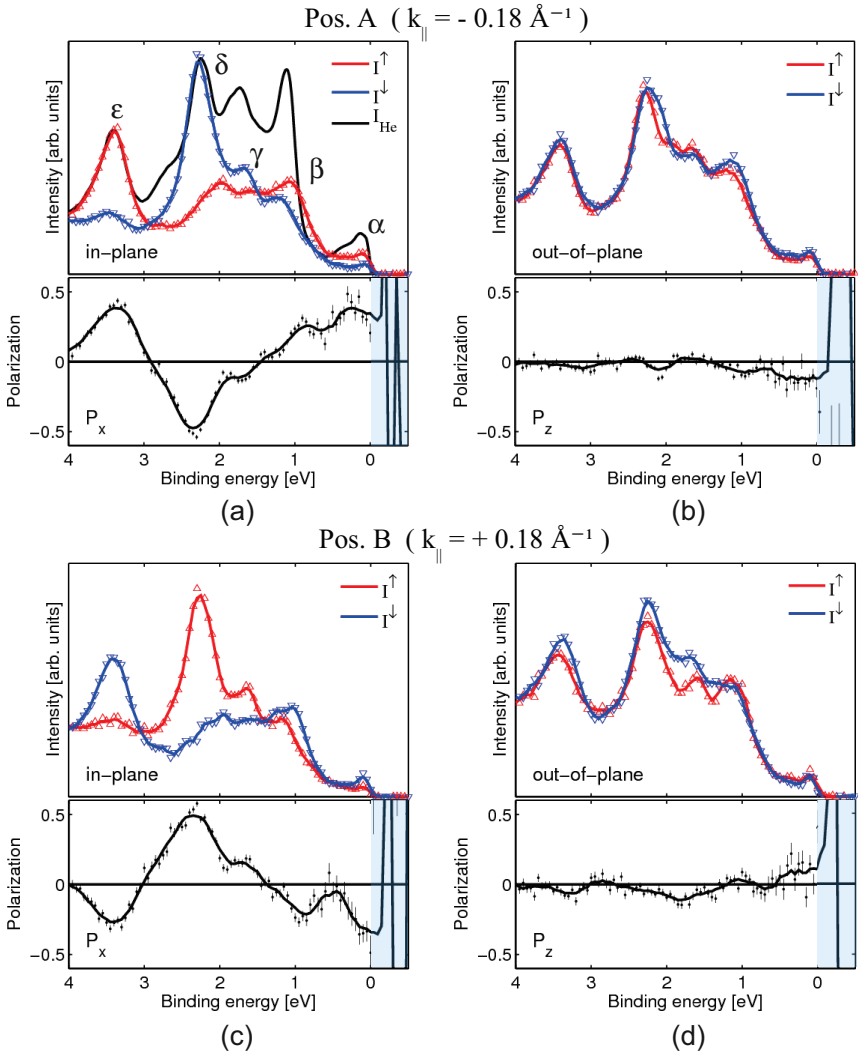

Figure 4.17: *Wide range spin-polarized spectra of the Bi_2Te_3 states α-ϵ taken along the $\overline{\Gamma K}$ direction at $h\nu = 24$ eV at selected positions $|\boldsymbol{k}_{\parallel}| = 0.18$ Å. Red and blue solid lines are related to smoothed $I^{\uparrow}$ and $I^{\downarrow}$ intensities for the in-plane (a,c) and the out-of-plane (b,d) spin vector components at different $\boldsymbol{k}$-space positions A and B, respectively. (a) Black line (top) shows He I data integrated over the SPLEED entrance slit. The related spin polarizations P_x and P_z are shown below the corresponding intensity plots, whereas standard deviations are given by vertical error bars. The black curves are guides to the eye.*

SP-ARPES on Sb_2Te_3 thin films

Fig. 4.18 shows the experimental (k_x, k_y)-plot, which reveals a circular shape of the Fermi surface taken on a ~ 25 nm Sb_2Te_3 thin film. The relevant $\boldsymbol{k}$-positions for further spin measurements are indicated by the letters A and B. For the spin-polarized measurements the opposite parts of the circular Fermi surface were adjusted by means of the aforementioned optimized $\boldsymbol{k}$-space mapping procedure similar to the previous SP-ARPES measurements on Bi_2Te_3 thin films. The angular maps shown in panels (b) and (c) are in a very good agreement with the presented laboratory data. The sample adjustment was performed by tilting along the $\overline{\Gamma K}$ direction. The spin-resolved data were integrated over the entrance slit area of the SPLEED detector with the centres located at $k_{\parallel} = \pm 0.08$ Å^{-1} for position A or B, respectively.

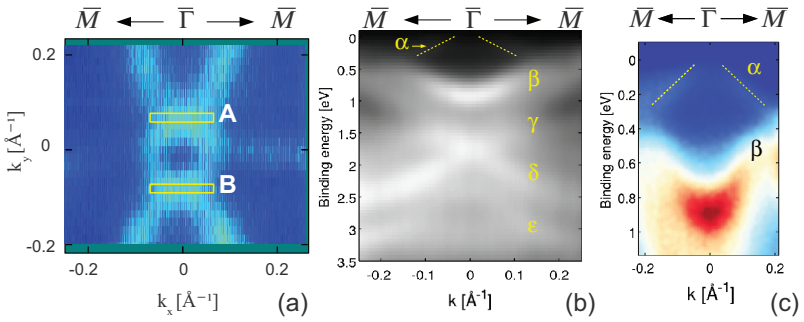

Figure 4.18: *Experimental Sb_2Te_3/Si(111) data. (a) Circular Fermi surface of the Sb_2Te_3 thin film structure taken at a photon energy $h\nu = 24$ eV indicating the $\boldsymbol{k}$-space areas A and B which are integrated in the spin-polarized experiment. Normal emission wide range (b) and (c) near Fermi level angular maps taken at ∼200 K with clear dispersive features α-ϵ. In panel (c) the Dirac cone state α and the Rashba-state β are shown. Dashed lines indicate the lower part of the Dirac cone.*

Figs. 4.19 and 4.20 show the spin-resolved results for the narrow and for the extended binding energy regions, respectively. In each figure, panels (a) and (b) display the *in-plane* P_x and *out-of-plane* P_z spin vector components for the position A, respectively. For the position B, the particular components P_x and P_z are plotted in panels (c) and (d), respectively. For each position the data acquisition time was in the order of 5 hours for the near Fermi level window, whereas a sufficient statistic was obtained within one hour for the wider binding energy region. The detected spin-

polarized signals were integrated over the SPLEED detection area of 0.03×0.1 Å^{-2} with the centres located at $k_{\parallel} = \pm 0.08$ Å^{-1} for the position A or B, respectively. In following, the same definitions and data acquisition procedures as already described in the case of the spin-polarized Bi_2Te_3 measurements are used.

Near the Fermi level, the Dirac cone feature carries a significant P_x spin polarization contribution. Similar to the Bi_2Te_3 measurements a clear spin reversal between the two opposite rim positions has been observed. For example, on the position A ($k_{\parallel} = -0.08$ Å^{-1}) at $E_B = 0.05$ eV binding energy the *in-plane* component shows a polarization value of $P_x \sim 15\%$. As expected, on the opposite side of the Fermi surface a value of $P_x \sim -15\%$ has been measured confirming the helical spin nature of the electrons within the Fermi surface. Around $E_B = 0.5$ eV the *in-plane* vector component reaches another maximum with values of $P_x \sim \pm$ 30%. This feature is attributed to the upper part of the state β, which is shown in more detail in the wide energy window scans depicted in Fig. 4.20. Here, the intensity peaks are indicated by the letters α-ϵ and relate to the dispersive features shown in Fig. 4.18(b). The highest spin polarization values were obtained from the state β. An overview of the experimental spin polarization values for the *in-plane* and *out-of-plane* spin vector components is summarized in table 4.4.

Moreover, spin-resolved photoemission experiments were performed on cleaved Sb_2Te_3 thin film samples. Fig. 4.21 depicts the spin-polarized spectra taken at position A ($k_{\parallel} = -0.08$ Å^{-1}). Clear spin-polarized features similar to those obtained from annealed samples are visible.

Sb_2Te_3/Si(111)		Pos. A		Pos. B	
Dispersions	E_B [eV]	$P_x \pm \sigma_{P_x}$	$P_z \pm \sigma_{P_z}$	$P_x \pm \sigma_{P_x}$	$P_z \pm \sigma_{P_z}$
α	0.05	0.15 ± 0.05	-0.02 ± 0.05	-0.19 ± 0.05	0.03 ± 0.05
β	0.35	0.36 ± 0.07	0.08 ± 0.08	-0.18 ± 0.10	-0.04 ± 0.11
γ	1.60	-0.19 ± 0.04	-0.02 ± 0.04	0.20 ± 0.05	-0.01 ± 0.04
δ	2.20	-0.23 ± 0.04	-0.07 ± 0.04	0.16 ± 0.04	0.03 ± 0.04
ϵ	2.90	0.18 ± 0.04	-0.02 ± 0.04	-0.14 ± 0.04	0.05 ± 0.04

Table 4.4: *Experimental spin polarization values for the Sb_2Te_3 energy band dispersions $\alpha, \beta, \gamma, \delta$ and ϵ investigated at the $\mathbf{k}$-positions A and B for chosen binding energy positions. The standard deviations σ_{P_x} and σ_{P_z} of the in-plane and out-of-plane spin polarization components are given.*

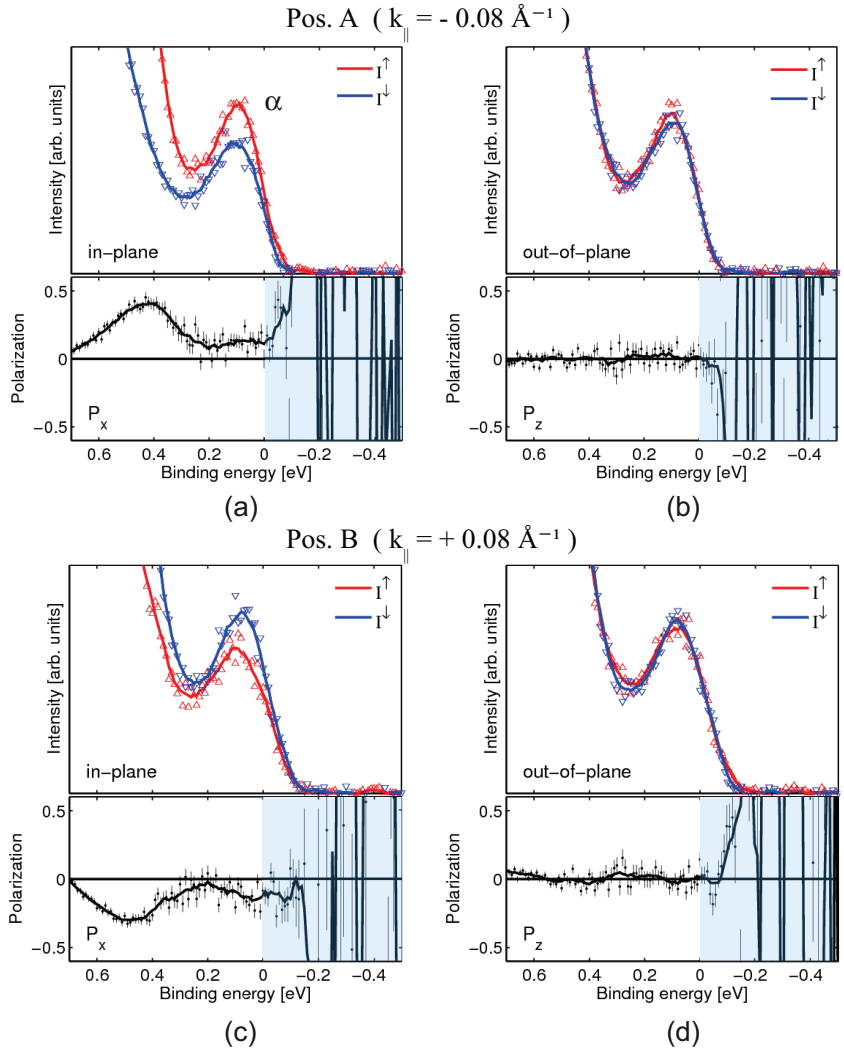

Figure 4.19: *Spin-polarized spectra of the lower Sb_2Te_3 Dirac cone α taken along the $\overline{\Gamma K}$ direction at $h\nu = 24$ eV at selected positions $|\boldsymbol{k}_{\parallel}| = 0.08$ Å^{-1}. Red and blue solid lines are related to smoothed $I^{\uparrow}$ and $I^{\downarrow}$ intensities for (a,c) the in-plane and (b,d) the out-of-plane spin vector components at different $\boldsymbol{k}$-space positions A and B, respectively. The related spin polarizations P_x and P_z (black dots) are shown below the corresponding intensity plots, whereas standard deviations are given by vertical error bars. The black curves are guides to the eye.*

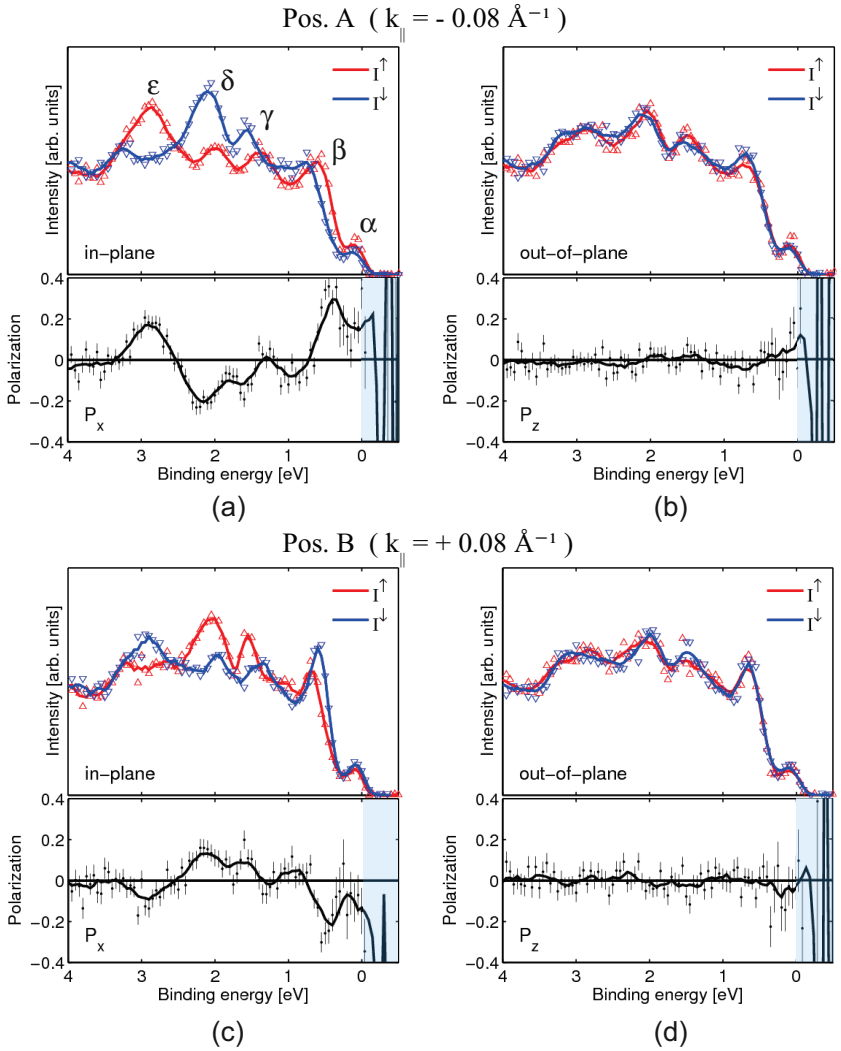

Figure 4.20: *Wide range spin-polarized spectra of the Sb_2Te_3 states α-ϵ taken along the $\overline{\Gamma K}$ direction at $h\nu = 24$ eV at selected positions $|\boldsymbol{k}_{\parallel}| = 0.08$ Å^{-1}. Red and blue solid lines are related to smoothed $I^{\uparrow}$ and $I^{\downarrow}$ intensities for the in-plane (a,c) and the out-of-plane (b,d) spin vector components at different $\boldsymbol{k}$-space positions A and B, respectively. (a) Black line shows He I data integrated over the SPLEED entrance slit. The related spin polarizations P_x and P_z (black dots) are shown below the corresponding intensity plots, whereas standard deviations are given by vertical error bars. The black curves are guides to the eye.*

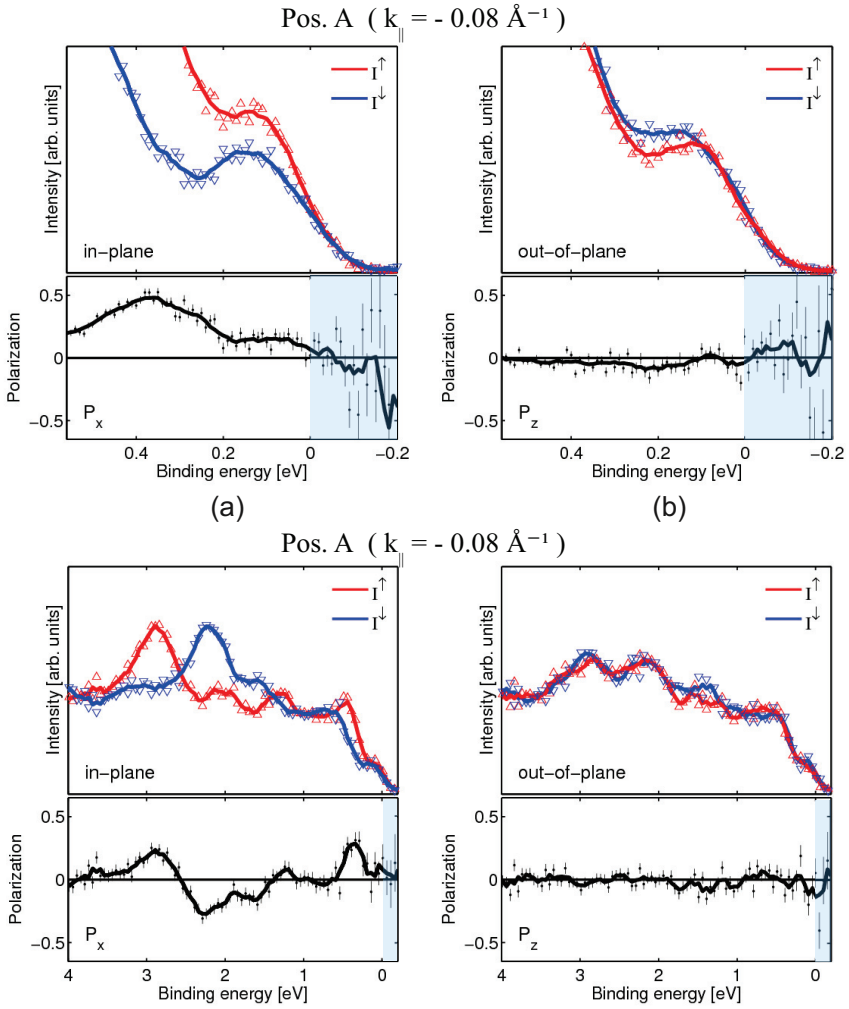

Figure 4.21: *Spin-polarized spectra of the cleaved Sb_2Te_3 thin film sample taken along the $\overline{\Gamma K}$ direction at $h\nu = 24$ eV at selected position $k_{\parallel} = -0.08$ Å^{-1}. Red and blue solid lines are related to smoothed $I^{\uparrow}$ and $I^{\downarrow}$ intensities for (a,c) the in-plane and (b,d) the out-of-plane spin vector components. The related spin polarizations P_x and P_z (black dots) are shown below the corresponding intensity plots, whereas standard deviations are given by vertical error bars. The black curves are guides to the eye.*

4.3.4 Comparison to DFT calculations

The presented SP-ARPES results show clearly, that the Dirac cone surface states of the 3D TIs Bi_2Te_3 and Sb_2Te_3 are not fully spin-polarized as assumed in the few-band phenomenological models [6]. A more detailed analysis of such states can be performed by using the DFT scheme including periodic boundary conditions. DFT calculations, which included the realistic atomic lattice, showed that the average spin polarization of the topological surface states is strongly reduced due to the presence of strong SOC (electron-volt magnitude), which causes an entanglement of the spin and orbital momentum degrees of freedom [6]. Moreover, the vector of spin polarization was found to change its orientation between the subsequent atomic layers resulting in a reduced averaged polarization value [7,8]. In particular, a layer resolved spin mapping analysis of the topological states showed a variation in the spin-helicity and an oscillatory behaviour of the P_z spin vector component in the Dirac cone [7]. Here, the rotation direction was reversed at the topmost Te atom which was comparable to the oscillatory layer resolved SOC contributions in Pb quantum-well states [7, 140]. Recently, experimental investigations were reported from bulk Bi_2Se_3 and Bi_2Te_3 samples [3,4] finding *in-plane* spin polarization values of up to $\sim 75\%$ and $\sim 60\%$, respectively.

In order to perform a consistent analysis of the photoemission experiment the electron scattering length has to be taken into account. In the kinetic energy range related to the VUV photon energy range, which was so far used in all the spin-polarized photoemission experiments on Bi_2Te_3 and Sb_2Te_3 materials, the mean free path of the electrons is in the order of 10 Å or less. Therefore, the effective probing depth of the photoemission experiment is in the order of several atomic layers, and the resulting measured spin polarization should in first approximation agree with the value integrated along the z axis over the surface QL. Nevertheless, the resulting average spin polarization of the emitted photoelectrons is a function of the symmetry of the particular states, the polarization degree, and the incidence angle of the beam.

In order to explain the experimental data our collaborators from the neighbouring institute PGI-1, Dr. Bihlmayer and Prof. Dr. Blügel, have performed dedicated *ab initio* calculations of the Bi_2Te_3 surface electronic structure based on the full-potential linear augmented plane wave (FLAPW) method as implemented in the

FLEUR code (for details see Ref. [54]). The results were obtained within the DFT scheme employing the local-density approximation (LDA), whereas SOC was included self-consistently as described in Ref. [130].

Fig. 4.22(a) illustrates the expectation values of the spin polarization along the *in-plane* and *out-of-plane* axes, where the *in-plane* (left) and *out-of-plane* (right) spin vector components share the same plot. The different colors mark different spin directions. The size of the circles gives the absolute spin polarization of the states for the *in-plane* P_x and *out-of-plane* P_z components. As can be seen, there exist several distinct spin-polarized states, which are localized in the surface QL. The photoelectron mean free path λ has been taken into account in reference to the experiment. Two states, namely α and δ, analyzed in the further drawings, are indicated by arrows. In Fig. 4.22(b) the calculated weight is overlaid with an experimental normal emission angular $E_B(\boldsymbol{k})$ map taken along the $\overline{\Gamma K}$ direction, which fits nicely after a Fermi level shift by 0.45 eV. The nature of the spin polarization limit in the surface localized states can be understood in terms of local depth-resolved spin density and charge density analysis. In particular, emphasis will be put on the Dirac cone state α and the highly spin-polarized δ state shown in the SP-ARPES results.

The calculated depth-resolved spin contributions are given in Figs. 4.22(c)-(h) for $|\boldsymbol{k}_\parallel| = 0.18$ Å^{-1} related to the center position of the spin detector integration area as shown in Fig. 4.15(c), which is also indicated by the arrow positions in Fig. 4.22(a). The spin density for the atom η is modelled as

$$\rho^{\eta}_{\boldsymbol{k}_\parallel} = (n^{\uparrow}_{\eta} - n^{\downarrow}_{\eta}), \tag{4.8}$$

whereas the photoelectron mean free path λ is taken into account in the corresponding spin polarization values by the expression

$$P = \sum_{\eta} e^{-z_\eta \lambda}(n^{\uparrow}_{\eta} - n^{\downarrow}_{\eta}). \tag{4.9}$$

In Fig. 4.22(d) the spin density plot reveals, that the observed spin polarization predominately has p_z character. As shown in Fig. 4.22(e), the direction and magnitude of the spin polarization vector of the corresponding states depend on the distance from the surface, with clear spin reversal taking place within the 2 Å surface region in case of the Dirac cone state α, which is in a fair agreement to a

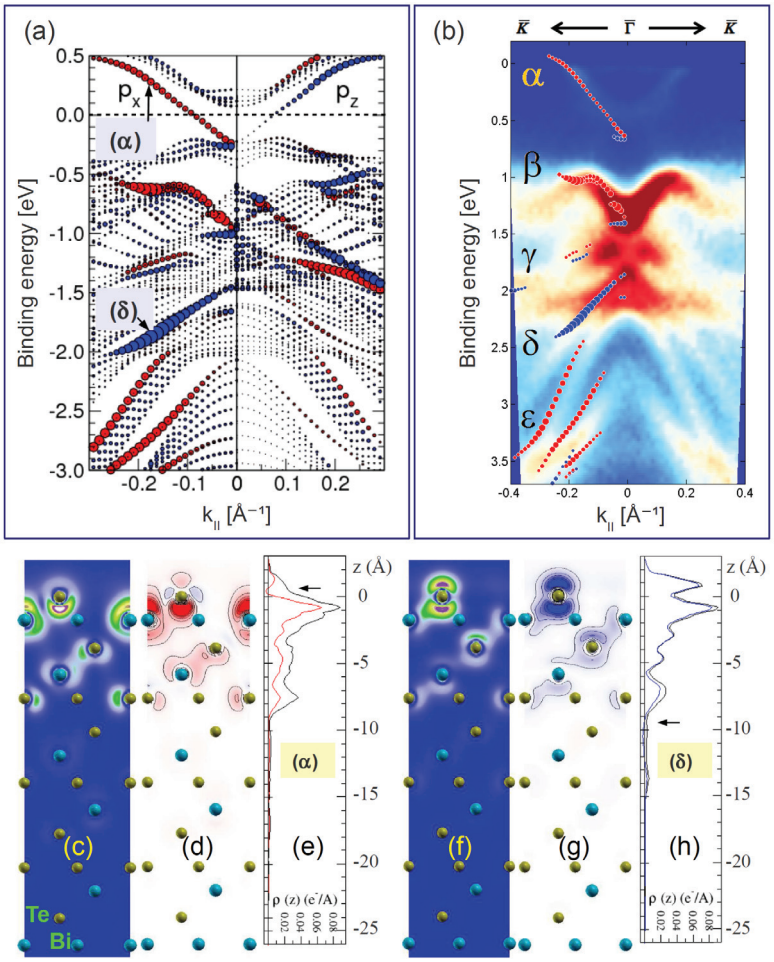

Figure 4.22: *(a) Simulated spin-polarized spectral weight of the 6 QL Bi_2Te_3 slab along the $\overline{\Gamma K}$ direction. (b) Photoemission map of the Bi_2Te_3 thin film taken at 15 K using the He I ($h\nu \approx 21.22$ eV) excitation along the $\overline{\Gamma K}$ direction, with the overlaid DFT in-plane calculation. Blue and red solid circles indicate the spin direction, whereas the size of the symbols is related to the weight of the states at the surface. Panels (c) and (f) show charge, and (d) and (g) spin densities plotted in real space integrated over the (x,y)-plane for the α and δ state at $|\boldsymbol{k}_{\|}| = 0.18$ Å^{-1}, respectively. (e) and (h) show charge and spin densities for those states with respect to the distance from the surface. Arrows in panels (e,h) denote spin-reversals taking place for each state.*

previous study [7]. Using the exponential decay from eq. 4.9, the spin polarization over the first QL is highest for the state indicated by δ in Fig. 4.22(a). The spin density of the δ-state with respect to the distance from the surface is plotted in Fig. 4.22(h). Unlike the Dirac cone, in this state the spin reversal takes place only in the bottom layer of the surface QL, ~ 9 Å below the surface.

The difference between the Dirac cone state and the aforementioned δ-state is further depicted in charge and spin densities plotted in Figs. 4.22 (c,d) and (f,g), where clear spin reversal at the surface atom is observed for the Dirac cone state, while not observed for the δ state. Furthermore, one can clearly observe the strong, surface Te atom localized, p_z character of the δ state which has a Rashba-type spin polarization. In contrast, the Dirac cone state has a hybridized nature, with most charge related to the p_z state of the second layer Bi atom, but with a significant contribution of the reversed spin from the surface layer Te atom. The Dirac-cone state has a smaller polarization, due to the polarization inversion above the topmost Te atom (local spin-reversal). The *in-plane* polarization value integrated over the first QL is about 46%, in contrast to the surface state δ that has 85%. In the experimental data the predicted 85% polarization of the δ state cannot be directly observed since at higher E_B spectral features are broadened and even in the presence of local gaps the spectral weight contains significant contributions from the bulk band structure. The helicity of the surface features in Bi_2Te_3 is not only a feature of the Dirac cone topological state, it is a general feature for all surface related states, as is the significant *out-of-plane* component present predicted for some of these states.

4.4 Conclusions

In this chapter, the surface electronic properties of the MBE-grown Bi_2Te_3/Si(111) and Sb_2Te_3/Si(111) 3D TI thin films have been investigated by means of low-energy spin- and angle-resolved photoemission experiments. It was shown, that the topological protection mechanism of *in situ* cleaned thin films leads to spin-polarized helical single branched Dirac cone states at the Fermi level.

The resulting high-resolution ARPES data is of similar quality as those obtained on cleaved single crystals or on thin films never exposed to the air. The existence of clear and sharp surface states confirms the high quality of the prepared samples. In addition, the insensitivity of topologically protected Bi_2Te_3 Dirac cone surface state to surface induced perturbations caused by the cleaning process has been confirmed. These observations agree nicely with other studies reported in Refs. [2, 141–144] showing the topological nature of time-reversal protected surface states. Furthermore, a reduction of the conduction band contribution with increasing sputtering time and decreased film thickness has been observed. This fact might be important for future spintronic applications requiring a well-defined TI surface state.

The presented spin-polarized measurements were carried out at the synchrotron radiation beamline 5. We find, that there exists a set of spin-polarized states in the Bi_2Te_3 and Sb_2Te_3 electronic band structure, which contains the Dirac cone states and additional states localized within the surface QL at higher binding energies. In both material systems, for all spin-polarized surface states, the antisymmetric helical spin property $\boldsymbol{\sigma}(\boldsymbol{k}) = -\boldsymbol{\sigma}(-\boldsymbol{k})$ is confirmed by the measured spin reversals for two opposite wave numbers. For the Bi_2Te_3 thin film the experiments show the strong Fermi surface warping predicted by theory, with both *in-plane* and *out-of-plane* spin polarization components. The topological protection mechanism in Bi_2Te_3 results in an *in-plane* experimental polarization value up to $\sim 45\%$ for the Dirac cone and in the wider range up to $\sim 55\%$ for the most pronounced δ feature at $E_B = 2.3$ eV. For the warped parts, an *out-of-plane* polarization value of $\sim 15\%$ has been found. These results are in quantitative agreement with dedicated DFT simulations which find the Dirac cone related electron density delocalized over the over the first QL. The involved spin reversal over the first atomic layer results in an altered spin polarization, with the theoretical prediction of $\sim 46\%$ for the *in-plane* direction, when including the photoelectron information depth. These findings suggest, that

careful attention should be paid to the analysis of surface states probed by spin-polarized photoemission when different experimental geometry, photon energy, or light polarization is used. Without dedicated one step photoemission calculations the degree of those effects is difficult to estimate, and they could be used as an argument to explain the discrepancy between the results from this thesis and these of Souma *et al.* [4] and Xu *et al.* [125].

5 Growth and characterization of the CCA half-metallic full Heusler alloy

This chapter is dedicated to the *in situ* thin film growth and the electronic properties of the ternary intermetallic Co_2CrAl Heusler alloy compound. In order to understand the underlying physical properties of the prepared thin films, it is important to first summarize the basic relations of the theoretical framework which governs the structural and electronic properties of half-metallic full-Heusler alloys. I follow the survey articles by Galanakis [13–15, 145, 146].

5.1 Introduction

The discovery of the Heusler alloys dates back to 1903 when F. Heusler first synthesized a Cu_2MnAl alloy expecting useful properties for the steel industry. This material showed a strong ferromagnetic behaviour although the alloy was made of a combination of non-magnetic elements. Later studies have revealed that the ferromagnetic order is associated with the onset of an ordered cubic phase [147] representing the Heusler alloys. Thereafter, the theoretical description of the so-called half-metallicity in the prototype alloy NiMnSb by de Groot *et al.* in 1983 [148] initiated a new research area of tremendous scientific interest especially due to the proposed full spin polarization being important for future efficient spintronic devices. A typical half-metal represents a hybrid structure comprising a metallic behaviour in the majority spin band structure and a semiconducting behaviour in the minority spin band structure [148]. In an ideal case this fact leads to a fully spin-polarized electron occupation within the material near the Fermi level. Fig. 5.1 shows a schematic representation of the density of states (DOS) for a conventional metallic and semiconducting material in comparison to a half-metal.

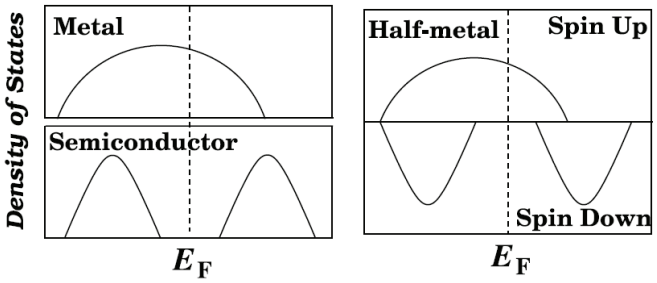

Figure 5.1: *Sketch of the density of states for metal and semiconductor materials (left) as well as for a half-metallic compound (right). The sketch was adapted from [14].*

The Co-based half-metals are of special interest mainly due to their ferromagnetic nature related to high Curie temperatures extending over the range from 1100 down to 95 K and high magnetic moments [149]. In modern condensed matter physics these materials remain attractive since they can be used as ferromagnetic electrodes of magnetic tunnel junctions (MTJ). Briefly, a simple MTJ structure consists of a thin insulating layer placed between two ferromagnetic half-metals. The sandwiched insulator, such as MgO, acts as a tunnel barrier. Assuming spin-polarized electrodes, the application of a voltage causes a spin-dependent tunnelling of the charge carriers. The resistance of a MTJ structure depends on the relative orientation of the two magnetization directions of the electrodes. In general magnetotransport phenomena are referred to the tunnel magnetoresistance (TMR) and giant magnetoresistance(GMR) effects with details described in Refs. [150–153]. In the simple model of Julliere [154] the resulting TMR value is given by

$$TMR = \frac{2P_1P_2}{1 - P_1P_2}. \tag{5.1}$$

Herein, P_1 and P_2 are the spin polarization values of the upper and lower electrodes, respectively [155]. In an ideal case, full spin-polarized $P_1, P_2 \sim 100\%$ electrode materials would lead to an infinitely large TMR ratio providing the possibility of the fabrication of a efficient spin-MTJ switching device.

Indeed, theoretical bulk band structure calculations predicted a full spin polarization for several Co-based full-Heusler alloys [13,156]. However, the degree of the spin polarization is very sensitive to structural conditions as well as to extrinsic factors,

such as segregation or adsorption effects. Taking the Co_2CrAl (CCA) compound as example, Miura *et al.* have shown, that the P value can be reduced by atomic disorder effects between the Co and Cr atoms, whereas Cr-Al type disorder does not affect the half-metallicity. Moreover, Galanakis *et al.* proposed that the degree of spin-polarized electrons depends strongly on the surface termination [15]. In his work surface electronic band structure of several Heusler alloys has been studied by means of *ab initio* calculations in the framework of the DFT approach. It could be shown, that different surface effects, such as surface states appearing in the gap for different surface terminations, lead to a loss of the spin polarization contrary to previous bulk related calculations. Among considered compounds, however, the CrAl-terminated CCA surface preserves the proposed half-metallicity at the Fermi level up to a surface spin polarization value of about $P \sim 84\%$.

These facts may explain the relatively small polarization values obtained from spin-polarized photoemission measurements up to now. For a Co_2MnSi sample, spin-polarized photoemission measurements yield a polarization value of $P \sim 12\%$ [157]. Spin polarization values of $P \sim 20\%$ [158] and $P \sim 45\%$ [158] were observed on sputtered and annealed $Co_2Cr_{0.6}Fe_{0.4}Al$ sample surfaces. Herein, the discrepancy between the observed results and the theoretical predictions may be explained by surface distortions caused by the chemical etching using the sputter method. Recently, a value of $P \sim 34\%$ was reported from *in situ* prepared Co_2MnGa thin films [159]. Herein, the authors referred the reduced polarization to atomic disorder effects which markedly reduced the magnetic moment of the thin film. It should be noted, that the PES results were obtained *in situ* directly after the preparation procedure without any air-exposure of the samples. The above survey of recent results indicates, that an exceptional attention needs to be paid to the surface structural order by means of a complete *in situ* realized preparation and characterization experiment. Thus, surface sensitive investigations on clean and well-ordered sample surfaces without sputtering induced surface structure distortions or roughness can be achieved. The aim of this work is therefore to provide a technological basis for future spin-and angle-resolved photoemission studies on *in situ* prepared Heusler alloy thin film samples. For this purpose the Co_2CrAl full-Heusler compound is taken as exemplary material mainly due to its proposed high surface spin polarization. Next, the crystal structure and the electronic properties of Co-based full-Heusler materials will be outlined.

5.2 Crystal structure

Heusler alloys are split up into two family classes with respect to their crystal structure. Both lattice types are shown in Fig. 5.2. The ternary full-Heusler alloys, with a chemical composition X_2YZ, crystallize in the $L2_1$ (space group no. 225:$Fm\bar{3}m$) structure characterized by four sets of interpenetrating fcc sublattices[1]. In general X and Y represent transition metals elements whereas Z is assigned to semiconducting or non-magnetic element. Here, the X atoms are placed on the (0, 0, 0) and (1/2, 1/2, 1/2) positions in Wyckoff coordinates occupying the cubic A and C sublattices, while B and D sublattices are occupied by the Y and Z atoms located at the (1/4, 1/4, 1/4) and (3/4, 3/4, 3/4) positions. The second family is known as the half-Heusler alloy XYZ compounds which crystallize in the $C1_b$ structure. In contrast to the full-Heusler alloys, only one Co sublattice is occupied whereas the other remains empty.

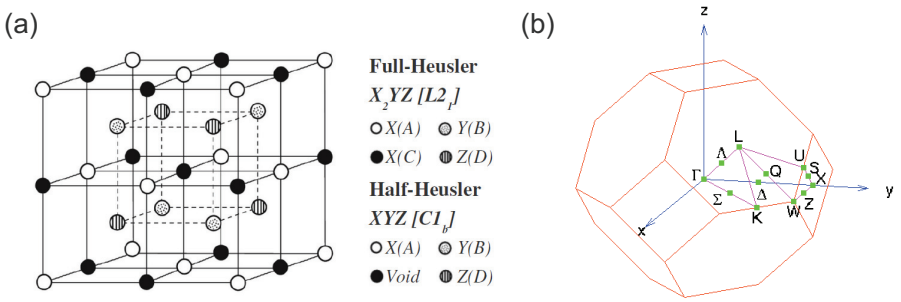

Figure 5.2: *(a) Representation of the full- and half-Heusler alloy families formed in $C1_b$ and $L2_1$ structures, respectively. The occupation of the sublattices by X, Y and Z atoms is also shown. Typical occupants are transition metals Au, Co, Cu, Fe, Ni, Pd, etc. for the X- and Cr, Mn, Ti, V, etc. for the Y-sites. The Z-sites are sp-like elements such as Al, Ge, Ga, Sn or Sn, etc. For particular Wyckoff positions see text. The schematic representation was adapted from [161]. (b) Brilloin zone of the fcc lattice and related high-symmetry lines. Taken from [162].*

By taking the full-Heusler alloy Co_2CrAl as an example, each Cr or *sp* atom has eight Co atoms as first neighbours, placed in an octahedral symmetry position, while each Co atoms has four *sp* atoms as first neighbours. The whole crystal

[1]We follow here the notation from [160]

has a tetrahedral T_d symmetry [146]. In case of an atomic interchange between different sublattices, the highest ordered $L2_1$ phase will be degraded to lower ordered structures B2, DO_3 and A2 [146]. A random partial swap (with a 0.5 occupation probability) of atoms between the Y and Z sublattices, results in the B2 structure. A DO_3 type of disorder can be obtained by interchanging the Co and Y atoms. The lowest ordered structure is referred to the A2 structure showing a randomly occupied crystal structure in all sublattices. The type of disorder can be determined from X-ray diffraction and neutron scattering experiments by analysing the intensity ratios of the Bragg reflections.

5.3 Electronic structure of Co_2-based full-Heusler alloys

Origin of the band gap

In case of Co_2-based compounds, a detailed theoretical explanation describing the formation of a minority energy band gap was first provided by the pioneering work of Galanakis *et al.*, with details explained in Ref. [13]. I follow this work and give only a qualitative picture of the band gap formation in the vicinity of the Fermi level.

The underlying process is characterized by two hybridization steps and is schematically shown in Figure 5.3. As can been seen, only d-states of the X and Y constituents are taken into account. Detailed information concerning symmetry group representations of the involved electronic structure is given in Ref. [13]. Taking the Co_2MnSi compound as an example, these are mainly couplings between the Co-Co hybrid and Mn atoms. Due to the crystal field splitting there exist five degenerate d-orbitals, with energetically separated twofold d_{z^2}, d_{x^2-y2} and threefold d_{xy}, d_{yx}, d_{zx} states related to the involved octahedral[2] complex formation as shown in Fig. 5.3. Since the Co atoms form a simple cubic lattice with each Co atom surrounded by 6 other Co atoms, the crystal field splitting is such that $E_{e_g} > E_{t_{2g}}$ [14]. In a first step, the hybridization between two Co atoms leads to bonding e_g (or t_{2g}) and antibonding e_u (or t_{1u}) orbitals, which can be attributed to symmetry notations given in Ref. [163]. The second hybridization refers to the interaction between the Co-Co

[2]Note that the lattice consisting the Co atoms has the O_h symmetry.

orbitals and the Mn d-orbitals. Specifically, the doubly-degenerated Co e_g orbitals couple with the d_{z^2} and $d_{x^2-y^2}$ Mn orbitals forming a doubly-degenerated bonding and antibonding e_g states, that are established below and above the Fermi level, respectively. The 3xt_{2g} Co states hybridize with the d_{xy}, d_{yx}, d_{zx} (t_{2g}) orbitals of the Mn atoms resulting in two split threefold degenerated bonding and antibonding t_{2g} orbitals situated at lower and higher energies, respectively. However, due to missing Mn hybridization partners the remaining non-bonding Co 2xe_u and 3xt_{1u} states form an energy gap around the Fermi level.

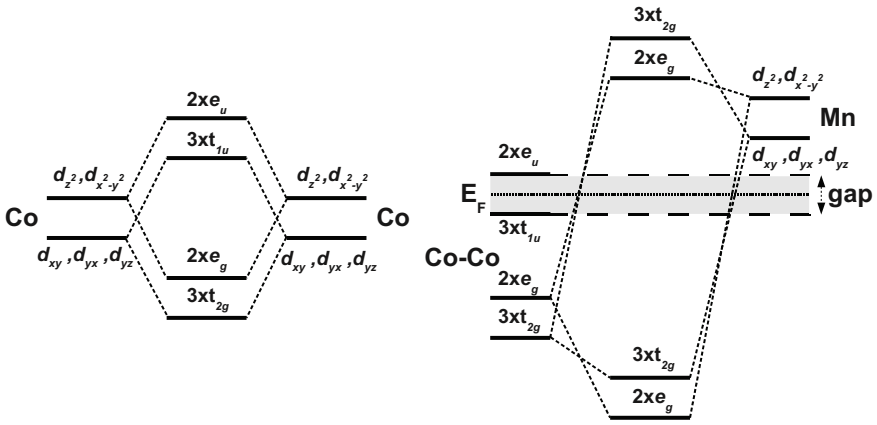

Figure 5.3: *Schematic representation of the minority band gap evolution at the Fermi level E_F for the Co_2MnSi full-Heusler alloys. Shaded area indicates the half-metallic band gap. Adapted from [146].*

The theoretical spin-resolved bulk electronic band structure for the Co_2CrAl material is shown in Fig. 5.4. The calculation was performed using the linear augmented-plane wave (LAPW) method as implemented in the WIEN2k package within the scheme of the density functional theory (DFT) using $100k$ k-points. The exchange-correlation potential was taken into account by means of the generalized gradient approximation (GGA) of Perdew, Burke, and Ernzerhof [126]. For the fcc structure an experimental lattice constant value of $a_{CCA} = 5.73$ Å [164] was used. Panels (a) and (b) show the calculated band structures for the majority and minority spin channels, respectively. As can be seen, there is no energy gap for the spin-up electrons near the Fermi level. In particular, there exist crossings of the Fermi level

E_F along all high symmetry directions. Contrary, for the spin-down electrons (minority spin electrons) there exists an energy gap extended over all high symmetry directions indicating the half-metallic behaviour of that material. This calculation agrees well with that presented in Ref. [165].

Fig. 5.5 shows the spin-resolved DOS for the majority and minority spin channels which was calculated using the WIEN2k code.

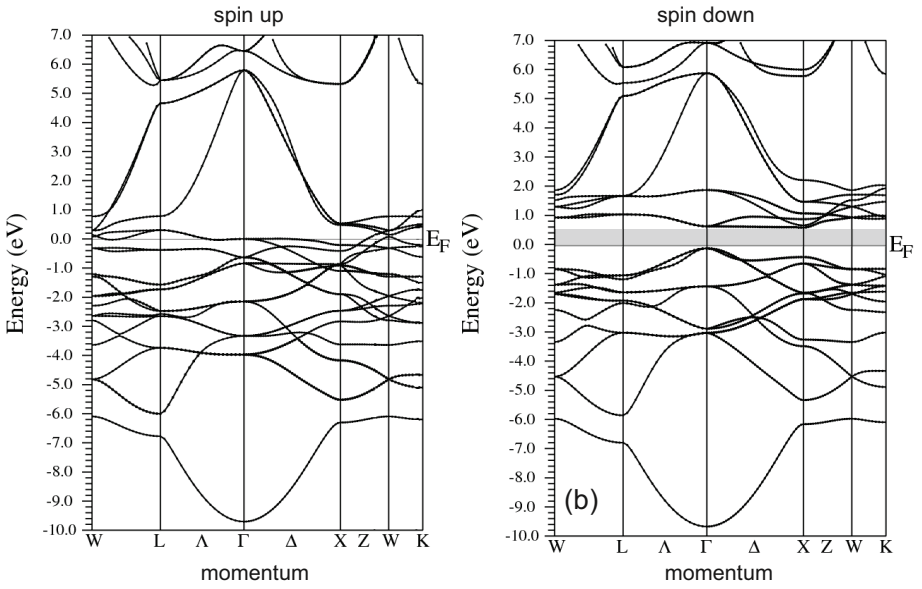

Figure 5.4: *Calculated spin-resolved bulk band structure calculation of the Co_2CrAl compound for (a) majority (spin up) electrons and (b) minority (spin-down) electrons along high symmetry lines in the fcc Brillouin zone. Shaded area is the half-metallic band gap within the minority spin channel.*

5.4 Experimental results

5.4.1 Growth and characterization of Co_2CrAl thin films

The preparation of the Co_2CrAl thin film samples was carried out in the UHV preparation chamber with technical details described in chapter 3. In order to explain the deposition procedure I make use of the schematic drawing displayed in Fig. 3.6.

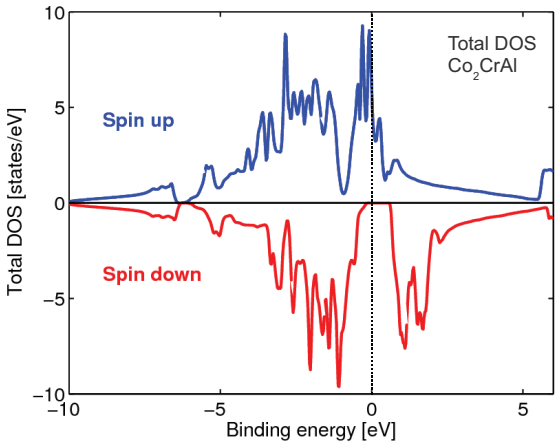

Figure 5.5: *Calculated total spin-resolved DOS of the bulk Co_2CrAl Heusler alloy for majority (spin up) electrons (spin-up) and minority (spin-down) electrons. The dashed line indicates the Fermi level.*

Due to a relatively small lattice mismatch of $\sim$ 3% between the Co_2CrAl compound ($a_{CCA} \sim 5.73$ Å [164]) and the diagonal length of a MgO ($\sqrt{2} \cdot a_{MgO} = 5.95$ Å), a (001)-oriented MgO single crystal has been chosen as the substrate material [166], see Fig. 5.6. According to this, the CCA film grows epitaxially preferably with its [001] direction rotated by 45° with respect to the bulk unit cell of MgO.

Prior to the insertion into the vacuum, the substrates[3] were ultrasonically pretreated in ethanol. Subsequently the substrates were introduced via the loadlock into the UHV preparation chamber PREP II, where they were cleaned by means of a sputter and annealing cycle. After degassing the sample around $T = 500$ °C for about

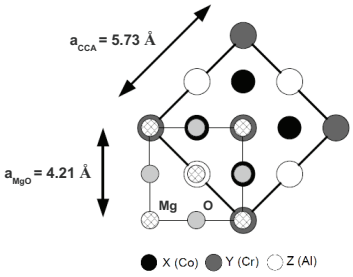

Figure 5.6: *Sketch of the superimposed CCA and MgO crystal structures (top view). The cubic unit cell of CCA is rotated by 45° compared to that of the MgO. Taken from [166].*

[3]Dimension: $\sim$ 10 mm x 10 mm x 0.5 mm

$\sim$ 20 min, the MgO surface was sputtered with Ar-ions at 500 eV at a pressure of $p \sim 6.5 \cdot 10^{-6}$ mbar for about $\sim$ 5 min. During sputtering the sample was held at room temperature and positioned at an angle of 45° with respect to the incident ion beam. Subsequently, the sample was annealed around 550 °C for $\sim$ 15 min and finally cooled down below a temperature of 100 °C.

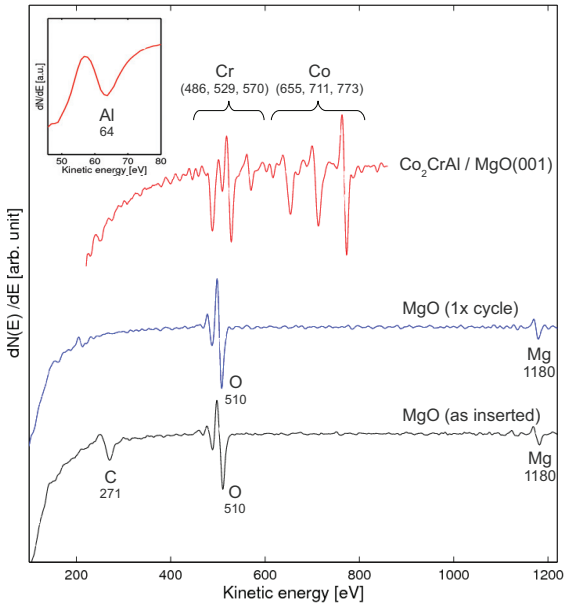

Figure 5.7: *Chemical AES analysis before and after thin film deposition taken at 3 keV primary electron energy. Before: MgO substrate as inserted (black) and cleaned MgO substrate (blue). After: Co_2CrAl/MgO(001) thin film structure (red). The inset shows the Al peak Auger position. The corresponding Auger electron energies are given for the most pronounced peaks. For a better visibility the spectra are shifted by a factor of 5 against each other.*

The amount of C contaminants was checked by means of AES whereby electron energies of $E_{AES} = 3$ keV have been used. Fig. 5.7 shows the Auger spectra of the MgO substrate taken before and after one cleaning cycle. In Fig. 5.8 the LEED pattern of the cleaned (001) surface reflects an ordered structure. The red square indicates the cubic unit cell. In the meantime the sputter source has been pre-sputtered for about 5 min in order to remove eventual target contaminants whereas

valve v1 was kept closed. The clean substrate was transferred from the PREP I chamber to the sputtering chamber PREP II (see path: T1 transfer → 3-way cross → T2 transfer) for the thin film deposition. Here, W1 labels an interchange point where the sample can be transferred using a standard wobble stick device. In the experimental geometry used the substrate was positioned above the sputter source head.

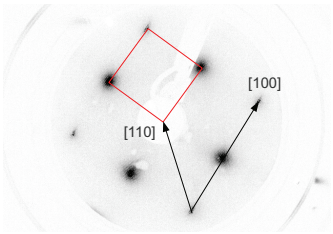

Figure 5.8: *Inverted contrast picture of the experimental LEED picture of the cleaned MgO(001) single crystal sample surface taken at 80 eV primary electron energy. The red square indicates the cubic unit cell.*

Initially, the CCA films were deposited at room temperature without the application of a substrate heating. For the deposition process a constant flow of Ar gas (purity: 99.99999%) was introduced by a variable leak valve, whereas the valve v2 was closed in order to maintain the vacuum in the rest system. By using a laboratory 100 bar gas bottle a pressure accuracy of $\pm 0.1 \cdot 10^{-2}$ mbar was obtained. Due to possible heat loads during the sputter process, the source head temperature was held around room temperature by using the installed water-cooling system. Moreover, the installed turbo pump was set to a standby modus and was separately water-cooled. The deposition was stopped after 60 min. After the deposition process the CCA/MgO(001) sample was transferred back to the PREP I chamber for further characterization. The AES result plotted in Fig. 5.7 shows the high purity of the resulting film surface, with absent O and C contaminants. For the sample grown at room temperature no diffraction pattern was observed in LEED. In order to obtain more informations about the desired growth parameters yielding to a B2 or even a $L2_1$ crystal structure, the crystal structure was analyzed by means of X-ray diffraction (XRD). Theoretical details can be found in Refs. [167, 168].

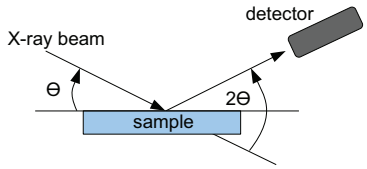

Figure 5.9: *Experimental XRD geometry of the* $\Theta - 2\Theta$ *scan mode.*

The XRD setup[4] with a Cu-Kα ($h\nu = 8047$ eV) source was provided by the group of Prof. Dr. M. Tolan[5]. The crystal structure of the films was investigated in the out-of plane $\Theta - 2\Theta$ geometry shown in Fig. 5.9. The sample was mounted onto a heatable sample stage located within a high vacuum chamber and annealed at different temperatures ranging from 150 °C to 650 °C for 1 h. After each annealing step the samples were cooled down to RT. The resulting XRD patterns are shown in Fig. 5.10.

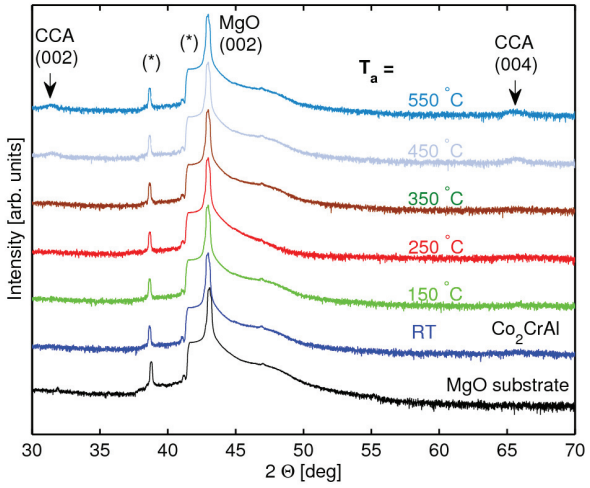

Figure 5.10: *XRD scans for a CCA thin film deposited on a (001)-oriented MgO single crystal at various annealing temperatures* T_a *ranging from 150 °C to 650 °C. The black curve represents the bare MgO substrate. The blue line is related to the thin film deposited at RT without annealing. For a better visibility the curves are vertically shifted with respect to each other. Asterisks denote the peaks from MgO (100) single crystal substrate.*

The MgO(001) pattern (black) is characterized by the (002) Bragg reflection. In the case of the Co_2CrAl full-Heusler alloy compound the crystallographic order is generally described by the characteristic (111) and (002) Bragg reflections. In

[4]D8 laboratory diffractometer, Bruker AXS, Germany
[5]Lehrstuhl Experimentelle Physik Ia, Technische Universität Dortmund, Germany

particular, the presence of both reflections indicates the fully ordered $L2_1$ structure or a pure Co-Cr disordered structure with a different intensity ratio [169]. The presence of only one (002) peak is related to the B2 structure with a full disorder on the Cr-Al positions. A disorder on all positions is classified by the absence of all intensity peaks. It has to be noted, that the off-specular (111) reflection was not accessible as a consequence of the scattering geometry. According to Fig. 5.10, the thin films deposited at room temperature possess the B2 structure after a post-annealing step above 450 °C as can be seen from the CCA(002) and CCA(004) reflections. In general, the (002) peak is the superlattice peak, whereas the (004) peak is related to the fundamental peak. It can be seen, that the degree of order increases with an increasing annealing temperature. Although our films show the (002) and (004) CCA reflections indicating a B2 structure, their intensities are not comparable to those shown in Ref. [170]. Based on this experience, the next CCA films were deposited on MgO substrates at various substrate temperatures T_s ranging from 300 °C to 600 °C. The sample temperature was controlled by a calibrated infrared pyrometer through a standard UHV viewport mounted on top of the preparation chamber. With the exception of the substrate temperature, the same growth parameters have been applied as used before. After the deposition no further annealing to the samples was applied. The prepared thin film surfaces were checked by LEED and AES.

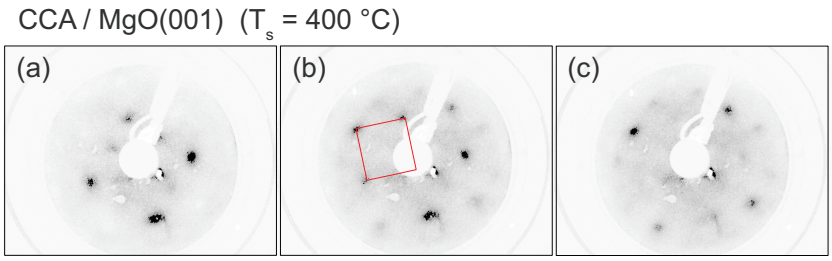

Figure 5.11: *Experimental LEED pictures of the prepared CCA/MgO(001) thin film structure deposited at a constant substrate temperature $T_s = 400\ °C$ taken at (a) 220 eV (b) 240 eV and (c) 250 eV primary electron energies. The red square indicates the cubic unit cell. For a better visibility the contrast has been inverted.*

Fig. 5.11 shows the LEED pictures of a prepared thin film deposited at $T_s = 400$ °C. The patterns were taken at different primary electron energies. The

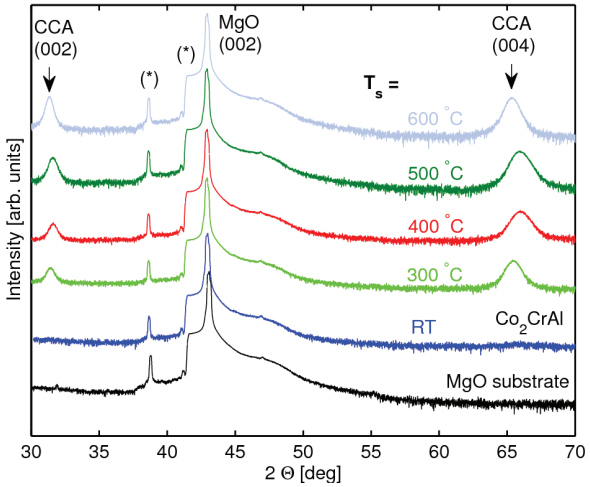

Figure 5.12: $\Theta - 2\Theta$ *scans of CCA/MgO(001) thin films prepared at different substrate temperatures* T_s *ranging from 300 °C to 600 °C. The blue line is related to the thin film deposited at RT. For a better visibility the curves are shifted by a factor of 5 against each other. Asterisks denote the peaks from MgO(100) single crystal substrate.*

surface shows a fourfold symmetry which is related to the cubic bulk lattice. A further annealing step around 350 °C, as it was suggested by Cinchetti *et al.* [171], did not increase the quality of the LEED pattern. The LEED picture was also present for the samples prepared at higher substrate temperatures suggesting an epitaxial growth for $T_s > 400$ °C. The structural information from the bulk material was further determined by XRD measurements.

The XRD scans of samples prepared at various substrate temperatures T_s are shown in Fig. 5.12. Again it could be shown, that the film deposited at RT did not show any clear structural peaks related to the CCA compound. Besides the MgO(002) substrate reflection, the measurements show clear CCA(002) and CCA(004) reflections for samples deposited at substrate temperatures T_s ranging between 300 °C and 600 °C. With an increasing substrate temperature, an intensity increase of those peaks was observed. At this point, it was possible to analyze the intensity ratio of the (002) and (004) Bragg reflections. For this purpose I use a simulation provided by *PowderCell* [172] which yields a ratio of I_{200}/I_{400} =0.39 for

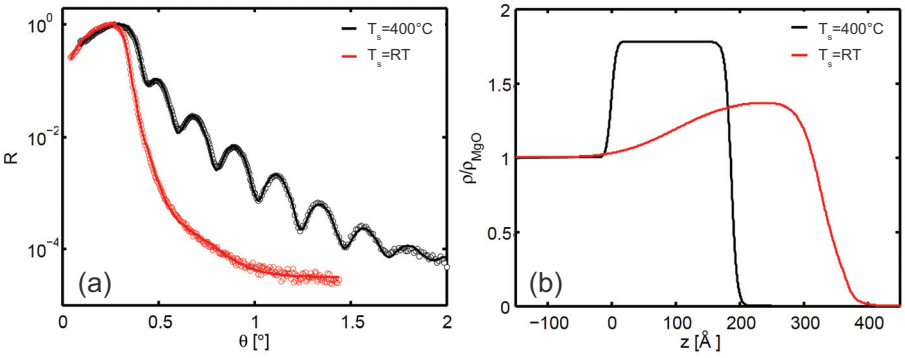

Figure 5.13: *(a) X-ray reflectivity data acquired from the CCA/MgO(001) thin films deposited at RT and at $T_s = 400\,°C$. (b) Electron density profiles obtained from a refinement of the reflectivity data.*

a full (100%) ordered B2 or $L2_1$ CCA structure. The structure parameter s_{B2} of the $B2$ structure can be expressed as [169]

$$s_{B2} = \frac{I_{(200)} \cdot sin(\Theta_{(200)})}{I_{(400)} \cdot sin(\Theta_{(400)})}, \tag{5.2}$$

which includes a geometrical correction by the sin-terms due to the thin film geometry. According to this, the obtained ratios s_{B2} for the films deposited at 300 °C, 400 °C, 500 °C and 600 °C are 0.20, 0.25, 0.31 and 0.33, respectively. This indicates, that the films carry a high degree of the B2 structure, whereas the decrease of the disorder on the Co sites is associated with an increasing substrate temperature T_s. This data agrees with the measurements performed on $Co_2Cr_{0.6}Fe_{0.4}Al$ thin films shown in Ref. [170], although there the order was achieved by a post annealing of the films.

Fig. 5.13(a) shows the X-ray reflectivity (XRR) measurement for the CCA thin film deposited at RT (red) and T_s = 400 °C (black). Theoretical details of the XRR method can be found in Ref. [173]. The open circles represent the raw data, whereas the solid lines were obtained from a fitting procedure using the Parratt algorithm as implemented in the *LSFIT* [174] code. For the sample prepared at RT no oscillations could be observed, which is accompanied by a strong decrease of the reflected intensity with the angle Θ, indicating a film surface with a high degree of roughness. On the contrary, periodic oscillations were measured for the

film deposited at a constant substrate temperature. This result is attributed to a well-defined film with a flat surface and confirms the epitaxial growth as shown in the previous XRD and LEED data. For this film a roughness value of 0.8 nm and a thickness value of $d = 187$ Å was determined. This result confirms the growth rate of 0.5 Å/s obtained with the quartz monitor, see paragraph 3.1.1. In Fig. 5.13(b) the corresponding electron density profiles ρ/ρ_{MgO} of both samples are shown, whereas the $z = 0$ Å position is related to the interface between the CCA film and the MgO(001) substrate. The sharp step around 200 Å indicates the flat surface of the CCA thin film structure deposited at $T_s = 400$ °C. Moreover, the interface region around $z = 0$ Å is well defined. The RT sample, however, shows a rather undefined density profile most likely related to an island growth.

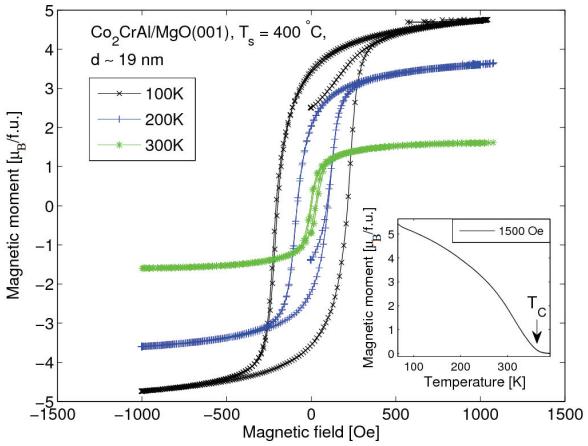

Figure 5.14: *Magnetization hysteresis loops of an epitaxial $Co_2CrAl/MgO(001)$ thin film (deposited at $T_s = 400$ °C) measured at 100, 200 and 300 K. The inset shows the temperature dependence of the magnetic moment at applied field of $H = 1500$ Oe.*

With the aim to perform spin-resolved photoemission experiments, next the magnetic properties were investigated by using an external Quantum Design vibrating sample magnetometer with a standard liquid Helium cooling system. The magnetization (M) measurements were performed at the PGI-6. Fig. 5.14 shows the hysteresis loops of a $B2$-ordered CCA thin film recorded at sample temperatures of 100, 200 and 300 K, with the magnetic moment m plotted as a function of the external magnetic field H. The magnetic field was applied in the plane of the film along

the [001] crystallographic axis. As can be seen, the sample exhibited a soft ferromagnetic behaviour with a clear increase of the coercivity and the magnetic moment after cooling below the room temperature. At 300 K the hysteresis curve shows a coercive field of $H_c \approx 40$ Oe and a saturated magnetic moment of $m_s \approx 1.6\ \mu_B$, which is reduced from the calculated bulk value of 2.96 μ_B expected for an ideal $L2_1$-ordered phase reported in Ref. [15]. Around 100 K, values of $H_c \approx 410$ Oe and $m_s \approx 4.7\ \mu_B$ were obtained. The Curie temperature T_C was measured after cooling the sample at $H = 1500$ Oe and heating it from 50 K to 390 K, see inset of Fig. 5.14. Its value of about 360 K is close to the value of 340 K reported in Ref. [175].

5.4.2 Spin- and angle-resolved valence band photoemission from Co_2CrAl thin films

The epitaxially grown CCA/MgO(001) thin films prepared by the optimized recipe were subsequently transferred without air exposure to the photoemission chamber at beamline 5. Fig. 5.15(a) shows the experimental valence band structure of a CCA thin film, which was deposited at $T_s = 400$ °C, measured in normal emission at $h\nu = 54$ eV. Moreover, the calculated total and partial DOS are plotted, which were convoluted by a Gaussian function accounting for the room temperature broadening of $\Delta E = 100$ meV. The two distinct experimental features between 0 and 2 eV binding energy are reproduced in the theoretical DOS. The main peak at $E_B \sim 1$ eV is dominated by Co $3d$ orbital contribution while the shoulder at $E_B \sim 0.15$ eV is mainly attributed to the Cr $3d$ orbital. Although the theory reproduces the experimental curve, the small discrepancy can be related to the limitations of the DFT GGA method such as electron-electron correlation effects [176] or to the so-called final state effects in photoemission [177].

In Fig. 5.15(b) the off-normal photoemission data shows the momentum dependence of the valence-band peaks indicating dispersive features which can be interpreted in terms of the bulk band mapping, whereas the spectral weight might also be influenced by significant contributions from the surface states. The spectra were measured with an angular step of $d\vartheta = 5°$ at $h\nu = 54$ eV. According to the sample orientation shown in Fig. 5.8, the spectra probe approximately the [110]-direction along the extended $\Gamma - K - X$ path within the reciprocal space. Fig. 5.16 displays the calculated spin-resolved electronic band structure of the majority and minority

spin-states of CCA with respect to the contributions of the Co and Cr *3d* orbitals. The mapped dispersion around 1 eV binding energy can therefore be explained by the dominating minority spin band simulated for the Co *3d* orbital, while the mapping around 0.15 eV binding energy agrees well with the spin-up contribution of the Cr *3d* orbital near the Fermi level.

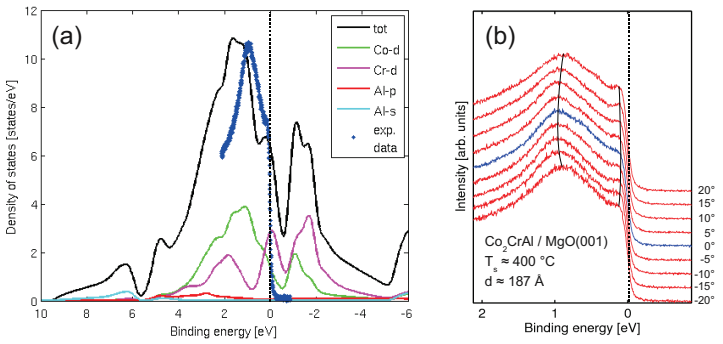

Figure 5.15: *(a) Comparison between experimental photoemission valence band data (blue dotted curve) and calculated spin-integrated total and partial DOS for Co_2CrAl. (b) Series of EDCs along the bulk $\Gamma - K - X$ direction taken at $\sim$ 200 K. The dispersive nature is indicated by the guide lines (black). The dashed lines represent the Fermi level at $E_B = 0$ eV.*

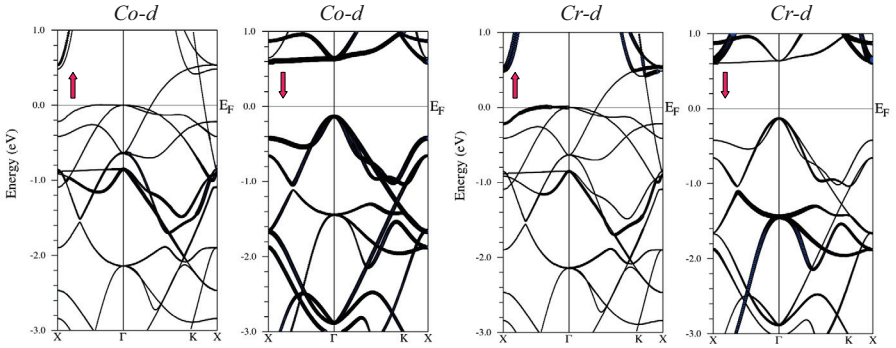

Figure 5.16: *Calculated spin-polarized bulk band structure of the Co_2CrAl compound for Co and Cr d-orbital contributions. The size of the symbols reflects the d character of the eigenvalues.*

Moreover, the CCA thin films were studied by means of spin-resolved photoemission spectroscopy. The spin-polarized spectra were measured in remanence using a photon energy of $h\nu = 24$ eV. Due to a relatively low Curie temperature close to the room temperature as shown in Fig. 5.14, the samples were cooled by liquid nitrogen. In order to remove polarimeter related asymmetries, the magnetization direction was reversed during the data acquisition. The experimental results are shown in Fig. 5.17. In the *in-plane* direction a weak spin polarization signal was found around 0.8 eV binding energy, which can be attributed to the Co 3*d* spin-down states in terms of the calculated bulk band structure shown in Fig. 5.16. However, the scatter of the experimental data does not permit a conclusion on the half-metallic behaviour, which is predicted to occur in the range between 0 and 0.1 eV. The quality of the photoemission data needs to be improved. In this context, a further evaluation of growth parameters, target stoichiometry and magnetic properties is mandatory in order to proof the half-metallic properties of the Co_2CrAl Heusler alloy.

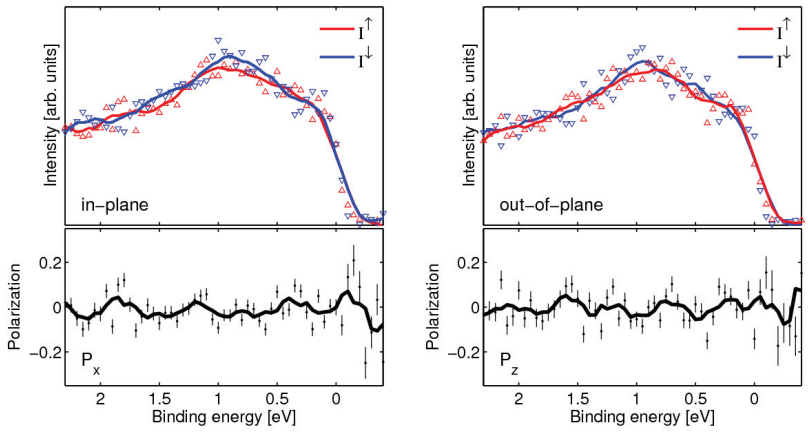

Figure 5.17: *Experimental spin-polarized spectra obtained from an epitaxially grown CCA/MgO(001) thin film for the in-plane (left) and out-of-plane (right) spin vector components. Red and blue solid lines are related to smoothed $I^{\uparrow}$ and $I^{\downarrow}$ intensities. The related spin polarizations P_x and P_z (black dots) are shown below the corresponding intensity plots, whereas standard deviations are given by vertical error bars. The black curves are guides to the eye.*

5.5 Conclusions

In conclusion, the structural and spectroscopic characterization proves the successful *in situ* epitaxial growth of the CCA films in the full-Heusler half-metallic B2 phase. The optimized growth mode was achieved by the magnetron sputtering method using a stoichiometric target under the strict UHV conditions. The initial *in situ* structural and chemical analysis was performed using *in situ* LEED and AES methods. Furthermore, the influence of substrate and post-annealing temperatures on the crystalline ordering was studied by XRD measurements. With an increasing substrate temperatures an increase of the order parameter s_{B2} was observed. The results show, that epitaxial thin films possessing a high B2 order can be obtained for substrate temperatures $T_s > 300$ °C. The presented XRD and XRR measurements on samples prepared at different conditions revealed the experimental growth parameters for ordered flat thin film structures. The application of a substrate temperature T_s significantly increased also the surface quality resulting in crystalline surface structures as confirmed by the LEED patterns. We find, that a combination of a low growth rate and the application of a constant substrate temperature during the sputter process improve the epitaxial growth in such a way, that surface roughness and structural disorder are decreased. Furthermore, magnetization measurements confirmed the ferromagnetic behaviour of the prepared thin films. Valence-band photoemission data taken at normal emission were compared to dedicated DOS calculations which allowed the interpretation of the observed features. Moreover, the quality of the thin films allowed angle-resolved photoemission measurements on freshly prepared specimens. The observed dispersive energy bands were discussed by orbital-resolved bulk band structure calculations. The occurrence of the measured dispersion curves demonstrated the quality of the successfully prepared epitaxial thin films.

6 Summary and Outlook

Topological insulators and half-metallic Heusler alloys are two important classes of materials currently under investigation for use in future spintronic devices [178]. In particular, they are potential candidates for achieving and injecting highly polarized spin currents at room temperature. The main emphasis of the thesis is on the electronic and structural properties of 3D TIs Bi_2Te_3 and Sb_2Te_3 compounds as well as on the half-metallic Co_2CrAl Heusler alloy. The focus was on the properties of thin films since those are the most relevant in case of future industrial applications.

The electronic properties of MBE-grown Bi_2Te_3/Si(111) and Sb_2Te_3/Si(111) epilayers were investigated by surface sensitive angle- and spin-resolved photoemission measurements. The samples were sputtered and annealed (Bi_2Te_3) or annealed only (Sb_2Te_3) after introducing to the photoemission system vacuum. High resolution ARPES studies confirmed the TI properties of the films by showing clear Dirac cone surface states within the fundamental gap for both thin film systems. In addition it was shown, that the spectral weight of Bi_2Te_3 and Sb_2Te_3 TIs is dominated by a set of strongly dispersing bands between 1 and 3.5 eV binding energy. These measurements were performed at the PGI-6 using the laboratory based photoemission system.

The combined spin-resolved measurements carried out at the synchrotron radiation facility DELTA revealed clear spin reversals of the *in-plane* vector component on selected opposite $\boldsymbol{k}$-points for both TI material systems. These results are related to the helical nature of the surface states, which up to now was only reported for states near the Fermi level below binding energies of $E_B < 1$ eV for the Dirac cone state [3, 4, 179]. In addition, spin-polarized photoemission measurements on Bi_2Te_3 thin films revealed an *out-of-plane* spin polarization related to the hexagonal nature of the Fermi surface.

This thesis presents the first detailed analysis on the spin polarization behaviour of epitaxial thin films of the narrow gap semiconductor Bi_2Te_3. The analysis of

the experimental results was performed with the aid of dedicated theoretical *ab initio* thin film calculations obtained within the DFT scheme, which have revealed that the Dirac cone related electron density is delocalized over the first quintuple layer, whereas the related spin density shows a remarkable spin polarization vector orientation changes within subsequent layers. As an extension to the previous work reported in Refs. [6–8] we have simulated the expected spin polarization taking into account the photoemission spectral weight, and found approx. 45% spin polarization in the Dirac cone state, in full agreement with the experiment.

Our finding suggests, that the future research on 3D TIs should focus not only on achieving the insulating state in the bulk, but also on increasing the spin polarization of the Dirac cone state. One way to achieve this might be by the deposition of thin layers of selected elements. It was recently shown that a Bi-bilayer on Bi_2Te_3 induces higher localization of the Dirac cone state [180], which suggests that the spin polarization in such states might be increased. Moreover, the electron doping of the Sb_2Te_3 surface, for example, by the deposition of the submonolayers of Caesium (Cs) will allow the control of the Dirac cone position with respect to the Fermi level. Furthermore, it is important to perform detailed spin-polarized band mapping studies at various photon energies using the synchrotron based photoemission system, which will allow one to vary the surface sensitivity and matrix elements. Such measurements will allow to reveal the layer-dependent spin structure of the Dirac cone states.

The second part of this thesis was devoted to the exploration of the electronic structure of thin Heusler alloy films. Since photoemission spectroscopy is a surface sensitive method and Heusler alloys were proposed to be sensitive to oxidation, it is therefore mandatory to produce clean and well-ordered surfaces *in situ*. For this purpose, ternary Co_2CrAl thin films were grown in a new sputter deposition chamber commissioned at the beamline 5. This fully UHV compatible system comprising a DC magnetron sputter source, a heatable sample stage and a quartz crystal thickness monitor was connected to the existing photoemission and a second sample preparation chamber. The successful *in situ* growth of clean epitaxial Heusler alloy Co_2CrAl thin films on MgO(001) substrates was confirmed by using surface sensitive AES and LEED techniques. The bulk related structural properties were measured using the X-ray diffraction method, which revealed a highly $B2$ ordered Heusler structure for films deposited at substrate temperatures higher than 300 °C. The

film thickness and roughness was obtained from X-ray reflectivity measurements. First angle-resolved photoemission results showed dispersion features within the valence band confirming the presence of a well-defined electronic structure. In order to improve the quality of the thin films and the resulting spin-polarized data, further growth condition studies are mandatory. In addition, it is important to make use of the newly developed FERRUM spin detector (see paragraph 3.2).

I have optimized growth conditions for a $B2$ ordered Co_2CrAl/MgO(001) Heusler alloy. In order to provide a complete characterization of the prepared films, further *in situ* and *ex situ* studies will be necessary. For example, it is important to study the influence of different growth conditions on the ferromagnetic properties using either the existing *in situ* based MOKE (magneto-optic Kerr effect) experiment, which is installed at the beamline 5, or an external superconducting quantum interference device (SQUID). In addition, investigations of the influence of the sputter target stoichiometry on surface and bulk properties is a promising path forward towards half-metallic Heusler alloys.

On the experimental side, the developed sputtering system opens up new possibilities for the design of alternative sample systems, such as various Heusler phases or similar materials exhibiting the half-metallic properties. It will also be possible to deposit topological insulating thin films from commercial stoichiometric Bi_2Te_3, Bi_2Se_3 or Bi_2Se_3 sputter targets [70]. Due to the direct connection to the photoemission and surface analysis chamber, the freshly deposited samples will not be exposed to air, therefore, it will not be necessary to clean the surfaces by invasive methods such as sputter, anneal or cleavage, thus, preserving the pristine surface stoichiometry and roughness. Following spin- and angle-resolved photoemission studies will give more insight into the complex electronic structure of high-quality TI thin films.

Furthermore, a new spin-sensitive detection system implemented at the laboratory based photoemission system is currently being commissioned by the PGI-6 group, which will open the possibility to reveal high-resolution details of the spin-texture on single crystal and thin film 3D TIs structures. Besides the surface related electronic properties, it is also important to probe the details of the bulk band structure by means of a synchrotron based hard X-ray angle-resolved photoemission spectroscopy (HARPES) experiment [181]. High photon energies between 2.0 and 6.0 keV increase the inelastic mean free path of the electrons and therefore allow to study the magnitude and character of the TI SO bulk band gap.

Bibliography

[1] H. Zhang, C. Liu, X. Qi, X. Dai, Z. Fang, and S. Zhang, Nat. Phys. **5**, 438 (2009).

[2] L. A. Wray, S.-Y. Xu, Y. Xia, D. Hsieh, A. V. Fedorov, Y. S. Hor, R. J. Cava, A. Bansil, H. Lin, and M. Z. Hasan, Nat. Phys. **7**, 32 (2011).

[3] Z.-H. Pan, E. Vescovo, A. V. Fedorov, D. Gardner, Y. S. Lee, S. Chu, G. D. Gu, and T. Valla, Phys. Rev. Lett. **106**, 257004 (2011).

[4] S. Souma, K. Kosaka, T. Sato, M. Komatsu, A. Takayama, T. Takahashi, M. Kriener, K. Segawa, and Y. Ando, Phys. Rev. Lett. **106**, 216803 (2011).

[5] C. Pauly, G. Bihlmayer, M. Liebmann, M. Grob, A. Georgi, D. Subramaniam, M. R. Scholz, J. Sánchez-Barriga, A. Varykhalov, S. Blügel, O. Rader, and M. Morgenstern, arXiv:1201.4323v1 (2012).

[6] O. V. Yazyev, J. E. Moore, and S. G. Louie, Phys. Rev. Lett. **105**, 266806 (2010).

[7] S. V. Eremeev, G. Landolt, T. V. Menshchikova, B. Slomski, Y. M. Koroteev, Z. S. Aliev, M. B. Babanly, J. Henk, A. Ernst, L. Patthey, A. Eich, A. A. Khajetoorians, J. Hagemeister, O. Pietzsch, J. Wiebe, R. Wiesendanger, P. M. Echenique, S. S. Tsirkin, I. R. Amiraslanov, J. H. Dil, and E. V. Chulkov, Nat. Commun. **3**, 635 (2012).

[8] J. Henk, A. Ernst, S. V. Eremeev, E. V. Chulkov, I. V. Maznichenko, and I. Mertig, Phys. Rev. Lett. **108**, 206801 (2012).

[9] H. Lin, L. A. Wray, Y. Xia, S. Xu, S. Jia, R. J. Cava, A. Bansil, and M. Z. Hasan, Nat. Mater. **9**, 546 (2010).

[10] W. Al-Sawai, H. Lin, R. S. Markiewicz, L. A. Wray, Y. Xia, S.-Y. Xu, M. Z. Hasan, and A. Bansil, Phys. Rev. B **82**, 125208 (2010).

[11] S. Chadov, X. Qi, J. Kübler, G. H. Fecher, C. Felser, and S. C. Zhang, Nat. Mater. **9**, 541 (2010).

[12] C. Liu, Y. Lee, T. Kondo, E. D. Mun, M. Caudle, B. N. Harmon, S. L. Bud'ko, P. C. Canfield, and A. Kaminski, Phys. Rev. B **83**, 205133 (2011).

[13] I. Galanakis, P. H. Dederichs, and N. Papanikolaou, Phys. Rev. B **66**, 174429 (2002).

[14] I. Galanakis, P. Mavropoulos, and P. H. Dederichs, Journal of Physics D: Applied Physics **39**, 765 (2006).

[15] I. Galanakis, Journal of Physics: Condensed Matter **14**, 6329 (2002).

[16] Y. Miura, K. Nagao, and M. Shirai, Phys. Rev. B **69**, 144413 (2004).

[17] T. M. Nakatani, A. Rajanikanth, Z. Gercsi, Y. K. Takahashi, K. Inomata, and K. Hono, Journal of Applied Physics **102**, 033916 (2007).

[18] S. Huefner, *Photoelectron Spectroscopy, Principle and Applications* (Springer, Berlin, 2003), Vol. 3rd edition.

[19] C. M. Schneider, *Lecture Manuscripts of the 38th Spring School: Probing the Nanoworld* (Schriften des Froschungszentrums Jülich, Jülich, 2007), p. 6.9.

[20] C. N. Berglund and W. E. Spicer, Phys. Rev. **136**, A1030 (1964).

[21] W. Schattke, *Solid-State Photoemission and Related Methods: Theory and Experiment* (John Wiley & Sons, Weinheim, 2003).

[22] P. D. Johnson, Reports on Progress in Physics **60**, 1217 (1997).

[23] A. Damascelli, Z. Hussain, and Z.-X. Shen, Rev. Mod. Phys. **75**, 473 (2003).

[24] C. M. Schneider, *Photoelectron Spectroscopy* (Schriften des Froschungszentrums Jülich, Jülich, 2009), Vol. IFF Spring School 2009.

[25] M. P. Seah and W. A. Dench, Surf. Interface Anal. **1**, 2 (1979).

[26] A. Damascelli, Physica Scripta **2004**, 61 (2004).

[27] V. N. Strocov, H. I. Starnberg, P. O. Nilsson, H. E. Brauer, and L. J. Holleboom, Phys. Rev. Lett. **79**, 467 (1997).

[28] K. Baberschke and M. Donath, *Band-Ferromagnetism: Ground-State and Finite-Temperature Phenomena* (Springer, Berlin, Heidelberg, New York, 2001), p. 343 ff.

[29] W. Schattke, Progress in Surface Science **54**, 211 (1997).

[30] J. Kessler, *Polarized Electrons* (Springer Verlag, Berlin Heidelberg New York, 1976).

[31] W. Kuch and C. M. Schneider, Reports on Progress in Physics **64**, 147 (2001).

[32] C. M. Schneider and J. Kirschner, Critical Reviews in Solid State and Materials Sciences **20**, 179 (1995).

[33] J. Osterwalder, Journal of Physics: Condensed Matter **24**, 171001 (2012).

[34] U. Heinzmann and J. H. Dil, Journal of Physics: Condensed Matter **24**, 173001 (2012).

[35] C. Schneider, J. de Miguel, P. Bressler, P. Schuster, R. Miranda, and J. Kirschner, Journal of Electron Spectroscopy and Related Phenomena **51**, 263 (1990).

[36] W. Shockley, Phys. Rev. **56**, 317 (1939).

[37] F. Forstmann and J. B. Pendry, Zeitschrift für Physik A Hadrons and Nuclei **235**, 75 (1970), 10.1007/BF01399759.

[38] F. Forstmann, Zeitschrift für Physik A Hadrons and Nuclei **235**, 69 (1970), 10.1007/BF01399758.

[39] J. Pendry and S. Gurman, Surface Science **49**, 87 (1975).

[40] R. Winkler, *Spin-Orbit Coupling Effects in Two-Dimensional Electron and Hole Systems* (Springer, Berlin, Heidelberg, New York, 2003), Vol. 191, pp. 77–79.

[41] G. Bihlmayer, *Electronic Oxides: Correlation Phenomena, Exotic Phases, and Novel Functionalities* (Schriften des Forschungszentrums Jülich, Jülich, 2010), Vol. 41st IFF Spring School.

[42] L. Petersen and P. Hedegård, Surface Science **459**, 49 (2000).

[43] J. H. Dil, Journal of Physics: Condensed Matter **21**, 403001 (2009).

[44] S. LaShell, B. A. McDougall, and E. Jensen, Phys. Rev. Lett. **77**, 3419 (1996).

[45] M. Hoesch, M. Muntwiler, V. N. Petrov, M. Hengsberger, L. Patthey, M. Shi, M. Falub, T. Greber, and J. Osterwalder, Phys. Rev. B **69**, 241401 (2004).

[46] Y. M. Koroteev, G. Bihlmayer, J. E. Gayone, E. V. Chulkov, S. Blügel, P. M. Echenique, and P. Hofmann, Phys. Rev. Lett. **93**, 046403 (2004).

[47] T. Hirahara, K. Miyamoto, I. Matsuda, T. Kadono, A. Kimura, T. Nagao, G. Bihlmayer, E. V. Chulkov, S. Qiao, K. Shimada, H. Namatame, M. Taniguchi, and S. Hasegawa, Phys. Rev. B **76**, 153305 (2007).

[48] A. Kimura, E. E. Krasovskii, R. Nishimura, K. Miyamoto, T. Kadono, K. Kanomaru, E. V. Chulkov, G. Bihlmayer, K. Shimada, H. Namatame, and M. Taniguchi, Phys. Rev. Lett. **105**, 076804 (2010).

[49] K. Sugawara, T. Sato, S. Souma, T. Takahashi, M. Arai, and T. Sasaki, Phys. Rev. Lett. **96**, 046411 (2006).

[50] C. R. Ast, J. Henk, A. Ernst, L. Moreschini, M. C. Falub, D. Pacilé, P. Bruno, K. Kern, and M. Grioni, Phys. Rev. Lett. **98**, 186807 (2007).

[51] H. Bentmann, F. Forster, G. Bihlmayer, E. V. Chulkov, L. Moreschini, M. Grioni, and F. Reinert, Europhysics Letters **87**, 37003 (2009).

[52] J. Moore, Nature Physics **5**, (2009).

[53] P. Blaha, K. Schwarz, G. Madsen, D. Kvasnicka, and J. Luitz, *WIEN2k, An Augmented Plane Wave + Local Orbitals Program for Calculating Crystal Properties* (Techn. Universität Wien, Austria, 2001).

[54] http://www.flapw.de.

[55] J. C. Slater, Phys. Rev. **36**, 57 (1930).

[56] J. C. Slater, Phys. Rev. **34**, 1293 (1929).

[57] P. Hohenberg and W. Kohn, Phys. Rev. **136**, B864 (1964).

[58] G. Bihlmayer, *Magnetism in Density Functional Theory*, Vol. 37 of *IFF Spring School* (Schriften des Forschungszentrums Jülich, Jülich, 2006).

[59] W. Kohn and L. J. Sham, Phys. Rev. **140**, A1133 (1965).

[60] J. M. Thijssen, *Computational Physics*, *2* (Cambridge University Press, New York, 2007), pp. 95–96.

[61] D. M. Ceperley and B. J. Alder, Phys. Rev. Lett. **45**, 566 (1980).

[62] J. P. Perdew and A. Zunger, Phys. Rev. B **23**, 5048 (1981).

[63] V. I. Anisimov, J. Zaanen, and O. K. Andersen, Phys. Rev. B **44**, 943 (1991).

[64] V. I. Anisimov, F. Aryasetiawan, and A. I. Lichtenstein, Journal of Physics: Condensed Matter **9**, 767 (1997).

[65] E. A. Jorge, *PhD thesis: Band structure of Heusler Compounds studied by Photoemission and Tunneling Spectroscopy* (Johannes Gutenberg-Universität Mainz, Mainz, 2011).

[66] H. Petersen, C. Jung, C. Hellwig, W. B. Peatman, and W. Gudat, Review of Scientific Instruments **66**, 1 (1995).

[67] S. Cramm, IFF Jahresbericht (1999).

[68] L. Grill, Ph.D. thesis, Karl-Franzens-Universität Graz, 2001.

[69] L. E. Davis, *Handbook of Auger Electron Spectroscopy* (Physical Electronics Devision, Minnesota, 1972), Vol. 2, pp. 1–2.

[70] J. Tan, K. Kalantar-zadeh, W. Wlodarski, S. Bhargava, D. Akolekar, A. Holland, and G. Rosengarten, Smart Sensors, Actuators, and MEMS II **5836**, 711 (2005).

[71] J. Marshall, Method and apparatus for linear magnetron sputtering, 1992, patent.

[72] http://www.agsemiconductor.com/SputterDeposition.php.

[73] J. Kirschner and R. Feder, Phys. Rev. Lett. **42**, 1008 (1979).

[74] D. Yu, C. Math, M. Meier, M. Escher, G. Rangelov, and M. Donath, Surface Science **601**, 5803 (2007).

[75] L. Plucinski, A. Oelsner, F. Matthes, and C. Schneider, Journal of Electron Spectroscopy and Related Phenomena **181**, 215 (2010).

[76] *An introduction to SES 2002 analyser*, 2001.

[77] *Delayline Detector DLD-3030*, Surface Concept GmbH, 2008.

[78] *High Voltage SPLEED Detector/Delayline Detector Combination*, Surface Concept GmbH, 2010.

[79] *Focus SPLEED, Technical Reference Manual*, 1.1 ed., 2012.

[80] Y. Zhu, *Modern Techniques For Characterizing Magnetic Materials* (Kluwer Academic Publishers, Springer, United States of America, 2005), p. 334.

[81] J. Osterwalder, *Spin-Polarized Photoemission* (Springer, Berlin, Heidelberg, 2006), No. 697, pp. 95–120.

[82] S. Suga, A. Sekiyama, G. Funabashi, J. Yamaguchi, M. Kimura, M. Tsujibayashi, T. Uyama, H. Sugiyama, Y. Tomida, G. Kuwahara, S. Kitayama, K. Fukushima, K. Kimura, T. Yokoi, K. Murakami, H. Fujiwara, Y. Saitoh, L. Plucinski, and C. M. Schneider, Rev. Sci. Instrum. **81**, 105111 (2010).

[83] Y. Xia, D. Qian, D. Hsieh, L. Wray, A. Pal, H. Lin, A. Bansil, D. Grander, Y. S. Hor, R. J. Cava, and M. Z. Hasan, Nat. Phys. **5**, 398 (2009).

[84] M. Escher, N. B. Weber, M. Merkel, L. Plucinski, and C. M. Schneider, e-Journal of Surface Science and Nanotechnology **9**, 340 (2011).

[85] X.-L. Qi and S.-C. Zhang, Rev. Mod. Phys. **83**, 1057 (2011).

[86] L. Landau, Phys. Z. Sowjetunion **11**, 26 (1937).

[87] K. v. Klitzing, G. Dorda, and M. Pepper, Phys. Rev. Lett. **45**, 494 (1980).

[88] von Klitzing K., Philos Transact A Math Phys Eng Sci. **363**, 1834 (2005).

[89] M. Z. Hasan and C. L. Kane, Rev. Mod. Phys. **82**, 3045 (2010).

[90] D. J. Thouless, M. Kohmoto, M. P. Nightingale, and M. den Nijs, Phys. Rev. Lett. **49**, 405 (1982).

[91] S. Murakami, N. Nagaosa, and S.-C. Zhang, Science **301**, 1348 (2003).

[92] J. Sinova, D. Culcer, Q. Niu, N. A. Sinitsyn, T. Jungwirth, and A. H. MacDonald, Phys. Rev. Lett. **92**, 126603 (2004).

[93] Y. K. Kato, R. C. Myers, A. C. Gossard, and D. D. Awschalom, Science **306**, 1910 (2004).

[94] J. Wunderlich, B. Kaestner, J. Sinova, and T. Jungwirth, Phys. Rev. Lett. **94**, 047204 (2005).

[95] C. L. Kane and E. J. Mele, Phys. Rev. Lett. **95**, 146802 (2005).

[96] Y. Yao, F. Ye, X.-L. Qi, S.-C. Zhang, and Z. Fang, Phys. Rev. B **75**, 041401 (2007).

[97] H. Min, J. E. Hill, N. A. Sinitsyn, B. R. Sahu, L. Kleinman, and A. H. MacDonald, Phys. Rev. B **74**, 165310 (2006).

[98] B. A. Bernevig, T. L. Hughes, and S.-C. Zhang, Science **314**, 1757 (2006).

[99] M. König, H. Buhmann, L. W. Molenkamp, T. Hughes, C.-X. Liu, X.-L. Qi, and S.-C. Zhang, Journal of the Physical Society of Japan **77**, 031007 (2008).

[100] L. Fu and C. L. Kane, Phys. Rev. B **76**, 045302 (2007).

[101] D. Hsieh, D. Qian, L. Wray, Y. Xia, Y. S. Hor, R. J. Cava, and M. Z. Hasan, Nature Letters **452**, 970 (2008).

[102] D. Hsieh, Y. Xia, L. Wray, D. Qian, A. Pal, J. H. Dil, J. Osterwalder, F. Meier, G. Bihlmayer, C. L. Kane, Y. S. Hor, R. J. Cava, and M. Z. Hasan, Science **323**, 919 (2009).

[103] M. Z. Hasan and J. E. Moore, Annual Review of Condensed Matter Physics **2**, 55 (2010).

[104] C. L. Kane and E. J. Mele, Phys. Rev. Lett. **95**, 226801 (2005).

[105] L. Fu, C. L. Kane, and E. J. Mele, Phys. Rev. Lett. **98**, 106803 (2007).

[106] Y. L. Chen, J. G. Analytis, J.-H. Chu, Z. K. Liu, S.-K. Mo, X. L. Qi, H. J. Zhang, D. H. Lu, X. Dai, Z. Fang, S. C. Zhang, I. R. Fisher, Z. Hussain, and Z.-X. Shen, Science **325**, 178 (2009).

[107] D. Hsieh, Y. Xia, D. Qian, L. Wray, F. Meier, J. H. Dil, J. Osterwalder, L. Patthey, A. V. Fedorov, H. Lin, A. Bansil, D. Grauer, Y. S. Hor, R. J. Cava, and M. Z. Hasan, Phys. Rev. Lett. **103**, 146401 (2009).

[108] K. Kuroda, M. Arita, K. Miyamoto, M. Ye, J. Jiang, A. Kimura, E. E. Krasovskii, E. V. Chulkov, H. Iwasawa, T. Okuda, K. Shimada, Y. Ueda, H. Namatame, and M. Taniguchi, Phys. Rev. Lett. **105**, 076802 (2010).

[109] D. Teweldebrhan, V. Goyal, M. Rahman, and A. A. Balandin, Applied Physics Letters **96**, 053107 (2010).

[110] S. K. Mishra, S. Satpathy, and O. Jepsen, Journal of Physics: Condensed Matter **9**, 461 (1997).

[111] O. Madelung, U. Roessler, and M. Schulz, SpringerMaterials - The Landolt-Boernstein Database **41C**, (1998).

[112] J. Zhang, Z. Peng, A. Soni, Y. Zhao, Y. Xiong, B. Peng, J. Wang, M. S. Dresselhaus, and Q. Xiong, Nano Letters **11**, 2407 (2011).

[113] O. Tereshchenko, K. Kokh, V. Atuchin, K. Romanyuk, S. Makarenko, V. Golyashov, A. Kozhukhov, I. Prosvirin, and A. Shklyaev, JETP Letters **94**, 465 (2011).

[114] Y. Kim, A. DiVenere, G. K. L. Wong, J. B. Ketterson, S. Cho, and J. R. Meyer, Journal of Applied Physics **91**, 715 (2002).

[115] J. Henk, M. Flieger, I. V. Maznichenko, I. Mertig, A. Ernst, S. V. Eremeev, and E. V. Chulkov, Phys. Rev. Lett. **109**, 076801 (2012).

[116] Y. L. Chen, J.-H. Chu, J. G. Analytis, Z. K. Liu, K. Igarashi, H.-H. Kuo, X. L. Qi, S. K. Mo, R. G. Moore, D. H. Lu, M. Hashimoto, T. Sasagawa, S. C. Zhang, I. R. Fisher, Z. Hussain, and Z. X. Shen, Science **329**, 659 (2010).

[117] D. Pesin and A. H. MacDonald, Nature Materials **11**, 409 (2012).

[118] A. H. Castro Neto, F. Guinea, N. M. R. Peres, K. S. Novoselov, and A. K. Geim, Rev. Mod. Phys. **81**, 109 (2009).

[119] S.-Q. Shen, W.-Y. Shan, and H.-Z. Lu, SPIN **1**, pp. 33 (2011).

[120] E. Rotenberg, Nat. Phys. **7**, 8 (2011).

[121] J. E. Moore and L. Balents, Phys. Rev. B **75**, 121306 (2007).

[122] J. C. Y. Teo, L. Fu, and C. L. Kane, Phys. Rev. B **78**, 045426 (2008).

[123] L. Fu, Phys. Rev. Lett. **103**, 266801 (2009).

[124] C. Jozwiak, Y. L. Chen, A. V. Fedorov, J. G. Analytis, C. R. Rotundu, A. K. Schmid, J. D. Denlinger, Y.-D. Chuang, D.-H. Lee, I. R. Fisher, R. J. Birgeneau, Z.-X. Shen, Z. Hussain, and A. Lanzara, Phys. Rev. B **84**, 165113 (2011).

[125] S.-Y. Xu, L. A. Wray, Y. Xia, F. von Rohr, Y. S. Hor, J. H. D. anfd anfd, F. Meier, B. Slomski, J. Osterwalder, M. Neupane, H. Lin, A. Bansil, A. Fedorov, R. J. Cava, and M. Z. Hasan, arXiv:1101.3985v1 (2011).

[126] J. P. Perdew, K. Burke, and M. Ernzerhof, Phys. Rev. Lett. **77**, 3865 (1996).

[127] W. Zhang, R. Yu, H.-J. Zhang, X. Dai, and Z. Fang, New Journal of Physics **12**, 065013 (2010).

[128] K. Park, J. J. Heremans, V. W. Scarola, and D. Minic, Phys. Rev. Lett. **105**, 186801 (2010).

[129] G. Wang and T. Cagin, Applied Physics Letters **89**, 152101 (2006).

[130] C. Li, A. J. Freeman, H. J. F. Jansen, and C. L. Fu, Phys. Rev. B **42**, 5433 (1990).

[131] J. Krumrain, G. Mussler, S. Borisova, T. Stoica, L. Plucinski, C. Schneider, and D. Gruetzmacher, Journal of Crystal Growth **324**, 115 (2011).

[132] L. Plucinski, G. Mussler, J. Krumrain, A. Herdt, S. Suga, D. Grützmacher, and C. M. Schneider, Applied Physics Letters **98**, 222503 (2011).

[133] G. Mussler (private communication).

[134] H.-J. Noh, H. Koh, S.-J. Oh, J.-H. Park, H.-D. Kim, J. D. Rameau, T. Valla, T. E. Kidd, P. D. Johnson, Y. Hu, and Q. Li, EPL (Europhysics Letters) **81**, 57006 (2008).

[135] Y.-Y. Li, G. Wang, X.-G. Zhu, M.-H. Liu, C. Ye, X. Chen, Y.-Y. Wang, K. He, L.-L. Wang, X.-C. Ma, H.-J. Zhang, X. Dai, Z. Fang, X.-C. Xie, Y. Liu, X.-L. Qi, J.-F. Jia, S.-C. Zhang, and Q.-K. Xue, Advanced Materials **22**, 4002 (2010).

[136] J. Zhang, C.-Z. Chang, Z. Zhang, J. Wen, and M. L. K. H. L. W. X. C. Q.-K. X. X. M. Y. W. Xiao Feng, Kang Li, Nat. Commun. **2**, 574 (2011).

[137] C. Chen, S. He, H. Weng, W. Zhang, L. Zhao, H. Liu, X. Jia, D. Mou, S. Liu, J. He, Y. Peng, Y. Feng, Z. Xie, G. L. X. Dong, J. Zhang, X. W. Q. Peng, Z. Wang, S. Zhang, F. Yang, C. Chen, Z. Xu, X. Dai, Z. Fang, and X. J. Zhou, Proceeding of the National Academy of Sciences of the United States of America (PNAS) **109**, 3694 (2012).

[138] H. D. Li, Z. Y. Wang, X. Kan, X. Guo, H. T. He, Z. Wang, J. N. Wang, T. L. Wong, N. Wang, and M. H. Xie, New Journal of Physics **12**, 103038 (2010).

[139] G. Wang, X. Zhu, J. Wen, X. Chen, K. He, L. Wang, X. Ma, Y. Liu, X. Dai, Z. Fang, J. Jia, and Q. Xue, Nano Research **3**, 874 (2010), 10.1007/s12274-010-0060-2.

[140] J. H. Dil, F. Meier, J. Lobo-Checa, L. Patthey, G. Bihlmayer, and J. Osterwalder, Phys. Rev. Lett. **101**, 266802 (2008).

[141] P. Roushan, J. Seo, C. V. Parker, Y. S. Hor, D. Hsieh, D. Qian, A. Richardella, M. Z. Hasan, R. J. Cava, and A. Yazdani, (2009).

[142] T. Zhang, P. Cheng, X. Chen, J.-F. Jia, X. Ma, K. He, L. Wang, H. Zhang, X. Dai, Z. Fang, X. Xie, and Q.-K. Xue, Phys. Rev. Lett. **103**, 266803 (2009).

[143] S. R. Park, W. S. Jung, C. Kim, D. J. Song, C. Kim, S. Kimura, K. D. Lee, and N. Hur, Phys. Rev. B **81**, 041405 (2010).

[144] T. Hanaguri, K. Igarashi, M. Kawamura, H. Takagi, and T. Sasagawa, Phys. Rev. B **82**, 081305 (2010).

[145] I. Galanakis, Journal of Physics: Condensed Matter **16**, 8007 (2004).

[146] I. Galanakis and P. H. Dederichs, *Half-metallic alloys: fundamentals and applications* (Springer, Berlin, Heidelberg, New York, 2005).

[147] Y. Liu, D. J. Sellmyer, and D. Shindo, *Handbook Of Advanced Magnetic Materials* (Springer, Berlin, Heidelberg, New York, 2005), Vol. 2, pp. 268–269.

[148] R. A. de Groot, F. M. Mueller, P. G. van Engen, and K. H. J. Buschow, Phys. Rev. Lett. **50**, 2024 (1983).

[149] J. Kübler, G. H. Fecher, and C. Felser, Phys. Rev. B **76**, 024414 (2007).

[150] M. N. Baibich, J. M. Broto, A. Fert, F. N. Van Dau, F. Petroff, P. Etienne, G. Creuzet, A. Friederich, and J. Chazelas, Phys. Rev. Lett. **61**, 2472 (1988).

[151] G. Binasch, P. Grünberg, F. Saurenbach, and W. Zinn, Phys. Rev. B **39**, 4828 (1989).

[152] J. S. Moodera and G. Mathon, Journal of Magnetism and Magnetic Materials **200**, 248 (1999).

[153] T. Shinjō, *Nanomagnetism and Spintronics* (Elsevier, Amsterdam, 2004).

[154] M. Julliere, Physics Letters A **54**, 225 (1975).

[155] Z. Gercsi, A. Rajanikanth, Y. K. Takahashi, K. Hono, M. Kikuchi, N. Tezuka, and K. Inomata, **89**, 082512 (2006).

[156] H. C. Kandpal, G. H. Fecher, C. Felser, and G. Schönhense, Phys. Rev. B **73**, 094422 (2006).

[157] W. H. Wang, M. Przybylski, W. Kuch, L. I. Chelaru, J. Wang, Y. F. Lu, J. Barthel, H. L. Meyerheim, and J. Kirschner, Phys. Rev. B **71**, 144416 (2005).

[158] J.-P. Wüstenberg, J. Fischer, C. Herbort, M. Jourdan, M. Aeschlimann, and M. Cinchetti, Journal of Physics D: Applied Physics **42**, 084016 (2009).

[159] M. Hahn, G. Schönhense, E. A. Jorge, and M. Jourdan, Applied Physics Letters **98**, 232503 (2011).

[160] B. Aktas and F. Mikailov, *Advances in Nanoscale Magnetism* (Springer, Berlin Heidelberg, 2008), Vol. Proceedings of the International Conference on Nanoscale Magnetism, pp. 21–22.

[161] E. Şaşioğlu, Ph.D. thesis, Martin-Luther-Universität Halle-Wittenberg, 2006.

[162] http://cst-www.nrl.navy.mil/bind/static/example7/fcczone.png.

[163] L. P. Bouckaert, R. Smoluchowski, and E. Wigner, Phys. Rev. **50**, 58 (1936).

[164] M. Zhang, Z. Liu, H. Hu, G. Liu, Y. Cui, J. Chen, G. Wu, X. Zhang, and G. Xiao, Journal of Magnetism and Magnetic Materials **277**, 130 (2004).

[165] G. H. Fecher, H. C. Kandpal, S. Wurmehl, J. Morais, H.-J. Lin, H.-J. Elmers, G. Schönhense, and C. Felser, Journal of Physics: Condensed Matter **17**, 7237 (2005).

[166] M. Ken-ichi, K. Takashi, M. Takao, U. Tetsuya, and Y. Masafumi, Journal of Crystal Growth **286**, 389 (2006).

[167] W. H. Zachariasen, *Theory of X-Ray Diffraction in Crystals* (Courier Dover Publications, New York, 2004).

[168] D. M. Jens Als-Nielsen, *Elements of Modern X-Ray Physics*, 2 ed. (John Wiley & Sons, United Kingdom, 2011).

[169] A. Conca, M. Jourdan, C. Herbort, and H. Adrian, Journal of Crystal Growth **299**, 299 (2007).

[170] C. Herbort, E. Arbelo, and M. Jourdan, Journal of Physics D: Applied Physics **42**, 084006 (2009).

[171] M. Cinchetti, J.-P. Wüstenberg, M. S. Albaneda, F. Steeb, A. Conca, M. Jourdan, and M. Aeschlimann, Journal of Physics D: Applied Physics **40**, 1544 (2007).

[172] http://www.bam.de/de/service/publikationen/powdercell.htm.

[173] M. Tolan, *X-ray Scattering from Soft Matter Thin Films* (Springer, Berlin Heidelberg, 1999).

[174] O. H. Seeck, LSFIT – Software zur Reflektivitätsbestimmung von Schichtsystemen.

[175] Y. V. Kudryavtsev, V. N. Uvarov, V. A. Oksenenko, Y. P. Lee, J. B. Kim, Y. H. Hyun, K. W. Kim, J. Y. Rhee, and J. Dubowik, Phys. Rev. B **77**, 195104 (2008).

[176] J. Braun, Reports on Progress in Physics **59**, 1267 (1996).

[177] D. E. Heim, Phys. Rev. B **33**, 5254 (1986).

[178] Y. Xu and S. Thompson, *Spintronic Materials and Technology*, *Series in Material Science and Engineering* (Taylor & Francis, London, United Kingdom, 2006).

[179] A. Nishide, Y. Takeichi, T. Okuda, A. A. Taskin, T. Hirahara, K. Nakatsuji, F. Komori, A. Kakizaki, Y. Ando, and I. Matsuda, New Journal of Physics **12**, 065011 (2010).

[180] T. Hirahara, G. Bihlmayer, Y. Sakamoto, M. Yamada, H. Miyazaki, S. ichi Kimura, S. Blügel, and S. Hasegawa, Phys. Rev. Lett. **107**, 166801 (2011).

[181] A. X. Gray, C. Papp, S. Ueda, B. Balke, Y. Yamashita, L. Plucinski, J. Minár, J. Braun, E. R. Ylvisaker, C. M. Schneider, W. E. Pickett, H. Ebert, K. Kobayashi, and C. S. Fadley, Nat. Mater. **10**, 759 (2011).

List of own publications

(in chronological order)

Papers

- R. Frahm, R. Wagner, **A. Herdt**, D. Lützenkirchen-Hecht
  "XAS at the materials science X-ray beamline BL8 at the DELTA storage ring"
  Journal of Physics: Conference Series **190**, 012040 (2009).

- C. J. Sahle, C. Sternemann, H. Conrad, **A. Herdt**, O. M. Feroughi, M. Tolan, A. Hohl, R. Wagner, D. Lützenkirchen-Hecht, R. Frahm, A. Sakko, K. Hamalainen
  "Phase separation and nanocrystal formation in GeO"
  Applied Physic Letters **95**, 021910 (2009).

- L. Plucinski, G. Mussler, J. Krumrain, **A. Herdt**, S. Suga, D. Grützmacher, C. M. Schneider
  "Robust surface electronic properties of topological insulators: Bi_2Te_3 films grown by molecular beam epitaxy"
  Applied Physic Letters **98**, 222503 (2011).

- A. Köhnen, M. Brücher, A. Reckmann, H. Klesper, A. v. Bohlen, R. Wagner, **A. Herdt**, D. Lützenkirchen-Hecht, R. Hergenröder, K. Meerholz
  "Tracing a Moving Thin-Film Reaction Front with Nanometer Resolution"
  Macromolecules **45**(8), 3487 (2012).

- **A. Herdt**, L. Plucinski, G. Bihlmayer, G. Mussler, S. Döring, J. Krumrain, D. Grützmacher, S. Blügel, C. M. Schneider
  "On the nature of the spin polarization limit in the Bi_2Te_3 Dirac cone"
  submitted to Physical Review Letters, under review (2012).

Posters

- C. J. Sahle, C. Sternemann, H. Conrad, **A. Herdt**, O. M. Feroughi, M. Tolan, A. Hohl, R. Wagner, D. Lützenkirchen-Hecht, R. Frahm, A. Sakko, K. Hamalainen
  "Phase separation and nanocrystal formation in bulk amorphous GeO"
  Frühjahrstagung der DPG, 22.-27.03.2009, Dresden (Germany).
- R. Frahm, R. Wagner, **A. Herdt**, D. Lützenkirchen-Hecht
  "XAS at the materials science X-ray beamline BL8 at the DELTA storage ring"
  XAFS 14 Conference, 26.-31.07.2009, Camerino (Italy).
- **A. Herdt**, R. Wagner, D. Lützenkirchen-Hecht, R. Frahm
  "First soft X-ray XAFS data using the YB_{66}-monochromator at beamline BL8"
  Sixth DELTA User meeting, 25.11.2010, Dortmund (Germany)
- L. Plucinski, **A. Herdt**, G. Bihlmayer, S. Döring, S. Blügel, C. M. Schneider
  "Spin-polarized photoemission from Bi_2Te_3 and Sb_2Te_3 topoloical insulator thin films"
  Frontiers in Electronic Materials: Correlation Effects and Memristive Phenomena (Nature Materials Conference), 17.-20.06.2012, Aachen (Germany)

Talks

- "Commissioning of the YB_{66}-monochromator at DELTA beamline BL8"
  Fifth DELTA User-Meeting 2009, Dortmund
- "Experiments at the Research Centre Jülich beamline BL5"
  NRW Forschungsschule: Forschung mit Synchrotronstrahlung in den Nano- und Biowissenschaften, 2010, Dortmund
- "Spin- and angle-resolved PES on Bi_2Te_3/Si(111) thin films at beamline BL5"
  Seventh DELTA User-Meeting 2011, Dortmund
- "Electronic properties of Bi_2Te_3 and Sb_2Te_3 studied by spin- and angle-resolved photoemission"

Seminar talk at the Technical University of Dortmund, Beschleunigerphysik/Synchrotronstrahlung mit Anwendungen in der Festkörperphysik, 2012, Dortmund

- "Spin- and angle-resolved photoemission spectroscopy on Bi_2Te_3 thin films" Frühjahrstagung der DPG, 2012, Dresden

Other publications

- C. J. Sahle, C. Sternemann, H. Conrad, **A. Herdt**, O. M. Feroughi, M. Tolan, A. Hohl, R. Wagner, D. Lützenkirchen-Hecht, R. Frahm, A. Sakko, K. Hamalainen
  "Phase separation of bulk amorphous GeO"
  Fourth DELTA User-Meeting, 25 (2008).

- D. Gottlob, M. Gulik, **A. Herdt**, L. Plucinski, S. Cramm, F. Matthes, B. Küpper, C. M. Schneider
  "Report-U250 PBM Beamline 5; Angle- and spin-polarized photoemission system with the upgraded in-situ sample preparation system"
  Fifth DELTA User-Meeting, 10 (2009).

- **A. Herdt**, R. Wagner, D. Lützenkirchen-Hecht, R. Frahm
  "Commissioning of the YB_{66}-monochromator at DELTA beamline BL8"
  Fifth DELTA User-Meeting, 12 (2009).

- C. J. Sahle, C. Sternemann, H. Conrad, **A. Herdt**, O. M. Feroughi, M. Tolan, A. Hohl, R. Wagner, D. Lützenkirchen-Hecht, R. Frahm, A. Sakko, K. Hamalainen
  "Phase separation and nanocrystal formation in GeO_x"
  Fifth DELTA User-Meeting, 40 (2009).

- L. Plucinski, **A. Herdt**, G. Bihlmayer, S. Döring, S. Blügel, C. M. Schneider
  "Spin-polarized photoemission from Bi_2Te_3 and Sb_2Te_3 topological insulator thin films"
  Frontiers in Electronic Materials Correlation Effects, Spintronics, and Memristive Phenomena - Fundamentals and Applications, ISBN 978-3-527-41191-7, Wiley-VCH, Berlin, 110 (2012).

Danksagung

Bei der Entstehung dieser Arbeit standen mir in den letzten drei Jahren viele Menschen unterstützend zur Seite, denen ich an dieser Stelle herzlich danken möchte.

Mein besonderer Dank gebührt meinem Doktorvater Prof. Dr. Claus M. Schneider für die freundliche Aufnahme an seinem Institut (PGI-6) und die kontinuierliche fachliche und finanzielle Unterstützung meiner Arbeit. Des weiteren danke ich für sein Vertrauen und die Freiheiten in der Ausübung meiner Tätigkeiten bei DELTA.

Ich danke Herrn Prof. Dr. Metin Tolan für die Bereitschaft, das Co-Referat zu übernehmen. Ferner, bedanke ich mich bei ihm für die Unterstützungen auf dem Weg zur Promotion.

Bei Dr. Lukasz Plucinski bedanke ich mich ganz besonders für die zahlreichen Diskussionen, Ratschläge und Ideen. Ohne seine großartige Unterstützung und Erfahrung wäre vieles nicht möglich gewesen. Ich bedanke mich für die kritische Durchsicht meiner Arbeit während seiner Urlaubszeit und seine unendliche Geduld.

Ferner danke ich Herrn Dr. Gustav Bihlmayer für die Bereitstellung der DFT Kalkulationen und die sehr gute Zusammenarbeit. Er hat mich bei allen theoretischen Fragestellungen bestens unterstützt. Vielen Dank für das Korrekturlesen des Theorieteils.

Ich danke Dr. Gregor Mussler vom PGI-3 für die Herstellung der MBE Topo-Proben sowie seinen Anmerkungen zu unserer Veröffentlichung.

Bei Dr. Michael Paulus, Dr. Christian Sternemann und Dr. Florian Wieland bedanke ich mich herzlich für die Hilfe am D8-Labordiffraktometer sowie für die

Unterstützung bei der Interpretation der Messdaten.

Ein großer Dank gilt meinen geschätzten Kollegen des PGI-6. Dr. Martina Müller und Dr. Sven Döring danke ich für das Korrigieren der ersten Version dieser Arbeit. Bei Sven möchte ich mich ferner für seine große Hilfe während der zahlreichen Messzeiten und für die nette Bürogemeinschaft bedanken. Bei Sarah Fahrendorf bedanke ich mich für die STM Messungen. Dennis Rudolf danke ich herzlich für seine Unterstützung am Magnetometer. Ferner danke ich Dr. Ingo Krug, Dr. Stefan Cramm, Florian Nickel, Daniel Gottlob und Christoph Keutner (AG Westphal) für Ihre Hilfe während der BESSY Messzeit. Ferner unterstützten mich Bernd Küpper, Conrad Bickmann, Heinz Pfeiffer, Jürgen Lauer und Franz-Josef Köhne bei der Erstellung diverser mechanischer und elektrischer Bauteile. Dafür möchte ich mich bei ihnen bedanken. Ohne die einzigartigen Konzeptplanungen von Bernd wäre vieles nicht möglich gewesen. Bei Frau Margret Frey, Frau Jutta Gollnick und Frau Elena Mirea bedanke ich mich herzlich für ihre tatkräftige Unterstützung bei allen verwaltungstechnischen Fragestellungen.

Ich möchte mich ebenfalls bei Frau S. Kralemann, Herrn M. Schier, Herrn P. Kortmann, Herrn W. Brembt sowie den Teams der mechanischen Werkstatt und der Elektronik-Werkstatt in Dortmund für die schnelle Fertigung der nötigten Bauteile bedanken. Des weiteren danke ich Patryk Towalski und Gerrit Schünemann für ihre Hilfe bei diversen Computerproblemen.

Der allergrößte Dank gilt meiner Familie. Ich danke meiner Mutter und Heinz für ihre tägliche Unterstützung, Fürsorge und Geduld in jeder Hinsicht. Meiner Frau danke ich für ihre fortwährende moralische Unterstützung und den familiären Rückhalt. Abschließend bedanke ich mich bei meinen Kindern für ihre mitreißende Kraft und ihren Elan.

1. **Soft Matter**
   From Synthetic to Biological Materials
   Lecture manuscripts of the 39th IFF Spring School March 3 – 14, 2008
   Jülich, Germany
   edited by J.K.G. Dhont, G. Gompper, G. Nägele, D. Richter, R.G. Winkler (2008),
   c. 1000 pages
   ISBN: 978-3-89336-517-3

2. **Structural analysis of diblock copolymer nanotemplates using grazing incidence scattering**
   by D. Korolkov (2008), III, 167 pages
   ISBN: 978-3-89336-522-7

3. **Thermal Nonequilibrium**
   Thermal forces in fluid mixtures
   Lecture Notes of the 8th International Meeting on Thermodiffusion,
   9 – 13 June 2008, Bonn, Germany
   edited by S. Wiegand, W. Köhler (2008), 300 pages
   ISBN: 978-3-89336-523-4

4. **Synthesis of CMR manganites and ordering phenomena in complex transition metal oxides**
   by H. Li (2008), IV, 176 pages
   ISBN: 978-3-89336-527-2

5. **Neutron Scattering**
   Lectures of the JCNS Laboratory Course held at the Forschungszentrum Jülich and the research reactor FRM II of TU Munich
   edited by R. Zorn, Th. Brückel, D. Richter (2008), ca. 500 pages
   ISBN: 978-3-89336-532-6

6. **Ultrafast Magnetization Dynamics**
   by S. Woodford (2008), 130 pages
   ISBN: 978-3-89336-536-4

7. **Role of Surface Roughness inTribology: from Atomic to Macroscopic Scale**
   by C. Yang (2008), VII, 166 pages
   ISBN: 978-3-89336-537-1

8. **Strahl- und Spindynamik von Hadronenstrahlen in Mittelenergie-Ringbeschleunigern**
   von A. Lehrach (2008), II, 171 Seiten
   ISBN: 978-3-89336-548-7

9. **Phase Behaviour of Proteins and Colloid-Polymer Mixtures**
   by C. Gögelein (2008), II, 147 pages
   ISBN: 978-3-89336-555-5

10. **Spintronics – From GMR to Quantum Information**
    Lecture Notes of the 40th IFF Spring School March 9 – 20, 2009
    Jülich, Germany
    edited by St. Blügel, D. Bürgler, M. Morgenstern, C. M. Schneider,
    R. Waser (2009), c. 1000 pages
    ISBN: 978-3-89336-559-3

11. **ANKE / PAX Workshop on SPIN Physics**
    JINR, Dubna, Russia / June 22. – 26, 2009
    Org. Committee: A. Kacharava, V. Komarov, A. Kulikov, P. Lenisa, R. Rathmann,
    H. Ströher (2009), CD-ROM
    ISBN: 978-3-89336-586-9

12. **Entwicklung einer Nanotechnologie-Plattform für die Herstellung Crossbar-basierter Speicherarchitekturen**
    von M. Meier (2009), 135 Seiten
    ISBN: 978-3-89336-598-2

13. **Electronic Oxides –**
    Correlation Phenomena, Exotic Phases and Novel Functionalities
    Lecture Notes of the 41st IFF Spring School March 8 – 19, 2010
    Jülich, Germany
    edited by St. Blügel, T. Brückel, R. Waser, C.M. Schneider (2010), ca. 1000 pages
    ISBN: 978-3-89336-609-5

14. **4th Georgian-German School and Workshop in Basic Science**
    Tbilisi, Georgia / May 3 – 7, 2010
    Org. Committee: E. Abrosimova, R. Botchorishvili, A. Kacharava, M. Nioradze,
    A. Prangishvili, H. Ströher (2010); CD-ROM
    ISBN: 978-3-89336-629-3

15. **Neutron Scattering**
    Lectures of the JCNS Laboratory Course held at Forschungszentrum Jülich and the research reactor FRM II of TU Munich
    edited by Th. Brückel, G. Heger, D. Richter, G. Roth and R. Zorn (2010),
    ca 350 pages
    ISBN: 978-3-89336-635-4

16. **Ab *initio* investigations of magnetic properties of ultrathin transition-metal films on *4d* substrates**
    by A. Al-Zubi (2010), II, 143 pages
    ISBN: 978-3-89336-641-5

17. **Investigation of a metal-organic interface realization and understanding of a molecular switch**
    by O. Neucheva (2010), 134 pages
    ISBN: 978-3-89336-650-7

18. **Reine Spinströme in lateralen Spinventilen, *in situ* Erzeugung und Nachweis**
von J. Mennig (2010), V, 95 Seiten
ISBN: 978-3-89336-684-2

19. **Nanoimprint Lithographie als Methode zur chemischen Oberflächenstrukturierung für Anwendungen in der Bioelektronik**
von S. Gilles (2010), II, 169 Seiten
ISBN: 978-3-89336-686-6

20. **Macromolecular Systems in Soft- and Living-Matter**
Lecture Notes of the 42nd IFF Spring School 2011 February 14 – 25, 2011 Jülich, Germany
edited by J. K.G. Dhont, G. Gompper, P. R.Lang, D. Richter, M. Ripoll, D. Willbold, R. Zorn (2011), ca. 1000 pages
ISBN: 978-3-89336-688-0

21. **The spin structure of magnetic nanoparticles and in magnetic nanostructures**
by S. Disch (2011), V, 342 pages
ISBN: 978-3-89336-704-7

22. **Element-selective and time-resolved magnetic investigations in the extreme ultraviolet range**
by P. Grychtol (2011), xii, 144 pages
ISBN: 978-3-89336-706-1

23. **Spin-Transfer Torque Induced Dynamics of Magnetic Vortices in Nanopillars**
by V. Sluka (2011), 121 pages
ISBN: 978-3-89336-717-7

24. **Adsorption von Phthalocyaninen auf Edelmetalloberflächen**
von I. Kröger (2011), vi, 206 Seiten
ISBN: 978-3-89336-720-7

25. **Time-Resolved Single Molecule FRET Studies on Folding/Unfolding Transitions and on Functional Conformational Changes of Phosphoglycerate Kinase**
by T. Rosenkranz (2011), III, 139 pages
ISBN: 978-3-89336-721-4

26. **NMR solution structures of the MIoK1 cyclic nucleotide-gated ion channel binding domain**
by S. Schünke (2011), VI, (getr. pag.)
ISBN: 978-3-89336-722-1

27. **Neutron Scattering**
    Lectures of the JCNS Laboratory Course held at Forschungszentrum Jülich and the research reactor FRM II of TU Munich
    edited by Th. Brückel, G. Heger, D. Richter, G. Roth and R. Zorn (2011), ca 350 pages
    ISBN: 978-3-89336-725-2

28. **Neutron Scattering**
    Experiment Manuals of the JCNS Laborator Course held at Forschungszentrum Jülich and the research reactorFRM II of TU Munich
    edited by Th. Brückel, G. Heger, D. Richter, G. Roth and R. Zorn (2011), ca. 180 pages
    ISBN: 978-3-89336-726-9

29. **Silicon nanowire transistor arrays for biomolecular detection**
    by X.T.Vu (2011), vii, 174 pages
    ISBN: 978-3-89336-739-9

30. **Interactions between parallel carbon nanotube quantum dots**
    by K. Goß (2011), viii, 139 pages
    ISBN: 978-3-89336-740-5

31. **Effect of spin-orbit scattering on transport properties of low-dimensional dilute alloys**
    by S. Heers (2011), viii, 216 pages
    ISBN: 978-3-89336-747-4

32. **Charged colloids and proteins: Structure, diffusion, and rheology**
    by M. Heinen (2011), xii, 186 pages
    ISBN: 978-3-89336-751-1

33. **Scattering Methods for Condensed Matter Research: Towards Novel Applications at Future Sources**
    Lecture Notes of the 43rd IFF Spring School 2012
    March 5 – 16, 2012 Jülich, Germany
    edited by M. Angst, T. Brückel, D. Richter, R. Zorn ca. 1000 pages
    ISBN: 978-3-89336-759-7

34. **Single-Site Green Function of the Dirac Equation for Full-Potential Electron Scattering**
    by P. Kordt (2012), 138 pages
    ISBN: 978-3-89336-760-3

35. **Time Resolved Single Molecule Fluorescence Spectroscopy on Surface Tethered and Freely Diffusing Proteins**
    by D. Atta (2012), iv, 126 pages
    ISBN: 978-3-89336-763-4

36. **Fabrication and Utilization of Mechanically Controllable Break Junction for Bioelectronics**
by D. Xiang (2012), 129 pages
ISBN: 978-3-89336-769-6

37. **Contact Mechanics and Friction of Elastic Solids on Hard and Rough Substrates**
by B. Lorenz (2012), iv, 121 pages
ISBN: 978-3-89336-779-5

38. **Ab initio Calculations of Spin-Wave Excitation Spectra from Time-Dependent Density-Functional Theory**
by M. Niesert (2012), 146 pages
ISBN: 978-3-89336-786-3

39. **Neutron Scattering**
Lectures of the JCNS Laboratory Course held at Forschungszentrum Jülich and the research reactor FRM II of TU Munich
edited by Th. Brückel, G. Heger, D. Richter, G. Roth and R. Zorn (2012),
ca 350 pages
ISBN: 978-3-89336-789-4

40. **Neutron Scattering**
Experiment Manuals of the JCNS Laborator Course held at Forschungszentrum Jülich and the research reactorFRM II of TU Munich
edited by Th. Brückel, G. Heger, D. Richter, G. Roth and R. Zorn (2012),
ca. 175 pages
ISBN: 978-3-89336-790-0

41. **Influence of a shear flow on colloidal depletion interaction**
by C. July (2012), xviii, 105 pages
ISBN: 978-3-89336-791-7

42. **NMR studies on the isolated C39 peptidase-like domain of ABC transporter Haemolysin B from *E. coli*: Investigation of the solution structure and the binding interface with HlyA**
by J. Lecher (2012), 126 pages
ISBN: 978-3-89336-793-1

43. **Spin Correlations and Excitations in Spin-frustrated Molecular and Molecule-based Magnets**
by Z. Fu (2012), 208 pages
ISBN: 978-3-89336-797-9

44. **Crystal and spin structure and their relation to physical properties in some geometrical and spin spiral multiferroics**
by N. K. Chogondahalli Muniraju (2012), iii, 190 pages
ISBN: 978-3-89336-802-0

45. **Multiferroicity in oxide thin films and heterostructures**
by A. Glavic (2012), xi, 152 pages
ISBN: 978-3-89336-803-7

46. **German Neutron Scattering Conference 2012**
September 24 -26, 2012. Gustav-Stresemann-Institut, Bonn, Germany
edited by Th. Brückel (2012)
ISBN: 978-3-89336-807-5

47. **STM beyond vacuum tunnelling: Scanning Tunnelling Hydrogen Microscopy as a route to ultra-high resolution**
by C. Weiss (2012), II, 165 pages
ISBN: 978-3-89336-813-6

48. **High Temperature Radio-Frequency Superconducting Quantum Interference Device System for Detection of Magnetic Nanoparticles**
by A. Pretzell (2012), 122 pages
ISBN: 978-3-89336-814-3

49. **Study of Molecule-Metal Interfaces by Means of the Normal Incidence X-ray Standing Wave Technique**
by G. Mercurio (2012), XXII, 361 pages
ISBN: 978-3-89336-816-7

50. **5th Georgian-German School and Workshop in Basic Science**
Tbilisi, Georgia/August 6 – 10, 2012. Batumi, Georgia/August 13 – 17, 2012.
Org. Committee: E. Abrosimova, A. Bakuridze, A. Kacharava, A. Kvitashvili, A. Prangishvili, H. Ströher (2012); CD-ROM
ISBN: 978-3-89336-818-1

51. **Exploring the electronic properties of novel spintronic materials by photoelectron spectroscopy**
by A. Herdt (2012), ii, 126 pages
ISBN: 978-3-89336-831-0

Schlüsseltechnologien / Key Technologies
Band / Volume 51
ISBN 978-3-89336-831-0

JÜLICH
FORSCHUNGSZENTRUM